

AD \_\_\_\_\_

Award Number: DAMD17-98-1-8176

TITLE: Computer Simulation of Breast Cancer Screening

PRINCIPAL INVESTIGATOR: John Boone, Ph.D.

CONTRACTING ORGANIZATION: University of California  
Davis, California 95616

REPORT DATE: July 2000

TYPE OF REPORT: Annual

PREPARED FOR: U.S. Army Medical Research and Materiel Command  
Fort Detrick, Maryland 21702-5012

DISTRIBUTION STATEMENT: Approved for Public Release;  
Distribution Unlimited

The views, opinions and/or findings contained in this report are those of the author(s) and should not be construed as an official Department of the Army position, policy or decision unless so designated by other documentation.

20010509 080

REPORT DOCUMENTATION PAGE			Form Approved OMB No. 074-0188	
Public reporting burden for this collection of information is estimated to average 1 hour per response, including the time for reviewing instructions, searching existing data sources, gathering and maintaining the data needed, and completing and reviewing this collection of information. Send comments regarding this burden estimate or any other aspect of this collection of information, including suggestions for reducing this burden to Washington Headquarters Services, Directorate for Information Operations and Reports, 1215 Jefferson Davis Highway, Suite 1204, Arlington, VA 22202-4302, and to the Office of Management and Budget, Paperwork Reduction Project (0704-0188), Washington, DC 20503				
1. AGENCY USE ONLY (Leave blank)	2. REPORT DATE July 2000	3. REPORT TYPE AND DATES COVERED Annual (1 Jul 99 - 30 Jun 00)		
4. TITLE AND SUBTITLE Computer Simulation of Breast Cancer Screening		5. FUNDING NUMBERS DAMD17-98-1-8176		
6. AUTHOR(S) John M. Boone, Ph.D.				
7. PERFORMING ORGANIZATION NAME(S) AND ADDRESS(ES) University of California Davis, California 95616  E-MAIL: jmboone@ucdavis.edu		8. PERFORMING ORGANIZATION REPORT NUMBER		
9. SPONSORING / MONITORING AGENCY NAME(S) AND ADDRESS(ES)  U.S. Army Medical Research and Materiel Command Fort Detrick, Maryland 21702-5012		10. SPONSORING / MONITORING AGENCY REPORT NUMBER		
11. SUPPLEMENTARY NOTES				
12a. DISTRIBUTION / AVAILABILITY STATEMENT Approved for public release; distribution unlimited			12b. DISTRIBUTION CODE	
13. ABSTRACT (Maximum 200 Words)  Breast cancer screening has been shown to reduce breast cancer mortality, however the current protocols for screening (annual screens after age 40) are not optimized and do not appropriately accommodate the spectrum of breast cancer risk present in the screening population. Optimization studies using clinical trials are unrealistic because of cost, time, and ethical concerns. In this investigation, we are developing a computer model which allows a wide variety of breast cancer screening protocols to be studied in the computer simulation environment. The computer model incorporates a variety of data into various modules, including demographic, incidence, growth rate, detection, survival, and other sources of data from the literature. Once the computer model is validated against published clinical trial data, it can be used to predict the most efficient screening schedules for women in various categories of risk. The model currently focuses on mammography for breast cancer screening, but other screening procedures including alternative imaging methods (e.g. MRI, ultrasound, computed tomography) or serum-based tumor marker testing could be incorporated into the model. Progress towards building all modules has proceeded well and after additional validation analyses, the methods used will be ready for reporting in the scientific literature.				
14. SUBJECT TERMS Breast Cancer			15. NUMBER OF PAGES 106	
			16. PRICE CODE	
17. SECURITY CLASSIFICATION OF REPORT Unclassified	18. SECURITY CLASSIFICATION OF THIS PAGE Unclassified	19. SECURITY CLASSIFICATION OF ABSTRACT Unclassified	20. LIMITATION OF ABSTRACT Unlimited	

NSN 7540-01-280-5500

Standard Form 298 (Rev. 2-89)  
Prescribed by ANSI Std. Z39-18  
298-102

## FOREWORD

Opinions, interpretations, conclusions and recommendations are those of the author and are not necessarily endorsed by the U.S. Army.

\_\_\_ Where copyrighted material is quoted, permission has been obtained to use such material.

\_\_\_ Where material from documents designated for limited distribution is quoted, permission has been obtained to use the material.

\_\_\_ Citations of commercial organizations and trade names in this report do not constitute an official Department of Army endorsement or approval of the products or services of these organizations.

N/A In conducting research using animals, the investigator(s) adhered to the "Guide for the Care and Use of Laboratory Animals," prepared by the Committee on Care and use of Laboratory Animals of the Institute of Laboratory Resources, national Research Council (NIH Publication No. 86-23, Revised 1985).

N/A For the protection of human subjects, the investigator(s) adhered to policies of applicable Federal Law 45 CFR 46.

N/A In conducting research utilizing recombinant DNA technology, the investigator(s) adhered to current guidelines promulgated by the National Institutes of Health.

N/A In the conduct of research utilizing recombinant DNA, the investigator(s) adhered to the NIH Guidelines for Research Involving Recombinant DNA Molecules.

N/A In the conduct of research involving hazardous organisms, the investigator(s) adhered to the CDC-NIH Guide for Biosafety in Microbiological and Biomedical Laboratories.

  
PI - Signature 7/24/00  
Date

## **Table of Contents**

<b>Cover.....</b>	<b>1</b>
<b>SF 298.....</b>	<b>2</b>
<b>Foreword.....</b>	<b>3</b>
<b>Table of Contents.....</b>	<b>4</b>
<b>Introduction.....</b>	<b>5</b>
<b>Body.....</b>	<b>6</b>
<b>Key Research Accomplishments.....</b>	<b>13</b>
<b>Reportable Outcomes.....</b>	<b>14</b>
<b>Conclusions.....</b>	<b>16</b>
<b>References.....</b>	<b>17</b>
<b>Appendices.....</b>	<b>18</b>

## INTRODUCTION

Breast cancer screening remains a key aspect of the fight to reduce the mortality of this disease. Over the years since mammography has been used for breast cancer screening, there has been substantial improvements in the technology. Simultaneously, the efficacy of breast cancer screening was evaluated in various clinical studies. While there is a growing consensus that breast cancer screening using mammography does in fact save lives, the exact protocol for optimal breast cancer screening has not enjoyed a consensus of opinion. For example, in the United States, after a fractious consensus conference, a panel of experts was over-ruled by leaders at the NIH, resulting in the current NCI recommendation that annual screening after age 40 be pursued. In Europe, different mammographic views (e.g. a different angle) and numbers of images (one mammogram instead of two) are used and the screening intervals and ages of women screened differ between countries. While a long term multi-institutional study using a large cohort of women could be used to optimize screening protocols, the time involved, enormous costs, and ethical issues associated with such a study prevent such an endeavor. This research is aimed at developing the methods for computer simulating such a study.

Population demographics, breast cancer incidence data, growth rate data, screening detectability data, breast cancer survival data, and other scientific data sources available from the research literature are combined with Monte Carlo techniques to produce a computer simulator for breast cancer screening. In the computer simulation environment, millions of women can be screened throughout their lives in a matter of minutes. The same cohort of simulated women can be screened repeatedly using different screening protocols, with the hopes of finding the most efficacious screening protocol for saving lives. In addition to optimizing the screening protocols depending on a women's individual risks (including her race, family history, breast density, and genetic profile), the development of this simulation tool will also allow scientists to predict appropriate screening intervals and starting ages for screening modalities other than screen-film mammography. The use of digital mammography, magnetic resonance, ultrasound, and blood tests are all currently under investigation for breast cancer screening. Once the detection abilities of these techniques are understood and characterized, they may individually or jointly be studied using the computer simulator to better understand and hopefully predict the best usage schedules of screening technology for the ultimate elimination of breast cancer mortality.

## BODY

Our work in the first year of this research touched on all of the statement of work (SOW) issues, and significant progress was made towards each of the specific aims (SOWs) of this proposal. The progress report submitted last year (August 20, 1999) for this grant contained 50 figures, detailing our vigorous efforts towards completion of the various aims of the research. We seek to not repeat that description, and hopefully the reviewers of this report will have the Year 1 Annual Report at their disposal to assess total progress to date. Here we concentrate on our specific efforts of this past year, year 2 of the project.

---

### **Statement of Work 1: Determine detectability of mammography versus breast density**

---

### **Statement of Work 2: Determine detectability versus lesion size and x-ray dose**

---

SOWs 1 and 2 are related and will be discussed together. Significant work was performed in Year 1 of the research, resulting in Figures 7 through 29 in the Year 1 Annual Report. Those discussions will not be repeated here. Not discussed in the Year 1 annual report were related studies that seek to better quantify various aspects of the mammography procedure. By better understanding mammography (and digital mammography), the physics of the procedure can be better simulated and the detectability of breast cancer as a function of various parameters (notably breast density, lesion size, breast thickness as it affects x-ray scatter, and x-ray dose) can be more accurately assessed.

### **X-ray Fluorescence**

An evaluation of x-ray fluorescence in x-ray detectors (including those used in mammography) was performed using Monte Carlo procedures, and this comprehensive investigation led to the publication included as Appendix 1:

JM Boone, JA Seibert, JM Sabol, and M Tecotzky, "A Monte Carlo study of x-ray fluorescence in x-ray detectors", Medical Physics 26, 905-916 (1999)

The study evaluated seven different detector types for x-ray imaging, and quantified the energy-dependence of x-ray fluorescence that is reabsorbed in the phosphor. This is important in the context of breast cancer detectability, because x-ray fluorescence acts as a source of glare in the detector system, and this reduces contrast resolution. While the study identified x-ray fluorescence (otherwise known as characteristic x-ray radiation) as a potential source of contrast resolution reduction in x-ray imaging, the effects are probably too subtle to have a significant impact in the mammography setting.

## Lesion Detectability in Quantum Noise Background

To address the fundamental limitations in lesion detectability under the simplest of circumstances (no breast parenchymal structure), a computer simulation study was performed which focussed on the parameters of radiation exposure level (x-ray photon fluence), detector element size, and lesion size. This data is presented in Appendix 2 and was published recently as:

VN Cooper, JM Boone, and JA Seibert, "A lesion detectability simulation method for digital x-ray imaging", Medical Physics 27;66-74 (2000)

The above study was generic in the sense that it covered a range of x-ray exposures from fluoroscopic levels (1  $\mu\text{R}/\text{image}$ ) to x-ray mammography levels (10 mR/image), and also addressed the detectability of both soft tissue and calcium-based "lesions". The study was performed using the simplifying assumptions of monoenergetic 50 keV x-ray photons and assuming ideal detection performance of the imaging system. While the findings of this paper confirm what theory predicts, the Monte Carlo nature of the report gives upper limitations on the detectability of lesions under various conditions. For example, for a 1 mm soft tissue lesion and 100  $\mu\text{m}$  square detector elements, the exposure to the detector should be greater than about 1 mR to assure near perfect detection. For a 2 mm soft tissue lesion and 100  $\mu\text{m}$  detector elements, as long as the detector exposure exceeds 100  $\mu\text{R}$ , the lesion will be detected in the vast majority of cases based on the area under the receiver operating characteristic (ROC) curve approaching unity (i.e.,  $A_z \rightarrow 1.0$ ). For larger lesions than 2 mm, better detectability results. Those results are applicable to 50 keV x-rays, but in mammography the average energy of an x-ray beam is closer to 20 keV. At 50 keV there are about 270,000 photons per  $\text{mm}^2$  per mR, whereas at 20 keV there are about 55,000 photons per  $\text{mm}^2$  per mR. Thus, to correct for this difference in the conversion factor between x-ray exposure and photon fluence, the exposure levels need to be increased by a factor of 4.9 (270,000 / 55,000). Nevertheless, this means that at mammographic energies that 4.9 mR is needed to routinely detect 1 mm soft tissue lesions and 490  $\mu\text{R}$  is needed to detect 2 mm lesions.

What the above simple simulation demonstrated that for standard mammography or digital mammography, where the lesions to be detected are generally *much* larger than 2 mm (the median lesion detection in clinical mammography is about 11 mm in diameter), the quantum noise associated with the x-ray fluence is not an important factor in obscuring lesion detection. This is the case since the typical exposure to the detector in mammography and digital mammography is on the order of 10 mR, higher than the 490  $\mu\text{R}$  and 4.9 mR limits observed in the above paragraph for the ideal detection of 2 mm and 1 mm lesions, respectively. These x-ray quantum statistic based simulations indicate that for lesions greater than about 1 mm, that x-ray quantum statistics do not play an important role in the reduction of lesion detection (on the other hand, the structured noise associated with tissue parenchyma is a major factor which obscures lesions). This result is the answer sought in SOW 2.

## **X-ray Scatter**

X-ray scatter affects lesion detectability by reducing the contrast in screen film mammography, or by increasing the noise in digital mammography. We developed a novel method for physically measuring the scatter to primary ratio (SPR) in mammography, and these results are included as Appendix 3, corresponding to the publication:

VN Cooper, JM Boone, and JA Seibert, C Pellot-Barakat, "An edge spread technique for measurement of the scatter to primary ratio in mammography", Medical Physics 27: 845-853 (2000)

In this report, the SPR was evaluated as a function of breast thickness, breast composition (i.e. glandular fraction) and x-ray beam energy. In a concise oversimplification, at the center of the field of view the SPRs are approximately 0.2, 0.4, 0.6, and 0.8 for 2 cm, 4 cm, 6 cm, and 8 cm breast thicknesses, respectively. The influence of x-ray energy (kVp) and breast composition on the SPR are minor. These measured SPRs are indicative of the scattered radiation intensity in the absence of an anti-scatter grid. Continuing Monte Carlo work in our laboratory, in addition to the published work of Rezentes and Barnes<sup>1</sup> will be used to convert these (Appendix 3) SPR values to SPRs in the presence of a grid.

While we have not incorporated the effect of x-ray scatter in the computer modeling of lesion detectability, however this will be performed in the forthcoming year if time allows and if the post-grid SPRs remain non-negligible.

## **X-ray Dose**

In the discussion of optimizing the efficacy of breast cancer screening, what actually prevents screening for breast cancer on a daily basis? Each women can come home from work and have a daily mammogram before dinner. Surely the earliest detection would be achieved under daily screening, since the *sojourn time* (the time between when the lesion is *detectable* and when it is actually *detected*) would be measured in hours. Well the obvious factor that prevents daily screening is the cost, but we would like to ground the science in physical terms, not in economic ones alone. That being the case, daily screening would result in a 365 fold increase in the radiation dose to the breast, compared with annual screening (the current standard). Such high radiation levels would surely impact breast cancer incidence by increasing the number of radiation-induced breast cancers. Therefore, a complete understanding of the radiation dose received in screening mammography is necessary. The influence of radiation dose was not specifically mentioned as an item in the statement of work for this proposal, however it has long been considered by us as an important component to include in the breast cancer screening simulator. The accumulated x-ray dose to the breast tissue for a given women and screening protocol would have to be translated to excess risk, which in turn is communicated to the computer model which calculates breast cancers from incidence data. X-ray dose is the sole physical parameter that drives the screening interval towards longer periods, rather than shorter ones.



While radiation dose values using so-called DgN (roentgen to rad conversion factors, or using SI nomenclature, air dose to glandular dose conversion factors) were available in the literature for conventional x-ray spectra<sup>2,3</sup>, the recent FDA approval of digital mammography for clinical screening presents a need to be able to calculate breast dose for non-standard x-ray spectra, since digital mammography systems will generally make use of slightly harder (higher energy) x-ray beams for mammography. Thus, a comprehensive study of the x-ray dose conversion factors was performed, and is presented in Appendix 4. This article was the lead scientific article in the October 1999 issue of Radiology, the first time in recent memory when a physics paper has held such a position:

JM Boone, "Glandular breast dose for monoenergetic and high-energy x-ray beams: Monte Carlo assessment", Radiology 213, 23-37 (1999)

### Converting $A_z$ to the Probability of Breast Cancer Detection

The studies described in Appendix 2 and in Figures 27 and 28 of the Year 1 Annual report lead to the computation of the  $A_z$  value – the area under the ROC curve. An ROC curve is a plot of the sensitivity as a function of [1-specificity]:

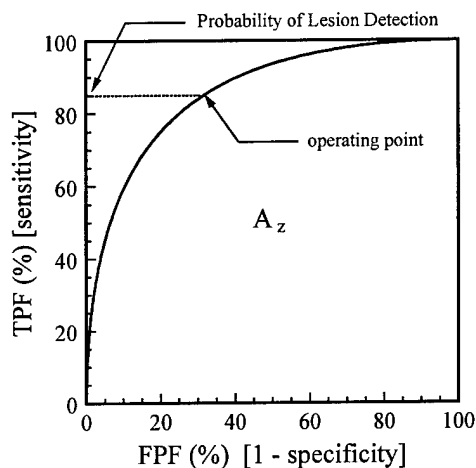


**Figure 1:** An receiver operating characteristic (ROC) curve is shown. The area under the curve is given by  $A_z$ . The result of our computer simulations which utilized ROC analysis was the  $A_z$  value, which ranges from 0.5 (worse case, pure guessing) to 1.0 (best case, perfect detection). However, the  $A_z$  is not equal to the actual probability of lesion detection. Rather, the operating point on the ROC curve needs to be known, and from this the sensitivity can be computed. The sensitivity is numerically equal to the probability of lesion detection when a lesion is present in the breast.

To convert the  $A_z$  value to the probability of detection, the operating point on the ROC curve for a given diagnostician needs to be known. From this, the sensitivity, which is the probability of lesion detection, can be computed (see Figure 1). We realized, as described in detail in the manuscript given as Appendix 5, that the operating point in mammography can be calculated if the cancer detection rate (typical metric of the CDR is *cancers detected per 1000 screens*) and the positive predictive value (PPV, otherwise known as the positive biopsy rate) are known. Because of the imposition of strict standards in mammography due to MQSA and other forces, the CDR and the PPV are known for most institutions – the CDR is typically about 3 cancers per 1000 screens for a mixed age screening population (this increases in older cohorts), and the PPV ranges around 20-30% in most US screening facilities (1 cancer for every 4 or 5 breast biopsies). The mathematics and theoretical development for these observations are developed in the manuscript in Appendix 5.

This manuscript was submitted to *Radiology* and rejected, primarily, we were criticized for assuming a symmetrical ROC curve. We have already generalized the mathematics to include asymmetrical ROC curves (i.e. this occurs when the noise variances in the normal and abnormal populations are unequal), and will soon revise and resubmit the manuscript to a different journal.

The interesting take-home message of the data presented in Appendix 5 is that for typical operating conditions in breast cancer screening clinics in the United States (e.g. CDR  $\approx$  4), even high  $A_z$  values such as 0.95 result in relatively low probability of breast cancer detection. This is illustrated in Figure 2:

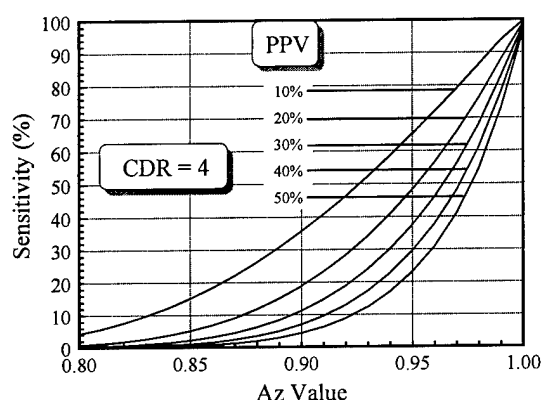


**Figure 2:** The sensitivity is the probability of detecting breast cancer when it is present. For positive predictive values (i.e. essentially equal to the positive biopsy rate) between 20% and 30% (typical values), the probability of detection at an  $A_z$  of 0.95 ranges from 37% to 47%. Even with  $A_z$  values of 0.99, the probability of cancer detection is only 82% to 87%. These values are for a cancer detection rate of 4 cancers per 1000 screens, which is typical if not a bit high for the United States.

The other hidden message of Figure 2 is given by the trend seen in the family of curves for the different PPVs. As the positive biopsy rate decreases (meaning the number of benign biopsies increases), the probability of cancer detection increases. The low positive biopsy rate typical in breast cancer diagnosis is often criticized in scientific and advocate circles as a failure of mammographic screening, but Figure 2 illustrates that low positive biopsy rates (a consequence of overcalling breast cancer) are actually *necessary* for improving sensitivity, given fixed levels of  $A_z$ .

The above analysis (and that given in Appendix 5) is used to convert our  $A_z$  values determined from Monte Carlo produced ROC curves (performed by placing simulated breast cancer lesions on top of digitized mammograms) to actual probabilities of detection – the detection probability is needed in the screening simulator. Notice that any new screening modality can be studied using the breast cancer screening simulator being developed in this project, if the probability of detection as a function of breast cancer diameter is known. Thus, blood tests, MRI, ultrasound, and any other possible detection methodologies can be studied for their overall impact on breast cancer mortality.

---

### Statement of Work 3: Develop a breast cancer growth model

---

This work has been done and was presented in the Year 1 annual report, Figures 36, 37 and 38. Further minor development may be pursued in Year 3.

---

**Statement of Work 4: Evaluate breast cancer prognosis from survival data**

---

This work was done and presented in the Year 1 annual report, Figures 39, 40, and 41. Survival data (prognosis) changes as the treatment of breast cancer changes (i.e lumpectomy with radiation or not), however for any new treatment regime the clinical outcomes are not fully known until several decades later. We continue to monitor the current literature to keep up with newly reported survival data. All new results will be evaluated and incorporated into the prognosis simulator module of the breast cancer screening simulator.

---

**Statement of Work 5: Develop a model for generating accurate US demographics**

---

This was performed in year 1 and presented in the Year 1 annual report, as Figures 1, 2, 3, 4, 5, and 6. As soon as the demographic data from the 2000 census is available, that data will be substituted for the currently used census bureau projections for 1997 (which were based largely on the 1990 census).

---

**Statement of Work 6: combine components above into a computer simulation model**

---

The computer models from the various sub-components of the research (SOWs 1-5, etc.) have been assembled into a comprehensive screening simulator tool. The simulator has been separated into two parts, *a cohort generator*, which is capable of generating large cohorts of simulated women with various characteristics. For example, the cohort simulator can be used to simulate different racial mixtures to emulate the population of different cities in the US. Cohorts of women with specific breast densities can be created (breast density is a large risk factor for breast cancer). Different age ranges of women can be studied as well. In short, the cohort generator gives us the flexibility to vary parameters in a given cohort of women, while allowing the other parameters to remain comparable statistically to that of the general US population. The cohort generator thus creates sub-populations of women with unique characteristics, and this cohort is saved to computer disk. An example of one of these files for a few simulated women is given below:

#	R	B	Age <sub>1</sub>	Age <sub>2</sub>	BC	BDI <sub>2</sub>
1802	2	1	69.935	80.935	-1.000	-0.740
1803	1	4	73.979	96.313	-1.000	3.512
1804	1	4	5.914	83.164	76.331	-0.298
1805	2	2	22.531	52.114	-1.000	-1.388

where # = women number, R = race code (1-4), B = breast density pentile, Age<sub>1</sub> = age on July 1, 2000, Age<sub>2</sub> = Age at death from non-BC causes, BC = age at BC initialization (-1 = no breast cancer during life), and BDI<sub>2</sub> = a second parameter used for determining the women's breast density.

Once generated and saved to computer disk, each cohort can then be used in the second component of the breast cancer screening simulator, *the screening simulator*, where each women undergoes a

breast cancer screening regime which can be changed using parameters unique to the screening simulator. By studying the exact same cohort of women repeatedly with different screening parameters, optimization and efficacy metrics can be determined. The screening interval, and the ages at which screening begins and at which screening ends are the obvious three parameters which can be varied in the screening simulator component of the model. Other less obvious screening simulations can be performed by modifying the screening simulator to change the screening interval as each women ages (shorter intervals for younger women), or to increase the screening interval for women with dense breasts (higher risks).

In the forthcoming year, we plan to make the selection of input parameters for both the cohort generator and the screening simulator a little more user friendly.

---

**Statement of Work 7: Validate the screening model against the Swedish trial data**

---

Preliminary validation of the breast cancer screening model has been done, as shown in Figures 42 and 43 of the Year 1 Annual report. A more comprehensive evaluation and validation of the model will be performed in Year 3 (this coming year) of this research.

---

**Statement of Work 8: determine optimal screening protocols**

---

Preliminary output of the breast cancer screening simulator, pertaining to optimizing screening intervals and ages, is illustrated in Figures 42 through 50 of the Year 1 Annual Report. We will generate screening output results data once the simulator has been completely validated, as described in SOW 7. This will be done in Year 3 of the grant.

## KEY RESEARCH ACCOMPLISHMENTS

- A comprehensive breast cancer screening simulation tool is well underway towards development and validation. Once completed, this simulation tool may prove useful in predicting optimal screening protocols for various risk categories of women.
- As an example of the output of the screening simulator *that has yet to be fully validated*, we submit the following Figure 3.

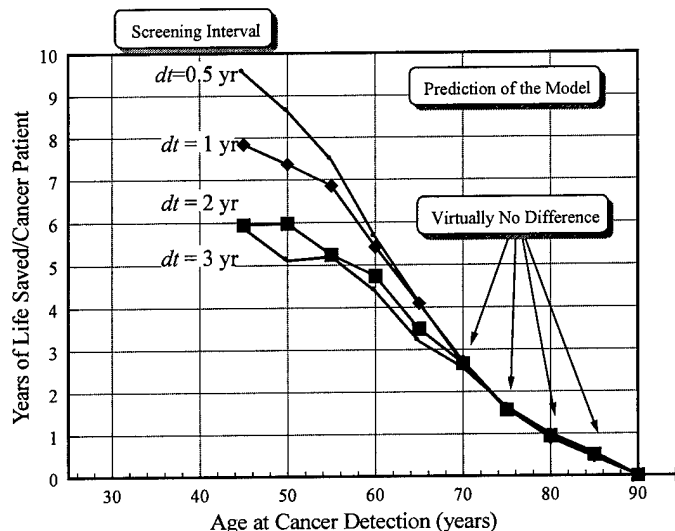


**Figure 3:** The purpose of breast cancer screening is to reduce breast cancer mortality, which really means saving years of cancer patient's lives. That metric, which can be assessed in the simulator, is plotted as a function of age at cancer detection for four different screening intervals,  $\frac{1}{2}$  year, 1 year, 2 years, and 3 years. The results in the graph indicate that there is no difference in outcome between the four different screening protocols for women aged 70 and above: This is because their cancers are more slowly growing than in younger women. However, for women aged 45 years, extending screening from 1 year to 6 month intervals saves more than one year of life per cancer patient.

The above example (which has yet to be fully validated) has the potential for profound implications on breast cancer screening policy in the United States. We do not suggest or suppose that screening policy would be changed by the results of a mere computer simulation, rather these results are intended to provide deeper insight into the relationship between breast cancer mortality and the many parameters that affect screening efficacy.

# REPORTABLE OUTCOMES

---

## *Outcomes from Year 1 Annual Report:*

---

### **Abstract**

- JM Boone and KK Lindfors, "Computer simulation of breast cancer screening efficacy", Medical Physics 26: 1065-1066 (1999)

### **Invited Presentation**

- JM Boone and KK Lindfors, "Computer simulation of breast cancer screening efficacy", presented at the 1999 annual meeting of the American Association of Physicists in Medicine, Nashville, TN (July 26, 1999).

---

## *Outcomes new to this annual report:*

---

### **Published Papers citing this grant:**

- JM Boone, JA Seibert, JM Sabol, and M Tecotzky, "A Monte Carlo study of x-ray fluorescence in x-ray detectors", Medical Physics 26, 905-916 (1999)
- JM Boone, "Glandular breast dose for monoenergetic and high-energy x-ray beams: Monte Carlo assessment", Radiology 213, 23-37 (1999)
- VN Cooper, JM Boone, and JA Seibert, "A lesion detectability simulation method for digital x-ray imaging", Medical Physics 27;66-74 (2000)
- VN Cooper, JM Boone, and JA Seibert, C Pellot-Barakat, "An edge spread technique for measurement of the scatter to primary ratio in mammography", Medical Physics 27: 845-853 (2000)

### **Manuscript in preparation citing this grant:**

- JM Boone, KK Lindfors, JA Seibert, and MN Haan, "Relating ROC curve area ( $A_z$ ) to sensitivity and specificity with application to mammography"

### **Grants Applied For**

The results presented above and in the Year 1 Annual Report have formed the basis for an NIH grant proposal submission. The proposal is entitled, "A fundamental study of breast cancer screening performance", and has been given the NIH designation of R01 CA86891-01. John Boone is the PI of this proposal. This is a five year, \$750,000 R01 grant. Unfortunately, the November 1999 submission of the grant was reviewed and it received an "unscored". We have rebutted the many incorrect comments of the reviewers and revised the grant to include many of the reviewers more appropriate comments, have resubmitted this proposal in June 2000 (so it is now designated as

R01 CA86891-01A1). Significantly, we have added Dr. Art Burgess as a consultant to this project, and his expertise will be a valuable addition to the research endeavor should it be funded.

## CONCLUSIONS

We remain very excited about the continued development and potential of the proposed breast cancer screening simulator. Our excitement has led to the submission of an NIH grant, with the intention of getting continued support to carry this work on. The PI had the privilege to recently serve on an *ad hoc* NIH study section (RFA CA-99-013, "Cancer Intervention and Surveillance Modeling Network" - CISNET, [<http://grants.nih.gov/grants/guide/rfa-files/RFA-CA-99-013.html>]) that reviewed approximately 50 proposals having to do with computer simulation of cancer screening, for colon, breast, and prostate cancers. With the perspectives gained from reviewing so many proposals in a subject area close to this research, we now realize that this research is much further along than most of the field. This has led us to revamp our previous go-slow approach towards publishing. We now plan to write a manuscript describing the simulation tool *en toto* after some further verification, and submit this to an appropriate journal.

We will wait to make specific scientific conclusions once further verification of the simulation tool has been further developed and verified. Rather, we conclude with some thoughts about the future of breast cancer screening simulations. We foresee an interesting ethical dilemma looming on the horizon that may affect this type of research. Computer simulations are used in many facets of the modern world which affect either large numbers of people or large amounts of federal funding or both, from weather forecasting and airplane design (e.g. the Boeing 777) to models of the early universe and of magma flow in the earth's core (earthquake forecasting). Nevertheless, computer simulations in health care and specifically in cancer screening will remain controversial, we suspect, because of the personal nature of cancer. While we remain steadfast believers in the potential of computer simulation for better understanding cancer screening, we also understand the fundamental limitations of such an approach. Figure 3 serves as a case in point: Whereas the take home message of Figure 3 (yet to be fully verified, mind you) could easily be that women in the 40 to 55 age range may benefit from 6 month interval screening (Dr. Kopans at Mass General has reported similar observations<sup>4</sup>), there is the other implication that women aged 70 and above could be screened every three years. Of course the public health implications for imposing a longer screening interval in older women are that this would open up current screening resources for younger women who are currently not screened, since screening resources are finite. The effect of such a policy shift, if the data in Figure 3 are correct, is that fewer years of life would be lost to breast cancer nationwide (we acknowledge that other considerations factor into this). The ethical dilemma is common to public health care policy: Public health care policies are designed to enhance health at the population level, but certain recommendations may detrimentally impact health at the personal level for some minority of the population. With respect to the results of Figure 3, while a 75 year old women may strongly reject the notion of increasing her screening interval since she personally will receive less preventative health care – similar policies are common in other areas of health care (almost all disease screening is targeted towards high risk groups). The only conclusion to make here is to observe that at some point in time down the road in this research area, the use of medical ethicists may be necessary to help guide how the results of this type of research should be (or should not be) translated into health care policy.



## REFERENCES

1. P. S. Rezentes, A. de Almeida, and G. T. Barnes, "Mammography grid performance.", *Radiology* **210**, 227-232 (1999)
2. X. Wu, E. L. Gingold, G. T. Barnes, and D. M. Tucker, "Normalized average glandular dose in molybdenum target-rhodium filter and rhodium target-rhodium filter mammography.", *Radiology* **193**, 83-89 (1994)
3. X. Wu, G. T. Barnes, and D. M. Tucker, "Spectral dependence of glandular tissue dose in screen-film mammography.", *Radiology* **179**, 143-148 (1991)
4. J. S. Michaelson, E. Halpern, and D. B. Kopans, "Breast cancer: computer simulation method for estimating optimal intervals for screening.", *Radiology* **212**, 551-560 (1999)

## **APPENDICES**

- Appendix 1** JM Boone, JA Seibert, JM Sabol, and M Tecotzky, "A Monte Carlo study of x-ray fluorescence in x-ray detectors", Medical Physics 26, 905-916 (1999)
- Appendix 2** VN Cooper, JM Boone, and JA Seibert, "A lesion detectability simulation method for digital x-ray imaging", Medical Physics 27;66-74 (2000)
- Appendix 3** VN Cooper, JM Boone, and JA Seibert, C Pellot-Barakat, "An edge spread technique for measurement of the scatter to primary ratio in mammography", Medical Physics 27: 845-853 (2000)
- Appendix 4** JM Boone, "Glandular breast dose for monoenergetic and high-energy x-ray beams: Monte Carlo assessment", Radiology 213, 23-37 (1999)
- Appendix 5** Manuscript entitled "Relating ROC curve area ( $A_z$ ) to sensitivity and specificity with application to mammography"

## Appendix 5

---

# Relating ROC curve area ( $A_z$ ) to sensitivity and specificity with application to mammography

---

John M. Boone, Ph.D.  
Karen K. Lindfors, M.D.  
J. Anthony Seibert, Ph.D.  
†Mary N. Haan, Ph.D.

Department of Radiology  
University of California – Davis  
Sacramento, California 95817

†Department of Epidemiology and Preventive Medicine  
University of California – Davis  
Davis, California 95616

### ADDRESS FOR CORRESPONDENCE:

John M. Boone, Ph.D.  
Department of Radiology  
UC Davis Medical Center  
4701 X Street, Research Imaging Center  
Sacramento, CA 95817  
(916) 734-3158 (Voice & Voice Mail)  
(916) 734-0316 (FAX)  
jmboone@ucdavis.edu

### KEY WORDS:

Breast cancer, mammography, positive predictive value, sensitivity, specificity, ROC curves, positive biopsy rates, cancer detection rates, screening.

---

# Relating ROC curve area ( $A_z$ ) to sensitivity and specificity with application to mammography

---

## KEY WORDS:

Breast cancer, mammography, positive predictive value, sensitivity, specificity, ROC curves, positive biopsy rates, cancer detection rates, screening.

# Abstract

**Purpose:** The sensitivity and specificity of screening mammography has been the topic of many research studies. We have developed a technique, based on receiver operating characteristic (ROC) curve analysis of area under the curve (so-called  $A_z$ ), which when combined with the positive biopsy rate and cancer detection rates for breast cancer, can be used to calculate sensitivity and specificity.

**Methods:** The theory is developed mathematically, and the resulting expressions are used to calculate tables of sensitivity and specificity over realistic ranges of cancer detection rates,  $A_z$  values, and positive biopsy rates reported in the literature. **Results:** The results demonstrate that for  $A_z < 0.95$ , the sensitivity will generally be less than 50%. In the high range of  $A_z$  values (above 0.95), an increase in  $A_z$  by 1% (by 0.01 units of area) can increase sensitivity by as much as 10%. Lower positive biopsy rates (i.e. lower positive predictive values) correlate with better sensitivity and specificity. Higher cancer detection rates improve the sensitivity, holding other factors constant. **Conclusions:** A model requiring three input parameters ( $A_z$ , the cancer detection rate, and the positive biopsy rate) was developed which is able to identify the operating point on the ROC curve, and therefore sensitivity and specificity can be directly computed.

## Introduction

Mammographic screening is considered to be an essential component of breast cancer control. Despite the importance of mammography, it is difficult to determine its exact sensitivity and specificity. Furthermore, efforts to determine single values for these parameters sometimes confuse the fact that the sensitivity of screening for a woman with breast cancer increases over time, as the lesion increases in both diameter and subject contrast. These changes increase its probability of being detected with successive screens. Characterizing the sensitivity of mammography by a single value, when the screened population has a variety of lesion sizes and densities, averages a wide range of sensitivity values together. Clearly the sensitivity of detecting 20 mm breast lesions using mammography is substantially higher than detecting 2 mm breast lesions that are isodense with glandular breasts.

The determination of sensitivity requires quantifying the number of true positive and false negative cases. True positive cases are those patients who have been diagnosed with breast cancer that actually have breast cancer, and false negatives are those patients who were diagnosed as being normal, but who actually harbor the disease. Quantifying the number of true positive cases is relatively easy, since they represent a very small fraction of women who visit the screening mammography clinic, and their outcome is determined by biopsy shortly following screening. False negatives, however, are by definition unknown cases, and the fraction of negative screens that pass through the mammography clinic is extremely high, making this a harder group to track in terms of sheer numbers.

There are a number of reports in the literature in which the receiver operating characteristic (ROC) curve has been measured for radiologists performing mammography<sup>1-6</sup>. There are also many reports of the positive biopsy rate which results from breast screening<sup>7-16</sup>. ROC curve analysis is often used as a test comparing two diagnostic techniques, and the area under the ROC curve (called  $A_z$ ) is a useful parameter that is related to lesion detectability. However, the  $A_z$  value is not the actual *probability* of detecting a lesion – the probability of detecting a lesion, when one is present, is given by the sensitivity. After performing ROC analysis, it is sometimes desirable to know precisely where on the ROC curve the radiologist actually operates (the operating point). Knowledge of the operating point leads directly to an assessment of sensitivity and specificity.

In this work, a method based on signal detection theory (which is the basis of the ROC methodology) is presented which allows the identification of the operating point on the ROC curve, and

thus the sensitivity and specificity can be calculated directly. The technique requires three input variables: the area under the ROC curve ( $A_z$ ), the positive biopsy rate, and the cancer detection rate.

# Methods

## BASIC SIGNAL DETECTION THEORY

Figure 1 illustrates two normally distributed (Gaussian) curves, where  $C(\xi)$  corresponds to the population with cancer and  $N(\xi)$  corresponds to the normal (non-cancer) population. The  $N(\xi)$  distribution has a mean of  $\bar{N}$  and standard deviation  $\sigma$ , and the  $C(\xi)$  distribution has a mean of  $\bar{C}$  and the same standard deviation  $\sigma$ . The area of these two curves have arbitrarily been set equal to each other. The decision parameter,  $\xi$ , is some quantifiable entity that allows one to make a decision concerning a diagnosis. For most radiologist-interpreted images, including mammograms,  $\xi$  corresponds to the radiologist's impression. The radiologist's diagnosis is dependent upon a number of factors, including the assessment of the pertinent anatomy and pathology visible on the mammogram, and other patient information such as age, family history, hormone replacement therapy, etc. The decision parameter may be considered as the radiologist's *gestalt*. In computer-analyzed images, the value of  $\xi$  may be the numerical output of a computer aided diagnostic routine.

The signal to noise ratio (SNR) between the normal  $N(\xi)$  and cancer  $C(\xi)$  populations shown in Figure 1 is related to the lateral shift between the means of the distributions, and is given by:

$$SNR = \frac{\bar{C} - \bar{N}}{\sigma} \quad \text{Eq. 1}$$

A decision threshold is illustrated in Figure 1 as the vertical line marked  $\tau$ , and all patients with a value of  $\xi$  to the right of  $\tau$  are considered by the diagnostician as having cancer, and all patients to the left of  $\tau$  are considered normal. As indicated in Figure 1, patients in the cancer population to the right of  $\tau$  are correctly diagnosed and are considered true positives (TP), and the cancer population to the left of  $\tau$  are false negatives (FN). The normal population to the left of  $\tau$  are true negatives (TN), and those to the right of  $\tau$  are false positives (FP). Mathematically, these terms can be defined as:



$$FP(\tau) = \int_{\tau}^{\infty} N(\xi) d\xi \quad \text{Eq. 2}$$

$$TN(\tau) = \int_{-\infty}^{\tau} N(\xi) d\xi \quad \text{Eq. 3}$$

$$TP(\tau) = \int_{\tau}^{\infty} C(\xi) d\xi \quad \text{Eq. 4}$$

$$FN(\tau) = \int_{-\infty}^{\tau} C(\xi) d\xi \quad \text{Eq. 5}$$

The *sensitivity* of a medical test is the fraction of cases in which the patient is diagnosed as being disease-positive, when they truly have the disease. The sensitivity depends on the selection of the threshold value  $\tau$ , and thus:

$$sensitivity(\tau) = \frac{TP(\tau)}{TP(\tau) + FN(\tau)} \quad \text{Eq. 6}$$

The sensitivity is a measure of the performance of a diagnostic test amongst those who truly have the disease, and is equivalent to the probability of detection of that disease. The specificity of a medical test represents the fraction of cases in which the patient is diagnosed as disease-free, when they truly are. The specificity is also dependent upon the threshold value  $\tau$ :

$$specificity(\tau) = \frac{TN(\tau)}{TN(\tau) + FP(\tau)} \quad \text{Eq. 7}$$

The specificity is a metric which describes the performance of a diagnostic test amongst those who truly do not have the disease that the test is designed to detect.

The receiver operating characteristic (ROC) curve is a plot of the sensitivity( $\tau$ ) as a function of (1-specificity( $\tau$ )), as shown in Figure 2. Each point on the ROC curve corresponds to a pair of coordinates ( $x, y$ ), where  $x = 1 - specificity(\tau)$ , and  $y = sensitivity(\tau)$ . Each point on the ROC curve

depends on the specific value of  $\tau$ , and thus different points on the ROC *curve* are produced by varying  $\tau$ . For example, by sweeping  $\tau$  from left to right across Figure 1, Eqs. 2-5 are used to calculate  $FP(\tau)$ ,  $TN(\tau)$ ,  $TP(\tau)$ , and  $FN(\tau)$  at each threshold value, and Eqs. 6 and 7 are used to calculate the subsequent  $\tau$ -dependent values of sensitivity( $\tau$ ) and specificity( $\tau$ ). For example, the ROC curve will have 7 points on it, if 7 values of  $\tau$  were evaluated (Figure 2).

The total number of cancer cases is given by the area of the curve  $C(\xi)$  in Figure 1. Mathematically, the total cancer population,  $P_c$ , is:

$$P_c = P f = \int_{-\infty}^{\infty} C(\xi) d\xi \quad \text{Eq. 8}$$

where  $P$  is the total population, and  $f$  is the fraction of the population with cancer. The total number of normal cases in the population,  $P_N$ , is given by:

$$P_N = P (1 - f) = \int_{-\infty}^{\infty} N(\xi) d\xi \quad \text{Eq. 9}$$

The incidence of a disease is the fraction,  $f$ , of the total population at a given window in time that has the disease:

$$\text{incidence} = f = \frac{P_c}{P_c + P_N} \quad \text{Eq. 10}$$

The sensitivity and specificity are parameters which are *independent* of the incidence in the population, and therefore the value of  $f$  in equations 8 and 9 does not affect sensitivity or specificity.

## BIOPSY RATES IN MAMMOGRAPHY

When a radiologist, based on mammographic images and other ancillary information, recommends a breast biopsy, he or she is stating that there is a reasonable chance that the patient has breast cancer. The assumption is that all patients sent to biopsy appear more abnormal than all those

who are not sent to biopsy. When screening mammography in addition to subsequent tests performed prior to biopsy (such as additional mammographic views, ultrasound, the clinical breast examination, etc.) are considered together (diagnostic work-up), then all those sent to biopsy have been called as “positive”, and represent the sum of the true positives and the false positives, as determined by the imaging work-up. The biopsy is considered the gold standard, and those patients who come back with positive biopsies represent the true positive population. Therefore, the positive biopsy rate is equal to the positive predictive value (PPV) of the comprehensive imaging and clinical examination for breast cancer. We also note that the PPV is dependent upon the threshold value  $\tau$ , discussed in the previous section.

$$PBR(\tau) = PPV(\tau) = \frac{TP(\tau)}{TP(\tau) + FP(\tau)} \quad \text{Eq. 11}$$

Unlike the sensitivity and the specificity, the PPV is *dependent* upon the incidence of disease in the total population (and therefore is dependent upon  $f$  in Eqs. 8 and 9). The cancer detection rate is a straightforward proxy for incidence, and is typically expressed in the units of *cancers detected per 1000 screens*. The cancer detection rate typically ranges from around 2 to upwards of 10 cancers detected per 1000 screens<sup>7,17,18</sup>, depending upon the age group being screened. Prevalence screens (first screen) typically yield greater numbers of cancers than do subsequent, incidence screens, and screening programs with greater time intervals between screening examinations report higher cancer detection rates (per screen) as well. The incidence of breast cancer in the United States is about 1.0, 2.8, 3.8, and 4.8 cancers per 1000 women for women ages 40, 50, 60, and 70, respectively<sup>19</sup>.

## ROC CURVES

While the specific example of mammography will be discussed here, this discussion is general and applies to other disease processes as well. An ROC curve for a mammographer is a plot of the trade-off between sensitivity( $\tau$ ) and specificity( $\tau$ ), as the radiologist modulates her threshold value  $\tau$ . The ROC curve is an indicator of the diagnostician’s performance, independent of the threshold value ( $\tau$ ) that a given diagnostician may use. Using a binormal (dual-gaussian) assumption, ROC curves have a characteristic appearance as shown in Figure 2. The area under the ROC curve is a single number

which describes the diagnostic performance of a radiologist (or of a diagnostic test). The maximum possible area under the ROC curve is unity indicating perfect diagnostic performance, and an area of 0.5 (diagonal line) indicates worst performance. ROC curves which bow significantly below the diagonal are indicative of a diagnostic test which implies that the disease is present when it's not, and visa versa. The area under the ROC is traditionally given the symbol  $A_z$ .

Note that the ROC curve is just a graphical representation of the SNR (Eq. 1). Figure 2 illustrates ROC curves for SNR's of 1, 2 and 3. A low SNR corresponds to two populations ( $C(\xi)$  and  $N(\xi)$  as seen in Figure 1) which have less separation, and a high SNR corresponds to larger separations between the two populations means, i.e. where  $(\bar{C} - \bar{N})$  is larger. For a given SNR, the area under the corresponding ROC curve can be calculated based on binormal distributions with equal variance. Consequently, the relationship between SNR and  $A_z$  is illustrated in Figure 3. For a SNR of 0,  $A_z = 0.5$ , corresponding to pure guessing. As the SNR approaches 4,  $A_z$  approaches unity, where ideal performance is realized. Specifically,  $A_z = 0.95$  at an SNR of 2.4,  $A_z > 0.99$  at an SNR of 3.4, and  $A_z > 0.999$  at an SNR of 6.5. According to the classic work of Rose<sup>20</sup>, if the SNR  $> 5.0$  (the "*Rose Criterion*"), then an object such as a breast lesion will almost certainly be detectable.

Sensitivity and specificity are independent of incidence, but the positive predictive value is not. Therefore, to assess the PPV, the normal and cancer populations have to be properly normalized with respect to each other. Figure 4 illustrates the normal and cancer populations, with the area of the cancer population equal to the cancer detection rate (2/1000 was used in the figure), and the area of the normal population is equal to  $1000 - \text{CDR}$  (998 was used in the figure). The distributions shown in Figure 4 are Gaussian, but the ordinate is logarithmic and this distorts their shape. A logarithmic scale was necessary to show both curves on the same plot, since their areas are so disparate.

## ROC CURVES AND SENSITIVITY

There is a certain fallacy in measuring the sensitivity and specificity of mammography, since the size of breast cancers present in the screening population varies from small, non-detectable lesions, to large, easily detectable lesions. In principal, the sensitivity and specificity of mammography should be discussed in terms of lesion diameter. In addition, dense breasts are known to reduce the ability of the mammographer to identify breast lesions, and therefore breast density has an impact on sensitivity and

specificity of mammography. For the same size breast lesion, lesions in dense breasts will demonstrate lower detectability (lower  $A_z$ ) than lesions in fatty-replaced (non-dense) breasts.

With the above caveats stated, there is nevertheless an obvious interest on the part of many<sup>21-28</sup> in estimating the performance of mammography. Determining the sensitivity is difficult, because accurately assessing the number of false negatives (see Eq. 6) requires lengthy follow-up. Furthermore, in a practice where perhaps 3 cases out of 1000 screens have cancer, the negatives (including FN and TN) far outnumber the positives (including TP and FP). While methods are available to assess the ROC performance of mammographers using clinical performance tests<sup>29-32</sup>, it is not straightforward how the ROC curve by itself can be used to estimate sensitivity and specificity<sup>33</sup>. Put differently, the ROC curve allows the  $A_z$  value to be computed, but it is not generally straightforward to deduce the point on the ROC curve where the mammographer actually operates. Nevertheless, the  $A_z$  performance of radiologists<sup>2,4,5</sup> and computer aids<sup>1,3-6</sup> have been reported frequently in the literature. The contribution of the present work is to introduce a technique in which the operating point on the ROC where the mammographer actually functions can be determined. From the determination of this point on the ROC curve, the sensitivity and specificity can be computed. In addition to the ROC curve (or rather it's shorthand indicator,  $A_z$ ), the breast cancer detection rate needs to be known, and the positive biopsy rate (positive predictive value) needs to be known as well.

The positive biopsy rate for mammography and the cancer detection rate for a population should be audited for every radiologist under the Mammography Quality Standards Act (MQSA). Typical published values<sup>5,7-16,18,34</sup> for the positive biopsy rate range from approximately 20% to 40%. Let us assume that the average positive biopsy rate for mammography is 25%. The PPV( $\tau$ ) can be computed from the  $A_z$  value assuming that the cancer detection rate for the screening population is also known. This being the case, the value of  $\tau$  can be found to yield the desired PPV( $\tau$ ), 25% in our example here. Once  $\tau$  is determined from the cancer detection rate and the PPV( $\tau$ ), it can be used with the ROC curve (i.e.  $A_z$ ) to calculate the sensitivity using Eqs. 2, 3 and 6. Specificity can be also calculated from  $\tau$  using Eqs. 4, 5 and 7. The details of the calculations are presented in the appendix.

## Results

Figure 5 shows the sensitivity as a function of the PPV, for a cancer detection rate of 2 in Fig. 5A, and a CDR=4 in Fig. 5B. Curves for different  $A_z$  values are shown in each figure. For practical biopsy rates in the range of 20-40%, the sensitivity is below 10% for  $A_z=0.90$ , and rises to a more reasonable 70% to 80% for  $A_z=0.99$ . The curves on the bottom graph (Fig. 5B) are slightly higher than those on top, indicating that a higher CDR improves the sensitivity at the same biopsy rate and  $A_z$ . It is clear from both curves that a very high  $A_z$  value is crucial to good sensitivity.

Figure 6 illustrates the trend in sensitivity as a function of  $A_z$  value, for different PPVs as indicated in the figures. The two figures shown are for a CDR=2 (Fig. 6A) and CDR=4 (Fig. 6B). In the United States, the CDR at most breast screening clinics will usually be between these values for a previously screened population with a typical age distribution. It is worth noticing that for PPVs in the reasonable 20-40% range, an  $A_z$  of 0.90 is required to achieve just 10% sensitivity for CDR=2 and an  $A_z$  of 0.87 is required in a population with CDR = 4 to achieve 10% sensitivity..

Figure 7 illustrates the same data set from a different perspective, showing sensitivity as a function of the cancer detection rate. In the early days of breast screening, some reports indicate CDR's as high as 15 and above, however that would be considered very high today. The CDR values from 1 to 5 are more representative of modern clinical breast cancer screening.

Tables 1 through 16 give the sensitivity (odd-numbered tables) and specificity (even-numbered tables) for biopsy rates from 5% to 95%, and for  $A_z$  values from 0.70 to 0.99. Each pair of tables is for different CDRs, and tables are given for CDRs of 1, 2, 3, 4, 5, 6, 8, and 10 per 1000 screens. The tables should be useful in determining the sensitivity and specificity over a range of detectability ( $A_z$ ) and over a wide range in biopsy rates.

## Discussion

Reported values for radiologist  $A_z$  performance in screening mammography alone vary widely, with reports of  $A_z$  values of 0.61<sup>5</sup>,  $A_z = 0.81$ <sup>3</sup>,  $A_z = 0.83$ <sup>4</sup> to  $A_z = 0.94$ <sup>2</sup>. The variability is likely due to differences in radiologist performance<sup>27</sup> and variation in the degree of diagnostic difficulty of the databases used for testing<sup>35</sup>. In one study reported by experienced investigators, an improvement from an  $A_z$  of 0.61 for the radiologist-interpreted screening mammogram was increased to  $A_z = 0.75$  when the radiologist was aided by a CAD program. These values were reported with a PPV of 46-55%<sup>5</sup>. Using a realistic CDR of 3 cancers per 1000 screens, the sensitivity from Table 5 corresponding to  $A_z=0.75$  and PPV=50% is 0%! How can this be? The answer lies in the fact that virtually all ROC studies make use of *enriched* data bases, where the percentage of cancers is much higher than that seen in the screening mammography setting. The ROC example<sup>5</sup> used a database of 46 cancers and 58 benign cases, resulting in a 44.2% cancer rate and therefore a CDR of 442 cancers per 1000 screens. Putting  $A_z=0.61$ , PPV=50%, and CDR=442 into the proposed model results in a sensitivity of 75.5% for the radiologist alone (specificity=40.2%), and with the help of the computer aid, the sensitivity improved to 95.5% (for parameters  $A_z=0.74$ , PPV=50%, CDR=442), with specificity=24.3%. Notice that these specificity values would be increased markedly with the additional diagnostic work-up beyond screening mammography. As this example demonstrates, when used in evaluating ROC results, the model proposed here should use the enrichment factor used in the ROC study as the cancer detection rate. It should be noted, however, that radiologists may (and probably do) alter their threshold value when participating in ROC studies, in response to the huge increase in cancers (or other abnormal findings) seen in the ROC setting. This suggests the need for studies aimed at comparing ROC performance as a function of the enrichment factor used.

Once a potential abnormality is discovered on a screening mammogram, an array of other diagnostic tools may be used to further evaluate that area of the breast, including comparison with previous films, breast ultrasound, the use of additional mammographic views, a clinical breast examination, and short interval follow-up for probably benign lesions. Research concerning the potential role of other procedures such as magnetic resonance imaging, scintimammography, and computer aided diagnosis is also under way. Some combination of additional diagnostic procedures are performed on the patient under most circumstances, prior to a recommendation for biopsy. These

additional procedures act to increase the  $A_z$  value beyond that of screening mammography<sup>3,5</sup> (Figure 6). Consequently, the diagnostic evaluation will almost certainly have better ROC performance (higher  $A_z$ ) than screening mammography by itself. Most ROC studies are performed using only the screening mammography image, and therefore most  $A_z$  values reported in the literature are representative of screening mammography only, not a complete diagnostic evaluation. However, most PPVs reported in the literature are indicative of the performance of a comprehensive diagnostic work-up. The additional tests that are a part of the comprehensive diagnostic evaluation serve to drive the PPV up, since many abnormalities are shown to be benign using these additional tests, and consequently fewer biopsies are performed.

Consistency is important, if the model presented here is to be used. If an  $A_z$  value determined in the screening mammography setting is used as input to the model, the PPV based only on screening mammography (and not from diagnostic work-up) should also be used. Under these conditions, the sensitivity and specificity calculated will be indicative of only screening mammography. A more realistic measure of the sensitivity and specificity performance of breast cancer screening will be that determined from the  $A_z$  value and PPV resulting from complete diagnostic evaluation.

Determination of the sensitivity from the ROC curve performance is useful for estimating the probability of breast cancer detection among those who have the disease. This probability is needed for the development of computer models designed to simulate the overall performance of breast cancer screening<sup>36</sup>. Understanding how the detection probability changes as a function of lesion size is also an important consideration that requires further research.

It is fortunate that the sensitivity and specificity are independent of the cancer detection rate (i.e. incidence), because for practical reasons ROC studies need to make use of enriched data bases, where the incidence is artificially inflated by several orders of magnitude. However, when applying ROC performance metrics to incidence-dependent parameters such as the positive predictive value, the incidence needs to be considered. Furthermore, as we have shown, ROC evaluation of the diagnostic performance of the screening mammogram by itself should not be considered to be representative of clinical reality. Realistic tests designed to assess the net contribution of adjuncts such as breast MRI or computed aided diagnosis should seek to compare the performance of the diagnostic examination (including ultrasound, additional views, the clinical breast examination, etc.) against the diagnostic examination plus the adjunct (e.g. MRI or CAD) to be assessed. Using ROC results based only on the evaluation of screening mammography, with and without the adjunct being assessed, will almost



certainly inflate the benefit of the adjunct, as it will essentially fill the void left by excluding the additional studies performed in the more comprehensive diagnostic evaluation. Nevertheless, we recognize that the methodology required for assessing the ROC performance of the entire diagnostic breast cancer examination is ill-defined, and will certainly be more complex when multiple branching decision pathways are considered.

## **Acknowledgements**

This research was supported in part by grants from the US Army Breast Cancer Research Program (DAMD17-98-1-8176 and DAMD17-94-J-4424).

## Appendix

The mathematical formulae necessary to compute sensitivity (and specificity) from the cancer detection rate (CDR), value, and PPV are presented below. The emphasis here is on how to concisely perform the calculations, not on a full analytical discussion of the details.

The integral of a Gaussian is the complementary error function, ERFC:

$$\int_{\tau}^{\infty} e^{-\alpha x^2} dx = k \text{ ERFC}(\tau \sqrt{\alpha}) \quad \text{A-1}$$

where the complementary error function ERFC is related to the error function ERF by:

$$\text{ERFC}(x) = 1 - \text{ERF}(x) \quad \text{A-2}$$

The normal distribution is given by:

$$p(x) = e^{-\frac{1}{2} \frac{(x - \mu)^2}{\sigma^2}} \quad \text{A-3}$$

Since the value of  $\sigma$  is relative to the signal (when discussing the SNR), we set  $\sigma = 1$ . This means that the axis of the decision variable is in the units of  $\sigma$ , as shown in Figure 8. We place the mean of the normal population  $\bar{N}$  at zero, and since the axis is in units of  $\sigma$ , the mean of the cancer population  $\bar{C}$  will be offset from zero by the signal to noise ratio, SNR. For the normal population,  $N(\xi)$ , since  $\sigma=1$  and  $\mu=0$ , plugging  $p(x)$  from Eq. A-3 into Eq. A-1 yields a value of  $\alpha = 1/2$ .

To simplify the normalization, we define a *modified* error function  $\text{MERF}(x)$ , where:

$$\text{MERF}(x) = \frac{1}{2} (1 + \text{ERF}(x)) \quad \text{A-4}$$

The redefined function  $MERF(x)$  scales such that the minimum is zero (for  $x \ll 0$ ) and the maximum is unity (for  $x \gg 0$ ). We similarly define a modified complimentary error function,  $MERFC(x)$ , where:

$$MERFC(x) = 1 - MERF(x) \quad A-5$$

$MERFC(x)$  also scales between zero and unity. Letting the area of the total population (the sum of the normal population and the cancer population) be unity, and letting the fraction of the population that has cancer be  $f_{cdr}$ , (i.e.  $f_{cdr} = 0.001 \times CDR$ ), the false positive fraction is given by:

$$FP(\tau) = (1 - f_{cdr}) \times MERFC\left(\tau \sqrt{\frac{1}{2}}\right) \quad A-6$$

The true negative fraction is given by:

$$TN(\tau) = (1 - f_{cdr}) \times MERF\left(\tau \sqrt{\frac{1}{2}}\right) \quad A-7$$

Because of the cancer population is shifted to the right from zero by the SNR, a change in variable is required for integration. Letting

$$\tau' = \tau - SNR \quad A-8$$

then the true positive fraction is given by:

$$TP(\tau) = f_{cdr} \times MERFC\left(\tau' \sqrt{\frac{1}{2}}\right) \quad A-9$$

And the false negative fraction is given by:

$$FN(\tau) = f_{cdr} \times MERF\left(\tau' \sqrt{\frac{1}{2}}\right) \quad A-10$$

Equations A-6 through A-10 are the properly normalized analytical solutions to Eqs. 2 through 5 discussed in the Methods section.

The SNR was fit to the  $A_z$  value (Figure 3), and the computerized fit is given by:

$$SNR = \frac{a + c \ln(x) + e \ln(x)^2 + g \ln(x)^3 + i \ln(x)^4 + k \ln(x)^5}{1 + b \ln(x) + d \ln(x)^2 + f \ln(x)^3 + h \ln(x)^4 + j \ln(x)^5} \quad A-11$$

where  $x = A_z$ , and the valid range for  $A_z$  is from 0.5 to 0.999. This fit yielded  $r^2 = 0.999999833$ .

The coefficient values are:

$a = 4.437387478757548$	$e = 1718.336644943578$	$i = 4221.784373695074$
$b = -142.908934776169$	$f = 634.3198806220385$	$j = -409.7642881382754$
$c = -407.4569847684826$	$g = 6816.717899798747$	$k = -1144.693365532518$
$d = 1512.141388072441$	$h = -2962.319327288902$	

The algorithm for finding the sensitivity (or specificity) from  $A_z$ ,  $f_{cdr}$ , and the PPV proceeds as follows:

1. The  $A_z$  value is converted to SNR using Eq. A-10.
2. The values of TN, TP, FN, and FP are calculated as a function of  $\tau$ , using Eqs. A-6 through A-9, and the desired PPV (Eq. 10) is determined iteratively. This yields the value of  $\tau$ , and thus the operating point on the ROC curve.
3. The value of  $\tau$  is used to calculate sensitivity using Eq. 6.
4. The value of  $\tau$  is used to calculate specificity using Eq. 7.

## References

1. K. G. Gilhuijs, M. L. Giger, and U. Bick, "Computerized analysis of breast lesions in three dimensions using dynamic magnetic-resonance imaging.", *Med.Phys.* **25**, 1647-1654 (1998)
2. B. Sahiner, H. P. Chan, N. Petrick, M. A. Helvie, and M. M. Goodsitt, "Computerized characterization of masses on mammograms: the rubber band straightening transform and texture analysis.", *Med.Phys.* **25**, 516-526 (1998)
3. G. M. Kacł, P. Liu, J. F. Debatin, E. Garzoli, R. F. Caduff, and G. P. Krestin, "Detection of breast cancer with conventional mammography and contrast-enhanced MR imaging.", *Eur.Radiol.* **8**, 194-200 (1998)
4. J. S. Lin, A. Hasegawa, M. T. Freedman, and S. K. Mun, "Differentiation between nodules and end-on vessels using a convolution neural network architecture.", *J.Digit.Imaging* **8**, 132-141 (1995)
5. Y. Jiang, R. M. Nishikawa, R. A. Schmidt, C. E. Metz, M. L. Giger, and K. Doi, "Improving breast cancer diagnosis with computer-aided diagnosis.", *Acad.Radiol.* **6**, 22-33 (1999)
6. J. Y. Lo, J. A. Baker, P. J. Kornguth, J. D. Iglehart, and C. E. Floyd, Jr., "Predicting breast cancer invasion with artificial neural networks on the basis of mammographic features.", *Radiology* **203**, 159-163 (1997)
7. L. G. Arnesson, B. Vitak, J. C. Manson, G. Fagerberg, and S. Smeds, "Diagnostic outcome of repeated mammography screening.", *World J.Surg.* **19**, 372-377 (1995)

8. J. A. Baker, P. J. Kornguth, J. Y. Lo, M. E. Williford, and C. E. Floyd, Jr., "Breast cancer: prediction with artificial neural network based on BI-RADS standardized lexicon.", *Radiology* **196**, 817-822 (1995)
9. D. D. Dershaw, L. Loring, S. J. True, D. C. Momrow, L. Liberman, and E. A. Morris, "A comparison of screening mammography results from programs for women of different socioeconomic status.", *Cancer* **82**, 1692-1697 (1998)
10. L. M. Fedoruk, M. A. Bojm, and S. P. Bugis, "Fine-wire localization for nonpalpable mammographic abnormalities.", *Can.J.Surg.* **38**, 173-177 (1995)
11. H. M. Fenlon, N. C. Phelan, P. O'Sullivan, S. Tierney, T. Gorey, and J. T. Ennis, "Benign versus malignant breast disease: comparison of contrast-enhanced MR imaging and Tc-99m tetrofosmin scintimammography.", *Radiology* **205**, 214-220 (1997)
12. D. Gist, J. Llorente, and J. Mayer, "A clinical algorithm for the management of abnormal mammograms. A community hospital's experience.", *West J.Med.* **166**, 21-28 (1997)
13. M. N. Linver and S. B. Paster, "Mammography outcomes in a practice setting by age: prognostic factors, sensitivity, and positive biopsy rate.", *J.Natl.Cancer Inst.Monogr* **113**-117 (1997)
14. L. W. Nunes, M. D. Schnall, S. G. Orel, M. G. Hochman, C. P. Langlotz, C. A. Reynolds, and M. H. Torosian, "Breast MR imaging: interpretation model.", *Radiology* **202**, 833-841 (1997)
15. H. C. Burrell, S. E. Pinder, A. R. Wilson, A. J. Evans, L. J. Yeoman, C. W. Elston, and I. O. Ellis, "The positive predictive value of mammographic signs: a review of 425 non-palpable breast lesions.", *Clin.Radiol.* **51**, 277-281 (1996)
16. H. Gabriel, T. E. Wilson, and M. A. Helvie, "Breast cancer in women 65-74 years old: earlier detection by mammographic screening.", *AJR Am.J.Roentgenol.* **168**, 23-27 (1997)

17. M. E. Akker-van Marle, C. M. Reep-van den Bergh, R. Boer, A. Del Moral, N. Asuncun, and H. J. de Koning, "Breast cancer screening in Navarra: interpretation of a high detection rate at the first screening round and a low rate at the second round.", *Int.J.Cancer* **73**, 464-469 (1997)
18. D. B. Kopans, R. H. Moore, K. A. McCarthy, D. A. Hall, C. A. Hulka, G. J. Whitman, P. J. Slanetz, and E. F. Halpern, "Positive predictive value of breast biopsy performed as a result of mammography: there is no abrupt change at age 50 years.", *Radiology* **200**, 357-360 (1996)
19. *SEER Cancer Statistics Review, 1973-1991: Tables and graphs*, National Cancer Institute, MIN PUb. No. 94-2789, Bethesda, MD,
20. A. Rose, *Vision, Human and Electronic*, Plenum Press, New York, 1973).
21. A. I. Mushlin, R. W. Kouides, and D. E. Shapiro, "Estimating the accuracy of screening mammography: A meta-analysis.", *Am.J.Prev.Med.* **14**, 143-153 (1998)
22. S. Nawano, K. Murakami, N. Moriyama, H. Kobatake, H. Takeo, and K. Shimura, "Computer-aided diagnosis in full digital mammography.", *Invest Radiol.* **34**, 310-316 (1999)
23. N. Avril, J. Dose, F. Janicke, S. Bense, S. Ziegler, C. Laubenbacher, W. Romer, H. Pache, M. Herz, B. Allgayer, W. Nathrath, H. Graeff, and M. Schwaiger, "Metabolic characterization of breast tumors with positron emission tomography using F-18 fluorodeoxyglucose.", *J.Clin.Oncol.* **14**, 1848-1857 (1996)
24. I. Leichter, R. Lederman, P. Bamberger, B. Novak, S. Fields, and S. S. Buchbinder, "The use of an interactive software program for quantitative characterization of microcalcifications on digitized film-screen mammograms.", *Invest Radiol.* **34**, 394-400 (1999)



25. G. S. Cooper, Z. Yuan, K. C. Stange, L. K. Dennis, S. B. Amini, and A. A. Rimm, "The sensitivity of Medicare claims data for case ascertainment of six common cancers.", *Med.Care* **37**, 436-444 (1999)
26. S. Ciatto, M. R. Del Turco, D. Morrone, S. Catarzi, D. Ambrogetti, A. Cariddi, and M. Zappa, "Independent double reading of screening mammograms.", *J.Med.Screen.* **2**, 99-101 (1995)
27. C. A. Beam, P. M. Layde, and D. C. Sullivan, "Variability in the interpretation of screening mammograms by US radiologists.", *Archives of Internal Medicine* **156**, 209-213 (1996)
28. M. S. Pep, N. Urban, C. Rutter, and G. Longton, "Design of a study to improve accuracy in reading mammograms.", *Journal of Clinical Epidemiology* **50**, 1327-1338 (1997)
29. D. D. Dorfman, K. S. Berbaum, and C. E. Metz, "Receiver operating characteristic rating analysis. Generalization to the population of readers and patients with the jackknife method.", *Invest Radiol.* **27**, 723-731 (1992)
30. H. E. Rockette, D. Gur, and C. E. Metz, "The use of continuous and discrete confidence judgments in receiver operating characteristic studies of diagnostic imaging techniques.", *Invest Radiol.* **27**, 169-172 (1992)
31. D. Gur, H. E. Rockette, W. F. Good, B. S. Slasky, L. A. Cooperstein, W. H. Straub, N. A. Obuchowski, and C. E. Metz, "Effect of observer instruction on ROC study of chest images.", *Invest Radiol.* **25**, 230-234 (1990)
32. C. E. Metz and J. H. Shen, "Gains in accuracy from replicated readings of diagnostic images: prediction and assessment in terms of ROC analysis.", *Med.Decis.Making* **12**, 60-75 (1992)
33. Y. Jiang, C. E. Metz, and R. M. Nishikawa, "A receiver operating characteristic partial area index for highly sensitive diagnostic tests .", *Radiology* **201**, 745-750 (1996)

34. R. Bellantone, S. Rossi, C. P. Lombardi, C. Cinini, S. Minelli, and F. Crucitti, "Excisional breast biopsy: when, why and how?", *Int.Surg.* **80**, 75-78 (1995)
35. R. M. Nishikawa, M. L. Giger, K. Doi, C. E. Metz, F. F. Yin, C. J. Vyborny, and R. A. Schmidt, "Effect of case selection on the performance of computer-aided detection schemes.", *Med.Phys.* **21**, 265-269 (1994)
36. J. M.Boone and K. L. Lindfors, "Computer simulation of breast cancer screening efficacy.", *Med.Phys.* **26**, 1065-1066 (1999) (Abstract)

## Figure Captions

### FIGURE 1:

The basic assumptions of signal detection theory are illustrated. A screening test is designed to differentiate between two populations, the normal population  $N(\xi)$  and those patients with cancer  $C(\xi)$ . These populations are assumed to be normally distributed, with means of  $\bar{N}$  and  $\bar{C}$  respectively, and with a standard deviation  $\sigma$ . A decision parameter  $\xi$  is used as the basis of the diagnosis, and a threshold value  $\tau$  is chosen by the diagnostician (a radiologist or other decision maker). By selecting  $\tau$ , all cases of  $\xi$  to the right of the threshold ( $\xi > \tau$ ) are considered by that diagnostician as having cancer, and all cases to the left of  $\tau$  ( $\xi < \tau$ ) are considered normal.

### FIGURE 2:

An ROC curve is illustrated for data with three different signal to noise ratios (SNR), as indicated. An ROC curve is generated as a series of pairs of points, where each (1-specificity( $\tau$ ), sensitivity( $\tau$ )) point on the curve corresponds to a single threshold value  $\tau$ . Different threshold values are shown as the vertical dashed lines on the inset, and correspond conceptually to each of the solid circles shown on the SNR=2 curve. The diagonal dashed line corresponds to pure guessing, while perfect performance results in a curve touching the upper left corner of the figure. The area under the SNR=1 ROC curve,  $A_z$ , is illustrated by the gray shading.

### FIGURE 3:

The relationship between signal to noise ratio (SNR) and area under the ROC curve ( $A_z$ ) is illustrated. When the SNR = 0, the diagnostic test cannot reveal useful information and an  $A_z = 0.5$  corresponds to purely guessing. Values of  $A_z$  less than 0.5 are generally not observed (gray area), but physically correspond to inverted diagnostic polarity (where the diagnostician calls the disease present when it's not, and visa versa).

#### FIGURE 4:

This figure is similar to Figure 1, however the number of cancer cases has been normalized to the typical cancer detection rate. The area under the curve  $C(\xi)$  (gray area) is 2, whereas the area under  $N(\xi)$  is 998, corresponding to a typical cancer detection rate of 2 cases per 1000 screens. The curves are normally distributed, but their shapes are distorted by the logarithmic ordinate axis.

#### FIGURE 5:

The sensitivity is plotted as a function of the positive predictive value (positive biopsy rate), for different  $A_z$  values as indicated in the figures. Figure 5A is plotted for a cancer detection rate (CDR) of 2 cases per 1000 screens, while Figure 5B is for a CDR of 4 cases per 1000 screens. The dramatic improvement in sensitivity with decreasing PPV is noted.

#### FIGURE 6:

The sensitivity is plotted as a function of  $A_z$ , for a range of positive predictive values (PPV) as indicated in the figures. Figure 6A is for a CDR = 2 cases per 1000 screens, and Figure 6B shows the results for a cancer detection rate of 4 cases per 1000 screens. A dramatic increase in the sensitivity occurs as  $A_z$  approaches unity. In Figure 6A representing most screening programs in the US, it is seen that for  $A_z < 0.95$ , the sensitivity ranges from a low of 14% (PPV=50%) to a high of 50% (PPV=10%).

#### FIGURE 7:

The sensitivity is shown plotted as a function of the cancer detection rate (CDR), for positive predictive values (PPVs) of 20% (Figure 7A) and 40% (Figure 7B). Most PPVs fall between these values. The sensitivity increases for higher  $A_z$  values, as noted in the last figure. The rate of change in the sensitivity with CDR, especially at the CDRs typically seen ( $CDR \approx 2$ ), also is higher for higher  $A_z$  values.

#### FIGURE 8:

The curves used for the development of the equations discussed in the Appendix are illustrated. The area of the normal population is normalized to  $1-f_{cdr}$ , and that of the cancer population is normalized to  $f_{cdr}$ , where  $f_{cdr}$  is the fractional cancer detection rate. When the units of the decision parameter are

expressed in units of the standard deviation ( $\sigma$ ), the separation between the means of the normal and cancer populations is given by the signal to noise ratio (SNR).

**Table 1: Sensitivity (%) versus Positive Predictive Value (PPV) and Area under the ROC curve (Az) for a Cancer Detection Rate = 1 cancer /1000 screens**

PPV	Az Value											
	0.70	0.75	0.80	0.85	0.90	0.92	0.94	0.95	0.96	0.97	0.98	0.99
5%	0.0	0.1	1.1	6.5	21.6	31.6	44.2	51.6	59.7	68.6	78.4	89.3
10%	0.0	0.0	0.2	2.0	10.7	18.2	29.3	36.6	45.1	55.3	67.4	82.2
15%	0.0	0.0	0.0	0.8	6.4	12.2	21.7	28.3	36.6	46.9	60.0	77.0
20%	0.0	0.0	0.0	0.4	4.2	8.8	16.9	22.9	30.7	40.9	54.3	72.7
25%	0.0	0.0	0.0	0.2	2.9	6.5	13.5	18.9	26.2	36.1	49.6	68.9
30%	0.0	0.0	0.0	0.1	2.1	5.0	11.0	15.8	22.6	32.1	45.5	65.5
35%	0.0	0.0	0.0	0.1	1.5	3.8	9.0	13.4	19.7	28.7	41.9	62.4
40%	0.0	0.0	0.0	0.0	1.1	3.0	7.4	11.3	17.1	25.7	38.6	59.3
45%	0.0	0.0	0.0	0.0	0.8	2.3	6.1	9.6	14.9	23.0	35.5	56.4
50%	0.0	0.0	0.0	0.0	0.6	1.8	5.0	8.1	12.9	20.5	32.7	53.6
55%	0.0	0.0	0.0	0.0	0.4	1.4	4.1	6.8	11.2	18.2	29.9	50.7
60%	0.0	0.0	0.0	0.0	0.3	1.0	3.3	5.6	9.6	16.1	27.2	47.8
65%	0.0	0.0	0.0	0.0	0.2	0.8	2.6	4.6	8.1	14.0	24.6	44.9
70%	0.0	0.0	0.0	0.0	0.1	0.5	2.0	3.7	6.7	12.0	21.9	41.7
75%	0.0	0.0	0.0	0.0	0.1	0.4	1.5	2.9	5.4	10.1	19.2	38.4
80%	0.0	0.0	0.0	0.0	0.0	0.2	1.0	2.1	4.2	8.2	16.4	34.7
85%	0.0	0.0	0.0	0.0	0.0	0.1	0.7	1.4	3.0	6.3	13.4	30.4
90%	0.0	0.0	0.0	0.0	0.0	0.1	0.4	0.8	1.9	4.3	10.0	25.2
95%	0.0	0.0	0.0	0.0	0.0	0.0	0.1	0.3	0.8	2.2	6.0	17.9

**Table 2: Specificity (%) versus Positive Predictive Value (PPV) and Area under the ROC curve (Az) for a Cancer Detection Rate = 1 cancer /1000 screens**

PPV	Az Value											
	0.70	0.75	0.80	0.85	0.90	0.92	0.94	0.95	0.96	0.97	0.98	0.99
5%	100.0	100.0	100.0	99.9	99.6	99.4	99.2	99.0	98.9	98.7	98.5	98.3
10%	100.0	100.0	100.0	100.0	99.9	99.8	99.7	99.7	99.6	99.5	99.4	99.3
15%	100.0	100.0	100.0	100.0	100.0	99.9	99.9	99.8	99.8	99.7	99.7	99.6
20%	100.0	100.0	100.0	100.0	100.0	100.0	99.9	99.9	99.9	99.8	99.8	99.7
25%	100.0	100.0	100.0	100.0	100.0	100.0	100.0	99.9	99.9	99.9	99.9	99.8
30%	100.0	100.0	100.0	100.0	100.0	100.0	100.0	100.0	99.9	99.9	99.9	99.8
35%	100.0	100.0	100.0	100.0	100.0	100.0	100.0	100.0	100.0	99.9	99.9	99.9
40%	100.0	100.0	100.0	100.0	100.0	100.0	100.0	100.0	100.0	100.0	99.9	99.9
45%	100.0	100.0	100.0	100.0	100.0	100.0	100.0	100.0	100.0	100.0	100.0	99.9
50%	100.0	100.0	100.0	100.0	100.0	100.0	100.0	100.0	100.0	100.0	100.0	99.9
55%	100.0	100.0	100.0	100.0	100.0	100.0	100.0	100.0	100.0	100.0	100.0	100.0
60%	100.0	100.0	100.0	100.0	100.0	100.0	100.0	100.0	100.0	100.0	100.0	100.0
65%	100.0	100.0	100.0	100.0	100.0	100.0	100.0	100.0	100.0	100.0	100.0	100.0
70%	100.0	100.0	100.0	100.0	100.0	100.0	100.0	100.0	100.0	100.0	100.0	100.0
75%	100.0	100.0	100.0	100.0	100.0	100.0	100.0	100.0	100.0	100.0	100.0	100.0
80%	100.0	100.0	100.0	100.0	100.0	100.0	100.0	100.0	100.0	100.0	100.0	100.0
85%	100.0	100.0	100.0	100.0	100.0	100.0	100.0	100.0	100.0	100.0	100.0	100.0
90%	100.0	100.0	100.0	100.0	100.0	100.0	100.0	100.0	100.0	100.0	100.0	100.0
95%	100.0	100.0	100.0	100.0	100.0	100.0	100.0	100.0	100.0	100.0	100.0	100.0

**Table 3: Sensitivity (%) versus Positive Predictive Value (PPV) and Area under the ROC curve (Az) for a  
Cancer Detection Rate = 2 cancer /1000 screens**

PPV	Az Value											
	0.70	0.75	0.80	0.85	0.90	0.92	0.94	0.95	0.96	0.97	0.98	0.99
5%	0.0	0.7	4.6	16.0	36.7	47.6	59.7	66.2	72.9	79.8	86.9	94.1
10%	0.0	0.1	1.0	6.0	20.7	30.6	43.1	50.5	58.7	67.7	77.7	88.8
15%	0.0	0.0	0.3	2.9	13.5	21.9	33.6	41.0	49.6	59.5	71.0	84.6
20%	0.0	0.0	0.1	1.6	9.5	16.6	27.3	34.4	42.9	53.1	65.6	81.0
25%	0.0	0.0	0.1	0.9	6.9	12.9	22.6	29.3	37.7	48.0	60.9	77.7
30%	0.0	0.0	0.0	0.6	5.1	10.2	18.9	25.2	33.3	43.5	56.9	74.6
35%	0.0	0.0	0.0	0.4	3.9	8.2	16.0	21.8	29.5	39.6	53.1	71.7
40%	0.0	0.0	0.0	0.2	2.9	6.5	13.5	18.9	26.2	36.1	49.6	68.9
45%	0.0	0.0	0.0	0.1	2.2	5.2	11.4	16.4	23.3	32.8	46.3	66.2
50%	0.0	0.0	0.0	0.1	1.7	4.2	9.6	14.2	20.6	29.8	43.1	63.4
55%	0.0	0.0	0.0	0.1	1.2	3.3	8.0	12.1	18.1	26.9	40.0	60.6
60%	0.0	0.0	0.0	0.0	0.9	2.6	6.6	10.3	15.8	24.1	36.9	57.6
65%	0.0	0.0	0.0	0.0	0.6	2.0	5.4	8.7	13.7	21.4	33.7	54.6
70%	0.0	0.0	0.0	0.0	0.4	1.5	4.3	7.1	11.6	18.7	30.6	51.4
75%	0.0	0.0	0.0	0.0	0.3	1.0	3.3	5.6	9.6	16.1	27.2	47.9
80%	0.0	0.0	0.0	0.0	0.2	0.7	2.4	4.3	7.6	13.4	23.7	43.9
85%	0.0	0.0	0.0	0.0	0.1	0.4	1.6	3.0	5.7	10.5	19.8	39.1
90%	0.0	0.0	0.0	0.0	0.0	0.2	0.9	1.9	3.7	7.5	15.3	33.2
95%	0.0	0.0	0.0	0.0	0.0	0.1	0.3	0.8	1.8	4.1	9.7	24.6

**Table 4: Specificity (%) versus Positive Predictive Value (PPV) and Area under the ROC curve (Az) for a  
Cancer Detection Rate = 2 cancer /1000 screens**

PPV	Az Value											
	0.70	0.75	0.80	0.85	0.90	0.92	0.94	0.95	0.96	0.97	0.98	0.99
5%	100.0	100.0	99.8	99.4	98.6	98.2	97.7	97.5	97.2	97.0	96.7	96.4
10%	100.0	100.0	100.0	99.9	99.6	99.4	99.2	99.1	98.9	98.8	98.6	98.4
15%	100.0	100.0	100.0	100.0	99.8	99.8	99.6	99.5	99.4	99.3	99.2	99.0
20%	100.0	100.0	100.0	100.0	99.9	99.9	99.8	99.7	99.7	99.6	99.5	99.4
25%	100.0	100.0	100.0	100.0	100.0	99.9	99.9	99.8	99.8	99.7	99.6	99.5
30%	100.0	100.0	100.0	100.0	100.0	100.0	99.9	99.9	99.8	99.8	99.7	99.7
35%	100.0	100.0	100.0	100.0	100.0	100.0	99.9	99.9	99.9	99.9	99.8	99.7
40%	100.0	100.0	100.0	100.0	100.0	100.0	100.0	99.9	99.9	99.9	99.9	99.8
45%	100.0	100.0	100.0	100.0	100.0	100.0	100.0	100.0	99.9	99.9	99.9	99.8
50%	100.0	100.0	100.0	100.0	100.0	100.0	100.0	100.0	100.0	99.9	99.9	99.9
55%	100.0	100.0	100.0	100.0	100.0	100.0	100.0	100.0	100.0	100.0	99.9	99.9
60%	100.0	100.0	100.0	100.0	100.0	100.0	100.0	100.0	100.0	100.0	100.0	99.9
65%	100.0	100.0	100.0	100.0	100.0	100.0	100.0	100.0	100.0	100.0	100.0	99.9
70%	100.0	100.0	100.0	100.0	100.0	100.0	100.0	100.0	100.0	100.0	100.0	100.0
75%	100.0	100.0	100.0	100.0	100.0	100.0	100.0	100.0	100.0	100.0	100.0	100.0
80%	100.0	100.0	100.0	100.0	100.0	100.0	100.0	100.0	100.0	100.0	100.0	100.0
85%	100.0	100.0	100.0	100.0	100.0	100.0	100.0	100.0	100.0	100.0	100.0	100.0
90%	100.0	100.0	100.0	100.0	100.0	100.0	100.0	100.0	100.0	100.0	100.0	100.0
95%	100.0	100.0	100.0	100.0	100.0	100.0	100.0	100.0	100.0	100.0	100.0	100.0

**Table 5: Sensitivity (%) versus Positive Predictive Value (PPV) and Area under the ROC curve (Az) for a Cancer Detection Rate = 3 cancer /1000 screens**

PPV	Az Value											
	0.70	0.75	0.80	0.85	0.90	0.92	0.94	0.95	0.96	0.97	0.98	0.99
5%	0.1	2.1	9.5	24.8	47.3	57.7	68.7	74.2	79.8	85.4	90.9	96.1
10%	0.0	0.2	2.4	10.5	28.8	39.4	52.0	59.1	66.5	74.5	83.0	91.9
15%	0.0	0.0	0.8	5.5	19.7	29.4	41.9	49.3	57.6	66.7	76.9	88.3
20%	0.0	0.0	0.4	3.2	14.3	22.9	34.8	42.2	50.7	60.5	71.9	85.1
25%	0.0	0.0	0.2	2.0	10.7	18.3	29.4	36.6	45.2	55.3	67.5	82.2
30%	0.0	0.0	0.1	1.3	8.2	14.8	25.1	32.0	40.4	50.7	63.4	79.5
35%	0.0	0.0	0.0	0.8	6.3	12.1	21.5	28.1	36.3	46.6	59.7	76.8
40%	0.0	0.0	0.0	0.5	4.9	9.9	18.5	24.7	32.7	42.9	56.2	74.2
45%	0.0	0.0	0.0	0.4	3.8	8.1	15.8	21.6	29.3	39.4	52.9	71.5
50%	0.0	0.0	0.0	0.2	2.9	6.5	13.5	19.0	26.3	36.1	49.6	68.9
55%	0.0	0.0	0.0	0.1	2.2	5.3	11.4	16.5	23.3	32.9	46.3	66.2
60%	0.0	0.0	0.0	0.1	1.7	4.2	9.6	14.2	20.6	29.8	43.1	63.4
65%	0.0	0.0	0.0	0.1	1.2	3.3	7.9	12.0	18.0	26.7	39.8	60.4
70%	0.0	0.0	0.0	0.0	0.9	2.5	6.4	10.0	15.4	23.7	36.3	57.2
75%	0.0	0.0	0.0	0.0	0.6	1.8	5.0	8.1	13.0	20.5	32.7	53.6
80%	0.0	0.0	0.0	0.0	0.4	1.2	3.7	6.3	10.5	17.3	28.8	49.5
85%	0.0	0.0	0.0	0.0	0.2	0.7	2.6	4.6	8.0	13.9	24.4	44.6
90%	0.0	0.0	0.0	0.0	0.1	0.4	1.5	2.9	5.4	10.1	19.2	38.4
95%	0.0	0.0	0.0	0.0	0.0	0.1	0.6	1.3	2.7	5.7	12.5	29.1

**Table 6: Specificity (%) versus Positive Predictive Value (PPV) and Area under the ROC curve (Az) for a Cancer Detection Rate = 3 cancer /1000 screens**

PPV	Az Value											
	0.70	0.75	0.80	0.85	0.90	0.92	0.94	0.95	0.96	0.97	0.98	0.99
5%	100.0	99.9	99.5	98.6	97.3	96.7	96.1	95.8	95.4	95.1	94.8	94.5
10%	100.0	100.0	99.9	99.7	99.2	98.9	98.6	98.4	98.2	98.0	97.8	97.5
15%	100.0	100.0	100.0	99.9	99.7	99.5	99.3	99.2	99.0	98.9	98.7	98.5
20%	100.0	100.0	100.0	100.0	99.8	99.7	99.6	99.5	99.4	99.3	99.1	99.0
25%	100.0	100.0	100.0	100.0	99.9	99.8	99.7	99.7	99.6	99.5	99.4	99.3
30%	100.0	100.0	100.0	100.0	99.9	99.9	99.8	99.8	99.7	99.6	99.6	99.4
35%	100.0	100.0	100.0	100.0	100.0	99.9	99.9	99.8	99.8	99.7	99.7	99.6
40%	100.0	100.0	100.0	100.0	100.0	100.0	99.9	99.9	99.9	99.8	99.7	99.7
45%	100.0	100.0	100.0	100.0	100.0	100.0	99.9	99.9	99.9	99.9	99.8	99.7
50%	100.0	100.0	100.0	100.0	100.0	100.0	100.0	99.9	99.9	99.9	99.9	99.8
55%	100.0	100.0	100.0	100.0	100.0	100.0	100.0	100.0	99.9	99.9	99.9	99.8
60%	100.0	100.0	100.0	100.0	100.0	100.0	100.0	100.0	100.0	99.9	99.9	99.9
65%	100.0	100.0	100.0	100.0	100.0	100.0	100.0	100.0	100.0	100.0	99.9	99.9
70%	100.0	100.0	100.0	100.0	100.0	100.0	100.0	100.0	100.0	100.0	100.0	99.9
75%	100.0	100.0	100.0	100.0	100.0	100.0	100.0	100.0	100.0	100.0	100.0	99.9
80%	100.0	100.0	100.0	100.0	100.0	100.0	100.0	100.0	100.0	100.0	100.0	100.0
85%	100.0	100.0	100.0	100.0	100.0	100.0	100.0	100.0	100.0	100.0	100.0	100.0
90%	100.0	100.0	100.0	100.0	100.0	100.0	100.0	100.0	100.0	100.0	100.0	100.0
95%	100.0	100.0	100.0	100.0	100.0	100.0	100.0	100.0	100.0	100.0	100.0	100.0



**Table 7: Sensitivity (%) versus Positive Predictive Value (PPV) and Area under the ROC curve (Az) for a Cancer Detection Rate = 4 cancer /1000 screens**

PPV	Az Value											
	0.70	0.75	0.80	0.85	0.90	0.92	0.94	0.95	0.96	0.97	0.98	0.99
5%	0.5	4.3	14.9	32.7	55.3	65.0	74.7	79.5	84.2	88.8	93.2	97.2
10%	0.0	0.6	4.2	15.0	35.4	46.3	58.5	65.1	71.9	79.0	86.3	93.7
15%	0.0	0.1	1.6	8.3	25.1	35.5	48.2	55.4	63.2	71.7	80.8	90.7
20%	0.0	0.0	0.7	5.0	18.7	28.2	40.7	48.1	56.4	65.7	76.1	87.8
25%	0.0	0.0	0.4	3.2	14.3	22.9	34.8	42.2	50.7	60.5	71.9	85.2
30%	0.0	0.0	0.2	2.1	11.2	18.8	30.1	37.3	45.9	55.9	68.0	82.6
35%	0.0	0.0	0.1	1.4	8.7	15.6	26.0	33.1	41.5	51.8	64.4	80.1
40%	0.0	0.0	0.1	0.9	6.9	12.9	22.6	29.3	37.7	48.0	61.0	77.7
45%	0.0	0.0	0.0	0.6	5.4	10.7	19.6	26.0	34.1	44.4	57.6	75.2
50%	0.0	0.0	0.0	0.4	4.2	8.8	16.9	22.9	30.7	40.9	54.3	72.7
55%	0.0	0.0	0.0	0.3	3.3	7.2	14.5	20.1	27.6	37.5	51.0	70.1
60%	0.0	0.0	0.0	0.2	2.5	5.8	12.3	17.5	24.6	34.2	47.7	67.3
65%	0.0	0.0	0.0	0.1	1.8	4.6	10.3	15.0	21.6	30.9	44.3	64.4
70%	0.0	0.0	0.0	0.1	1.3	3.5	8.4	12.6	18.7	27.6	40.7	61.2
75%	0.0	0.0	0.0	0.0	0.9	2.6	6.6	10.3	15.8	24.1	36.9	57.7
80%	0.0	0.0	0.0	0.0	0.6	1.8	5.0	8.1	13.0	20.6	32.7	53.6
85%	0.0	0.0	0.0	0.0	0.3	1.1	3.5	6.0	10.0	16.7	28.0	48.7
90%	0.0	0.0	0.0	0.0	0.1	0.6	2.1	3.8	6.9	12.4	22.4	42.3
95%	0.0	0.0	0.0	0.0	0.0	0.2	0.8	1.7	3.6	7.2	14.9	32.5

**Table 8: Specificity (%) versus Positive Predictive Value (PPV) and Area under the ROC curve (Az) for a Cancer Detection Rate = 4 cancer /1000 screens**

PPV	Az Value											
	0.70	0.75	0.80	0.85	0.90	0.92	0.94	0.95	0.96	0.97	0.98	0.99
5%	100.0	99.7	98.9	97.5	95.8	95.0	94.3	93.9	93.6	93.2	92.9	92.6
10%	100.0	100.0	99.8	99.5	98.7	98.3	97.9	97.7	97.4	97.1	96.9	96.6
15%	100.0	100.0	100.0	99.8	99.4	99.2	98.9	98.7	98.6	98.4	98.2	97.9
20%	100.0	100.0	100.0	99.9	99.7	99.5	99.3	99.2	99.1	98.9	98.8	98.6
25%	100.0	100.0	100.0	100.0	99.8	99.7	99.6	99.5	99.4	99.3	99.1	99.0
30%	100.0	100.0	100.0	100.0	99.9	99.8	99.7	99.7	99.6	99.5	99.4	99.2
35%	100.0	100.0	100.0	100.0	99.9	99.9	99.8	99.8	99.7	99.6	99.5	99.4
40%	100.0	100.0	100.0	100.0	100.0	99.9	99.9	99.8	99.8	99.7	99.6	99.5
45%	100.0	100.0	100.0	100.0	100.0	99.9	99.9	99.9	99.8	99.8	99.7	99.6
50%	100.0	100.0	100.0	100.0	100.0	100.0	99.9	99.9	99.9	99.8	99.8	99.7
55%	100.0	100.0	100.0	100.0	100.0	100.0	100.0	99.9	99.9	99.9	99.8	99.8
60%	100.0	100.0	100.0	100.0	100.0	100.0	100.0	100.0	99.9	99.9	99.9	99.8
65%	100.0	100.0	100.0	100.0	100.0	100.0	100.0	100.0	100.0	99.9	99.9	99.9
70%	100.0	100.0	100.0	100.0	100.0	100.0	100.0	100.0	100.0	100.0	99.9	99.9
75%	100.0	100.0	100.0	100.0	100.0	100.0	100.0	100.0	100.0	100.0	100.0	99.9
80%	100.0	100.0	100.0	100.0	100.0	100.0	100.0	100.0	100.0	100.0	100.0	99.9
85%	100.0	100.0	100.0	100.0	100.0	100.0	100.0	100.0	100.0	100.0	100.0	100.0
90%	100.0	100.0	100.0	100.0	100.0	100.0	100.0	100.0	100.0	100.0	100.0	100.0
95%	100.0	100.0	100.0	100.0	100.0	100.0	100.0	100.0	100.0	100.0	100.0	100.0

**Table 9: Sensitivity (%) versus Positive Predictive Value (PPV) and Area under the ROC curve (Az) for a Cancer Detection Rate = 5 cancer /1000 screens**

	Az Value											
PPV	0.70	0.75	0.80	0.85	0.90	0.92	0.94	0.95	0.96	0.97	0.98	0.99
5%	1.1	7.1	20.3	39.5	61.5	70.4	79.1	83.3	87.3	91.1	94.8	97.9
10%	0.0	1.1	6.4	19.4	41.1	51.8	63.5	69.6	75.9	82.3	88.7	95.0
15%	0.0	0.3	2.6	11.2	29.9	40.6	53.2	60.1	67.5	75.3	83.6	92.3
20%	0.0	0.1	1.2	7.0	22.7	32.8	45.5	52.8	60.8	69.6	79.2	89.7
25%	0.0	0.0	0.6	4.6	17.7	27.0	39.3	46.8	55.1	64.5	75.2	87.3
30%	0.0	0.0	0.3	3.1	14.0	22.5	34.3	41.7	50.2	60.1	71.5	84.9
35%	0.0	0.0	0.2	2.1	11.1	18.8	30.0	37.2	45.8	55.9	68.0	82.6
40%	0.0	0.0	0.1	1.4	8.9	15.7	26.2	33.3	41.8	52.0	64.6	80.3
45%	0.0	0.0	0.1	1.0	7.0	13.1	22.9	29.7	38.0	48.3	61.3	77.9
50%	0.0	0.0	0.0	0.7	5.6	10.9	19.9	26.4	34.5	44.8	58.0	75.5
55%	0.0	0.0	0.0	0.4	4.4	9.0	17.2	23.3	31.1	41.3	54.7	73.0
60%	0.0	0.0	0.0	0.3	3.4	7.3	14.7	20.4	27.9	37.8	51.4	70.3
65%	0.0	0.0	0.0	0.2	2.5	5.8	12.4	17.6	24.7	34.4	47.9	67.5
70%	0.0	0.0	0.0	0.1	1.8	4.5	10.2	14.9	21.5	30.9	44.2	64.4
75%	0.0	0.0	0.0	0.1	1.3	3.4	8.2	12.3	18.4	27.2	40.3	60.9
80%	0.0	0.0	0.0	0.0	0.8	2.4	6.3	9.8	15.2	23.3	36.0	56.8
85%	0.0	0.0	0.0	0.0	0.5	1.5	4.4	7.3	11.8	19.1	31.0	51.8
90%	0.0	0.0	0.0	0.0	0.2	0.8	2.7	4.8	8.3	14.3	25.0	45.4
95%	0.0	0.0	0.0	0.0	0.1	0.3	1.1	2.2	4.4	8.5	16.9	35.4

**Table 10: Specificity (%) versus Positive Predictive Value (PPV) and Area under the ROC curve (Az) for a Cancer Detection Rate = 5 cancer /1000 screens**

	Az Value											
PPV	0.70	0.75	0.80	0.85	0.90	0.92	0.94	0.95	0.96	0.97	0.98	0.99
5%	99.9	99.3	98.1	96.2	94.1	93.3	92.5	92.1	91.7	91.3	91.0	90.7
10%	100.0	100.0	99.7	99.1	98.1	97.7	97.1	96.9	96.6	96.3	96.0	95.7
15%	100.0	100.0	99.9	99.7	99.2	98.8	98.5	98.3	98.1	97.9	97.6	97.4
20%	100.0	100.0	100.0	99.9	99.5	99.3	99.1	98.9	98.8	98.6	98.4	98.2
25%	100.0	100.0	100.0	99.9	99.7	99.6	99.4	99.3	99.2	99.0	98.9	98.7
30%	100.0	100.0	100.0	100.0	99.8	99.7	99.6	99.5	99.4	99.3	99.2	99.0
35%	100.0	100.0	100.0	100.0	99.9	99.8	99.7	99.7	99.6	99.5	99.4	99.2
40%	100.0	100.0	100.0	100.0	99.9	99.9	99.8	99.7	99.7	99.6	99.5	99.4
45%	100.0	100.0	100.0	100.0	100.0	99.9	99.9	99.8	99.8	99.7	99.6	99.5
50%	100.0	100.0	100.0	100.0	100.0	99.9	99.9	99.9	99.8	99.8	99.7	99.6
55%	100.0	100.0	100.0	100.0	100.0	100.0	99.9	99.9	99.9	99.8	99.8	99.7
60%	100.0	100.0	100.0	100.0	100.0	100.0	100.0	99.9	99.9	99.9	99.8	99.8
65%	100.0	100.0	100.0	100.0	100.0	100.0	100.0	100.0	99.9	99.9	99.9	99.8
70%	100.0	100.0	100.0	100.0	100.0	100.0	100.0	100.0	100.0	99.9	99.9	99.9
75%	100.0	100.0	100.0	100.0	100.0	100.0	100.0	100.0	100.0	100.0	99.9	99.9
80%	100.0	100.0	100.0	100.0	100.0	100.0	100.0	100.0	100.0	100.0	100.0	99.9
85%	100.0	100.0	100.0	100.0	100.0	100.0	100.0	100.0	100.0	100.0	100.0	100.0
90%	100.0	100.0	100.0	100.0	100.0	100.0	100.0	100.0	100.0	100.0	100.0	100.0
95%	100.0	100.0	100.0	100.0	100.0	100.0	100.0	100.0	100.0	100.0	100.0	100.0

**Table 11: Sensitivity (%) versus Positive Predictive Value (PPV) and Area under the ROC curve (Az) for a Cancer Detection Rate = 6 cancer /1000 screens**

PPV	Az Value											
	0.70	0.75	0.80	0.85	0.90	0.92	0.94	0.95	0.96	0.97	0.98	0.99
5%	2.2	10.4	25.7	45.6	66.6	74.7	82.4	86.1	89.6	92.8	95.8	98.4
10%	0.1	1.8	8.7	23.6	45.9	56.4	67.6	73.2	79.0	84.7	90.4	95.9
15%	0.0	0.5	3.8	14.1	34.1	44.9	57.2	63.9	70.9	78.2	85.7	93.4
20%	0.0	0.1	1.9	9.0	26.3	36.8	49.5	56.6	64.3	72.6	81.6	91.1
25%	0.0	0.1	1.0	6.0	20.8	30.6	43.2	50.5	58.7	67.7	77.8	88.8
30%	0.0	0.0	0.5	4.1	16.6	25.7	37.9	45.4	53.8	63.3	74.2	86.6
35%	0.0	0.0	0.3	2.9	13.3	21.7	33.4	40.8	49.3	59.2	70.8	84.5
40%	0.0	0.0	0.2	2.0	10.8	18.3	29.4	36.7	45.2	55.3	67.5	82.3
45%	0.0	0.0	0.1	1.4	8.7	15.4	25.9	32.9	41.4	51.6	64.2	80.0
50%	0.0	0.0	0.1	1.0	6.9	12.9	22.6	29.4	37.7	48.0	61.0	77.7
55%	0.0	0.0	0.0	0.6	5.5	10.7	19.7	26.1	34.2	44.5	57.7	75.3
60%	0.0	0.0	0.0	0.4	4.2	8.8	16.9	23.0	30.8	40.9	54.4	72.7
65%	0.0	0.0	0.0	0.3	3.2	7.1	14.3	20.0	27.4	37.4	50.9	70.0
70%	0.0	0.0	0.0	0.2	2.4	5.6	11.9	17.0	24.0	33.7	47.2	66.9
75%	0.0	0.0	0.0	0.1	1.7	4.2	9.6	14.2	20.6	29.8	43.1	63.4
80%	0.0	0.0	0.0	0.0	1.1	3.0	7.4	11.4	17.2	25.7	38.7	59.4
85%	0.0	0.0	0.0	0.0	0.6	1.9	5.3	8.5	13.5	21.2	33.6	54.4
90%	0.0	0.0	0.0	0.0	0.3	1.0	3.3	5.7	9.6	16.1	27.3	47.9
95%	0.0	0.0	0.0	0.0	0.1	0.3	1.4	2.7	5.2	9.8	18.7	37.7

**Table 12: Specificity (%) versus Positive Predictive Value (PPV) and Area under the ROC curve (Az) for a Cancer Detection Rate = 6 cancer /1000 screens**

PPV	Az Value											
	0.70	0.75	0.80	0.85	0.90	0.92	0.94	0.95	0.96	0.97	0.98	0.99
5%	99.8	98.8	97.1	94.8	92.4	91.5	90.6	90.1	89.7	89.4	89.0	88.7
10%	100.0	99.9	99.5	98.7	97.5	96.9	96.3	96.0	95.7	95.4	95.1	94.8
15%	100.0	100.0	99.9	99.5	98.8	98.5	98.0	97.8	97.6	97.3	97.1	96.8
20%	100.0	100.0	100.0	99.8	99.4	99.1	98.8	98.6	98.5	98.2	98.0	97.8
25%	100.0	100.0	100.0	99.9	99.6	99.4	99.2	99.1	98.9	98.8	98.6	98.4
30%	100.0	100.0	100.0	99.9	99.8	99.6	99.5	99.4	99.2	99.1	99.0	98.8
35%	100.0	100.0	100.0	100.0	99.9	99.8	99.6	99.5	99.4	99.3	99.2	99.1
40%	100.0	100.0	100.0	100.0	99.9	99.8	99.7	99.7	99.6	99.5	99.4	99.3
45%	100.0	100.0	100.0	100.0	99.9	99.9	99.8	99.8	99.7	99.6	99.5	99.4
50%	100.0	100.0	100.0	100.0	100.0	99.9	99.9	99.8	99.8	99.7	99.6	99.5
55%	100.0	100.0	100.0	100.0	100.0	99.9	99.9	99.9	99.8	99.8	99.7	99.6
60%	100.0	100.0	100.0	100.0	100.0	100.0	99.9	99.9	99.9	99.8	99.8	99.7
65%	100.0	100.0	100.0	100.0	100.0	100.0	100.0	99.9	99.9	99.9	99.8	99.8
70%	100.0	100.0	100.0	100.0	100.0	100.0	100.0	100.0	99.9	99.9	99.9	99.8
75%	100.0	100.0	100.0	100.0	100.0	100.0	100.0	100.0	100.0	99.9	99.9	99.9
80%	100.0	100.0	100.0	100.0	100.0	100.0	100.0	100.0	100.0	100.0	99.9	99.9
85%	100.0	100.0	100.0	100.0	100.0	100.0	100.0	100.0	100.0	100.0	100.0	99.9
90%	100.0	100.0	100.0	100.0	100.0	100.0	100.0	100.0	100.0	100.0	100.0	100.0
95%	100.0	100.0	100.0	100.0	100.0	100.0	100.0	100.0	100.0	100.0	100.0	100.0

**Table 13: Sensitivity (%) versus Positive Predictive Value (PPV) and Area under the ROC curve (Az) for a  
Cancer Detection Rate = 8 cancer /1000 screens**

PPV	Az Value											
	0.70	0.75	0.80	0.85	0.90	0.92	0.94	0.95	0.96	0.97	0.98	0.99
5%	5.3	17.8	35.9	55.6	74.3	81.0	87.2	90.0	92.7	95.1	97.2	99.0
10%	0.4	3.8	13.8	31.2	53.9	63.7	73.7	78.6	83.5	88.3	92.8	97.1
15%	0.1	1.1	6.5	19.6	41.4	52.1	63.8	69.9	76.1	82.4	88.8	95.0
20%	0.0	0.4	3.4	13.1	32.7	43.5	55.9	62.7	69.8	77.3	85.1	93.0
25%	0.0	0.2	1.9	9.0	26.4	36.8	49.5	56.7	64.4	72.7	81.6	91.1
30%	0.0	0.1	1.1	6.4	21.5	31.4	44.0	51.4	59.5	68.4	78.3	89.1
35%	0.0	0.0	0.6	4.5	17.6	26.9	39.2	46.6	55.0	64.4	75.1	87.2
40%	0.0	0.0	0.4	3.2	14.4	23.0	34.9	42.3	50.8	60.6	72.0	85.2
45%	0.0	0.0	0.2	2.3	11.7	19.6	31.0	38.3	46.8	56.9	68.8	83.1
50%	0.0	0.0	0.1	1.6	9.5	16.7	27.4	34.5	43.0	53.2	65.7	81.0
55%	0.0	0.0	0.1	1.1	7.6	14.0	24.0	30.9	39.3	49.6	62.4	78.7
60%	0.0	0.0	0.0	0.8	6.0	11.6	20.9	27.4	35.6	46.0	59.1	76.3
65%	0.0	0.0	0.0	0.5	4.7	9.5	17.9	24.1	32.0	42.2	55.6	73.7
70%	0.0	0.0	0.0	0.3	3.5	7.6	15.1	20.8	28.4	38.4	51.9	70.7
75%	0.0	0.0	0.0	0.2	2.5	5.8	12.3	17.5	24.6	34.3	47.8	67.4
80%	0.0	0.0	0.0	0.1	1.7	4.2	9.7	14.2	20.7	29.9	43.2	63.5
85%	0.0	0.0	0.0	0.0	1.0	2.8	7.0	10.9	16.5	24.9	37.8	58.6
90%	0.0	0.0	0.0	0.0	0.5	1.5	4.5	7.4	11.9	19.2	31.1	52.0
95%	0.0	0.0	0.0	0.0	0.1	0.5	2.0	3.7	6.6	11.9	21.8	41.6

**Table 14: Specificity (%) versus Positive Predictive Value (PPV) and Area under the ROC curve (Az) for a  
Cancer Detection Rate = 8 cancer /1000 screens**

PPV	Az Value											
	0.70	0.75	0.80	0.85	0.90	0.92	0.94	0.95	0.96	0.97	0.98	0.99
5%	99.2	97.3	94.5	91.5	88.6	87.6	86.7	86.2	85.8	85.4	85.1	84.9
10%	100.0	99.7	99.0	97.7	96.1	95.4	94.7	94.3	94.0	93.6	93.3	93.0
15%	100.0	99.9	99.7	99.1	98.1	97.6	97.1	96.8	96.5	96.2	95.9	95.7
20%	100.0	100.0	99.9	99.6	98.9	98.6	98.2	98.0	97.7	97.5	97.3	97.0
25%	100.0	100.0	100.0	99.8	99.4	99.1	98.8	98.6	98.4	98.2	98.0	97.8
30%	100.0	100.0	100.0	99.9	99.6	99.4	99.2	99.0	98.9	98.7	98.5	98.3
35%	100.0	100.0	100.0	99.9	99.7	99.6	99.4	99.3	99.2	99.0	98.9	98.7
40%	100.0	100.0	100.0	100.0	99.8	99.7	99.6	99.5	99.4	99.3	99.1	99.0
45%	100.0	100.0	100.0	100.0	99.9	99.8	99.7	99.6	99.5	99.4	99.3	99.2
50%	100.0	100.0	100.0	100.0	99.9	99.9	99.8	99.7	99.7	99.6	99.5	99.3
55%	100.0	100.0	100.0	100.0	99.9	99.9	99.8	99.8	99.7	99.7	99.6	99.5
60%	100.0	100.0	100.0	100.0	100.0	99.9	99.9	99.9	99.8	99.8	99.7	99.6
65%	100.0	100.0	100.0	100.0	100.0	100.0	99.9	99.9	99.9	99.8	99.8	99.7
70%	100.0	100.0	100.0	100.0	100.0	100.0	99.9	99.9	99.9	99.9	99.8	99.8
75%	100.0	100.0	100.0	100.0	100.0	100.0	100.0	100.0	99.9	99.9	99.9	99.8
80%	100.0	100.0	100.0	100.0	100.0	100.0	100.0	100.0	100.0	99.9	99.9	99.9
85%	100.0	100.0	100.0	100.0	100.0	100.0	100.0	100.0	100.0	100.0	99.9	99.9
90%	100.0	100.0	100.0	100.0	100.0	100.0	100.0	100.0	100.0	100.0	100.0	100.0
95%	100.0	100.0	100.0	100.0	100.0	100.0	100.0	100.0	100.0	100.0	100.0	100.0

**Table 15: Sensitivity (%) versus Positive Predictive Value (PPV) and Area under the ROC curve (Az) for a Cancer Detection Rate = 10 cancer /1000 screens**

PPV	Az Value											
	0.70	0.75	0.80	0.85	0.90	0.92	0.94	0.95	0.96	0.97	0.98	0.99
5%	9.9	25.8	44.9	63.5	79.8	85.4	90.4	92.6	94.7	96.5	98.1	99.4
10%	1.0	6.4	19.1	38.0	60.2	69.2	78.2	82.5	86.7	90.7	94.4	97.8
15%	0.1	2.1	9.5	24.9	47.3	57.8	68.7	74.2	79.8	85.4	90.9	96.1
20%	0.0	0.8	5.2	17.1	38.2	49.0	61.0	67.4	73.9	80.7	87.5	94.4
25%	0.0	0.3	3.0	12.1	31.3	42.1	54.5	61.4	68.7	76.3	84.3	92.6
30%	0.0	0.1	1.8	8.7	25.8	36.3	48.9	56.1	63.9	72.3	81.3	90.9
35%	0.0	0.1	1.1	6.4	21.4	31.4	44.0	51.3	59.4	68.4	78.2	89.1
40%	0.0	0.0	0.6	4.6	17.7	27.1	39.4	46.9	55.2	64.6	75.2	87.3
45%	0.0	0.0	0.4	3.3	14.7	23.4	35.3	42.7	51.2	61.0	72.2	85.4
50%	0.0	0.0	0.2	2.4	12.0	20.0	31.4	38.7	47.3	57.3	69.2	83.4
55%	0.0	0.0	0.1	1.7	9.8	17.0	27.8	34.9	43.5	53.7	66.0	81.3
60%	0.0	0.0	0.1	1.2	7.8	14.3	24.4	31.2	39.7	50.0	62.7	79.0
65%	0.0	0.0	0.0	0.8	6.1	11.8	21.1	27.6	35.9	46.2	59.3	76.5
70%	0.0	0.0	0.0	0.5	4.6	9.5	17.9	24.1	32.0	42.2	55.6	73.6
75%	0.0	0.0	0.0	0.3	3.4	7.4	14.8	20.4	27.9	38.0	51.4	70.4
80%	0.0	0.0	0.0	0.2	2.3	5.4	11.7	16.8	23.7	33.3	46.8	66.6
85%	0.0	0.0	0.0	0.1	1.4	3.7	8.6	13.0	19.1	28.1	41.3	61.8
90%	0.0	0.0	0.0	0.0	0.7	2.1	5.6	8.9	14.0	21.9	34.3	55.2
95%	0.0	0.0	0.0	0.0	0.2	0.8	2.6	4.6	8.0	13.9	24.4	44.6

**Table 16: Specificity (%) versus Positive Predictive Value (PPV) and Area under the ROC curve (Az) for a Cancer Detection Rate = 10 cancer /1000 screens**

PPV	Az Value											
	0.70	0.75	0.80	0.85	0.90	0.92	0.94	0.95	0.96	0.97	0.98	0.99
5%	98.1	95.0	91.4	87.8	84.7	83.6	82.7	82.2	81.9	81.5	81.2	81.0
10%	99.9	99.4	98.3	96.5	94.5	93.7	92.9	92.5	92.1	91.8	91.4	91.1
15%	100.0	99.9	99.5	98.6	97.3	96.7	96.1	95.8	95.4	95.1	94.8	94.5
20%	100.0	100.0	99.8	99.3	98.5	98.0	97.5	97.3	97.0	96.7	96.5	96.2
25%	100.0	100.0	99.9	99.6	99.1	98.7	98.3	98.1	97.9	97.7	97.4	97.2
30%	100.0	100.0	100.0	99.8	99.4	99.1	98.8	98.7	98.5	98.3	98.1	97.9
35%	100.0	100.0	100.0	99.9	99.6	99.4	99.2	99.0	98.9	98.7	98.5	98.3
40%	100.0	100.0	100.0	99.9	99.7	99.6	99.4	99.3	99.2	99.0	98.9	98.7
45%	100.0	100.0	100.0	100.0	99.8	99.7	99.6	99.5	99.4	99.2	99.1	98.9
50%	100.0	100.0	100.0	100.0	99.9	99.8	99.7	99.6	99.5	99.4	99.3	99.2
55%	100.0	100.0	100.0	100.0	99.9	99.9	99.8	99.7	99.6	99.6	99.5	99.3
60%	100.0	100.0	100.0	100.0	99.9	99.9	99.8	99.8	99.7	99.7	99.6	99.5
65%	100.0	100.0	100.0	100.0	100.0	99.9	99.9	99.9	99.8	99.7	99.7	99.6
70%	100.0	100.0	100.0	100.0	100.0	100.0	99.9	99.9	99.9	99.8	99.8	99.7
75%	100.0	100.0	100.0	100.0	100.0	100.0	100.0	99.9	99.9	99.9	99.8	99.8
80%	100.0	100.0	100.0	100.0	100.0	100.0	100.0	100.0	99.9	99.9	99.9	99.8
85%	100.0	100.0	100.0	100.0	100.0	100.0	100.0	100.0	100.0	100.0	99.9	99.9
90%	100.0	100.0	100.0	100.0	100.0	100.0	100.0	100.0	100.0	100.0	100.0	99.9
95%	100.0	100.0	100.0	100.0	100.0	100.0	100.0	100.0	100.0	100.0	100.0	100.0

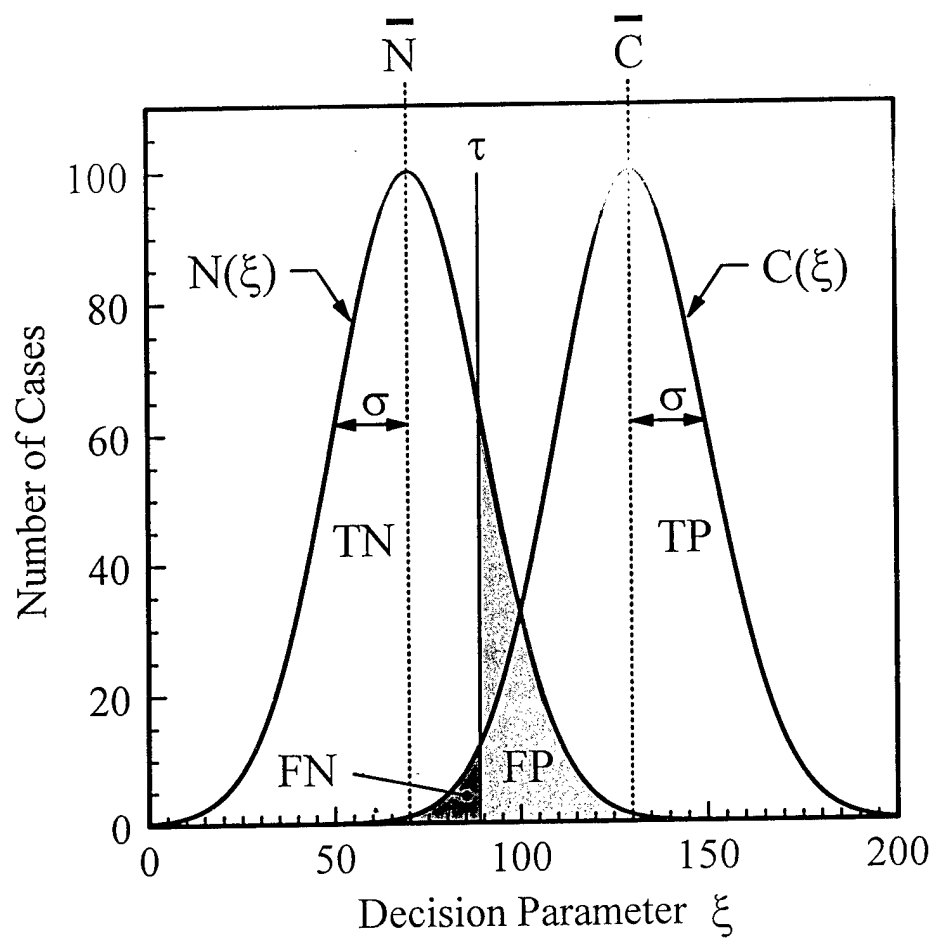


Figure 1

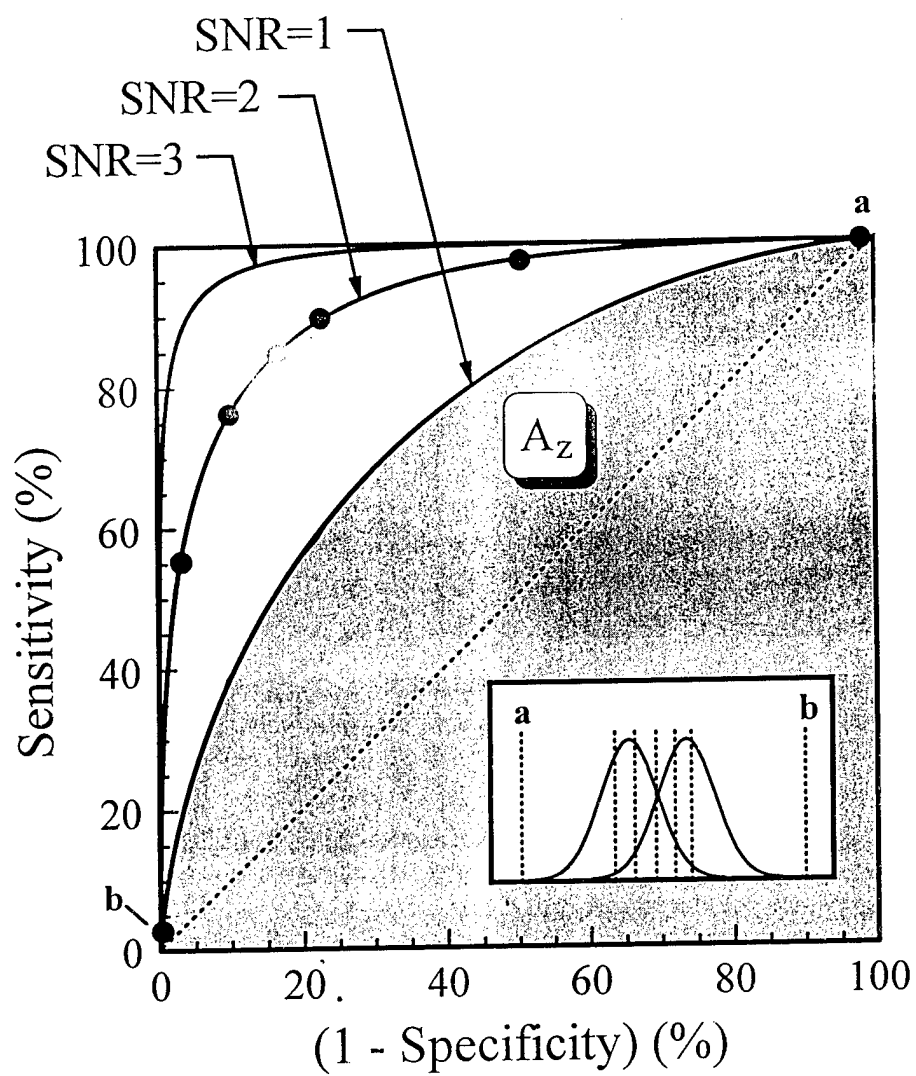


Figure 2

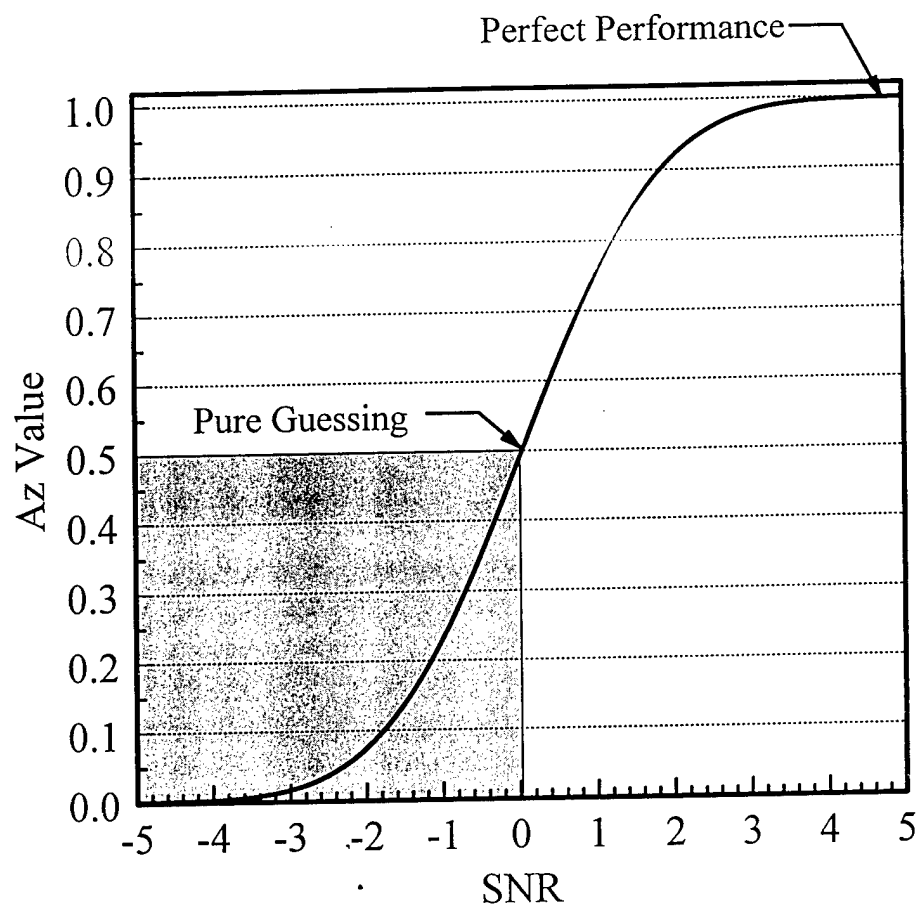


Figure 3



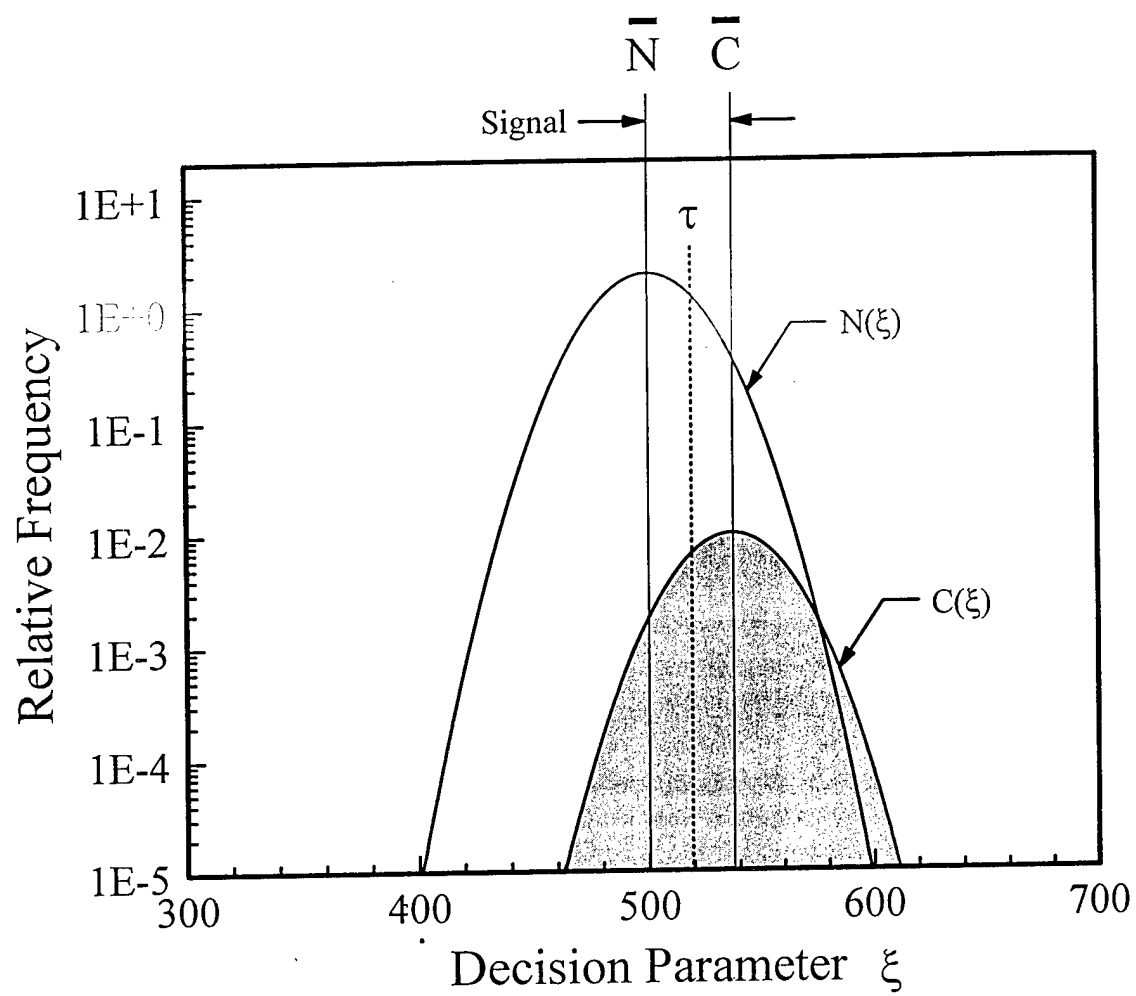


Figure 4

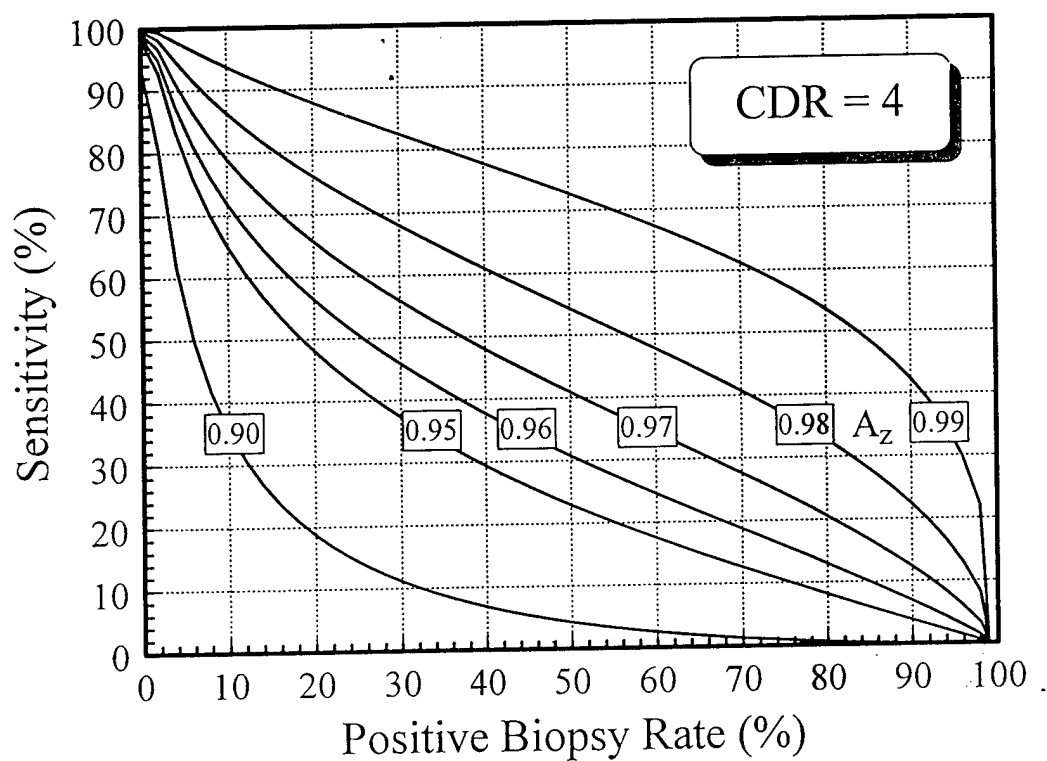
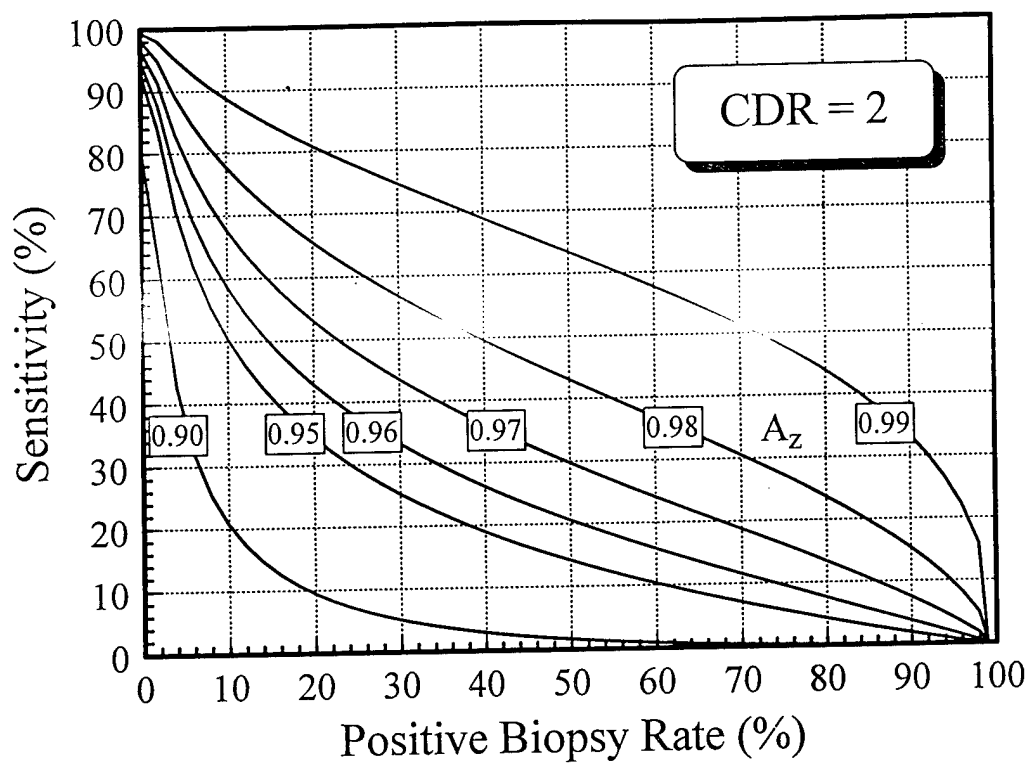


Figure 5

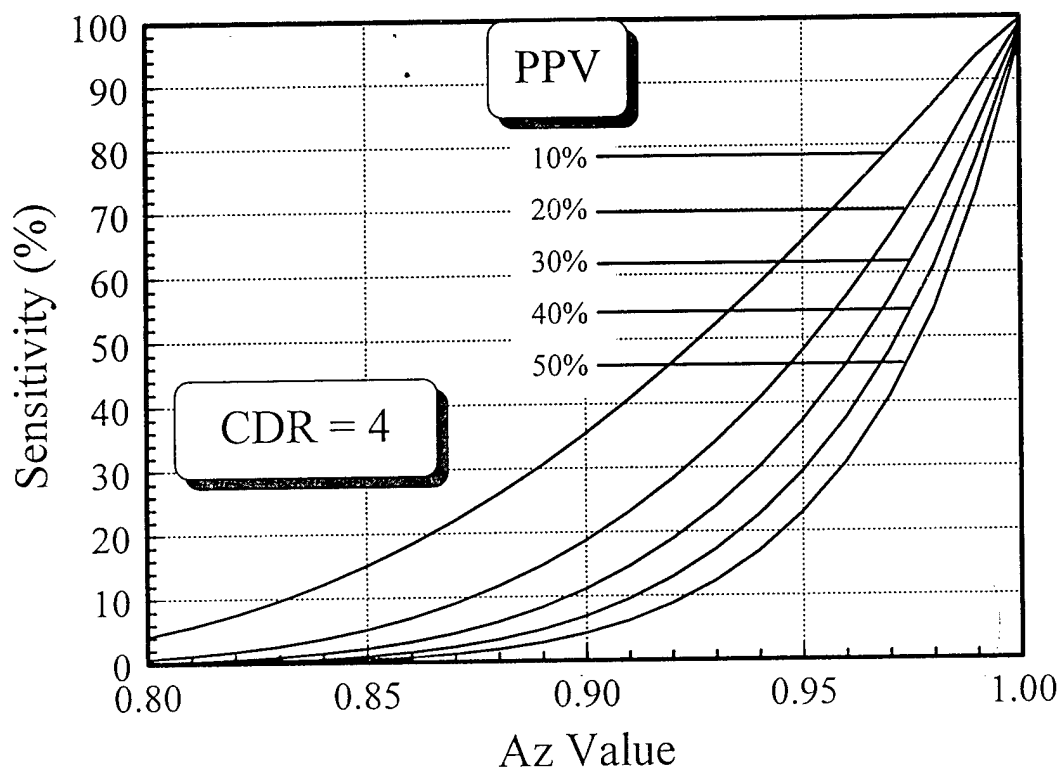
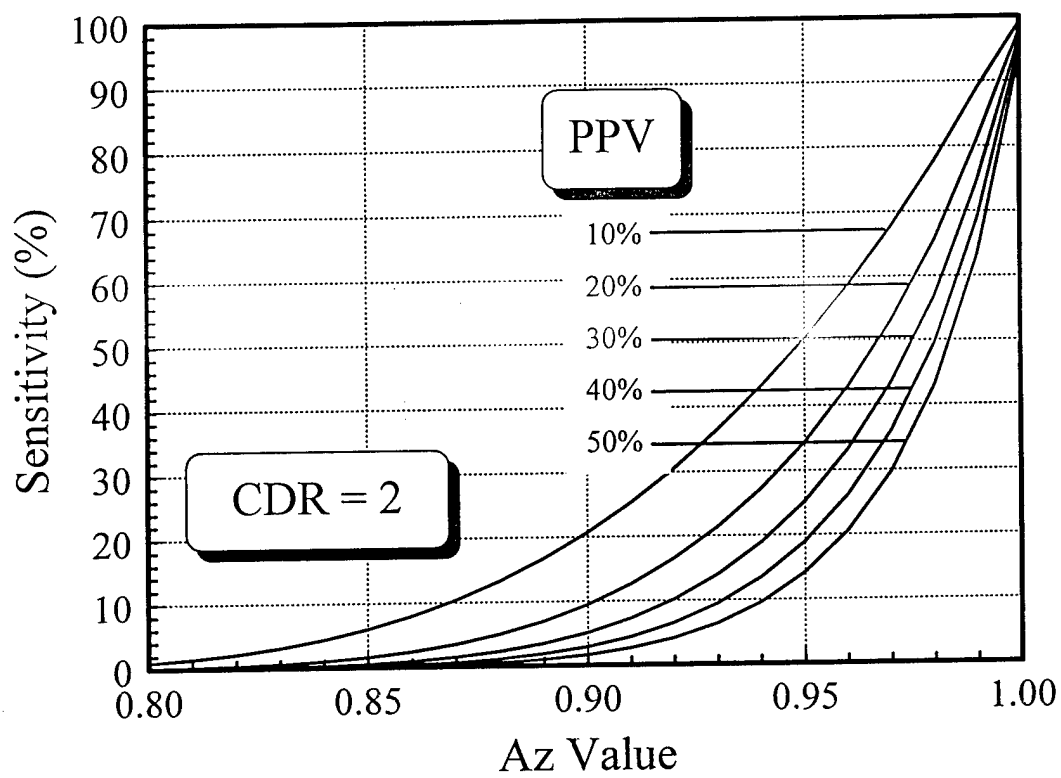


Figure 6

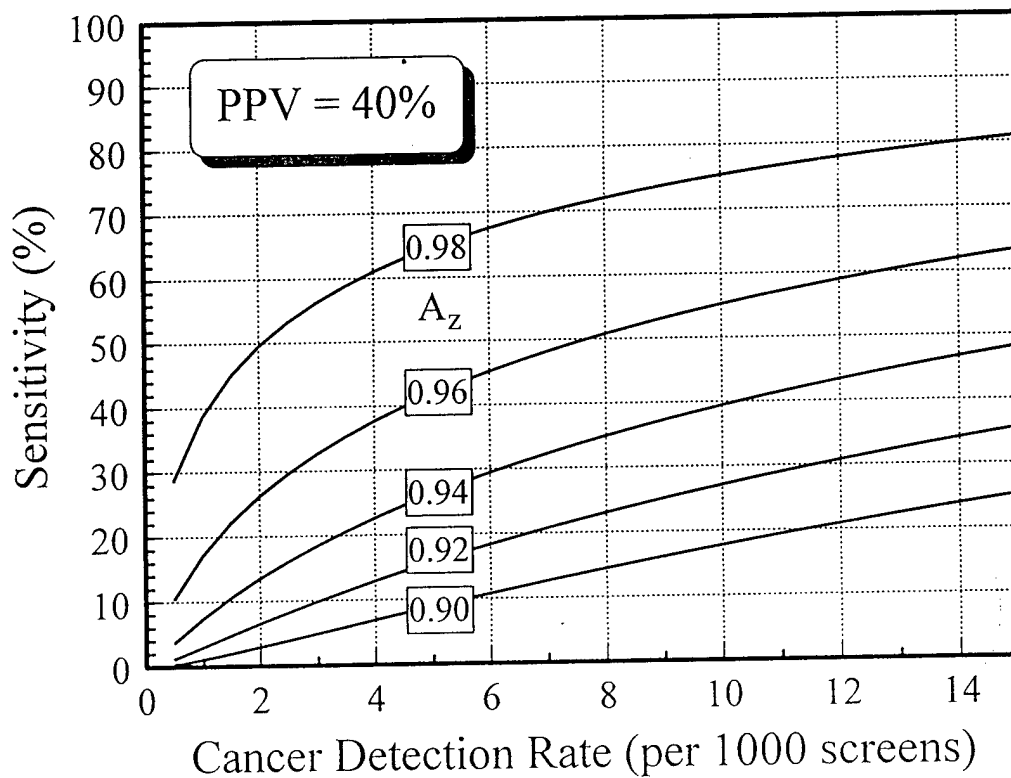
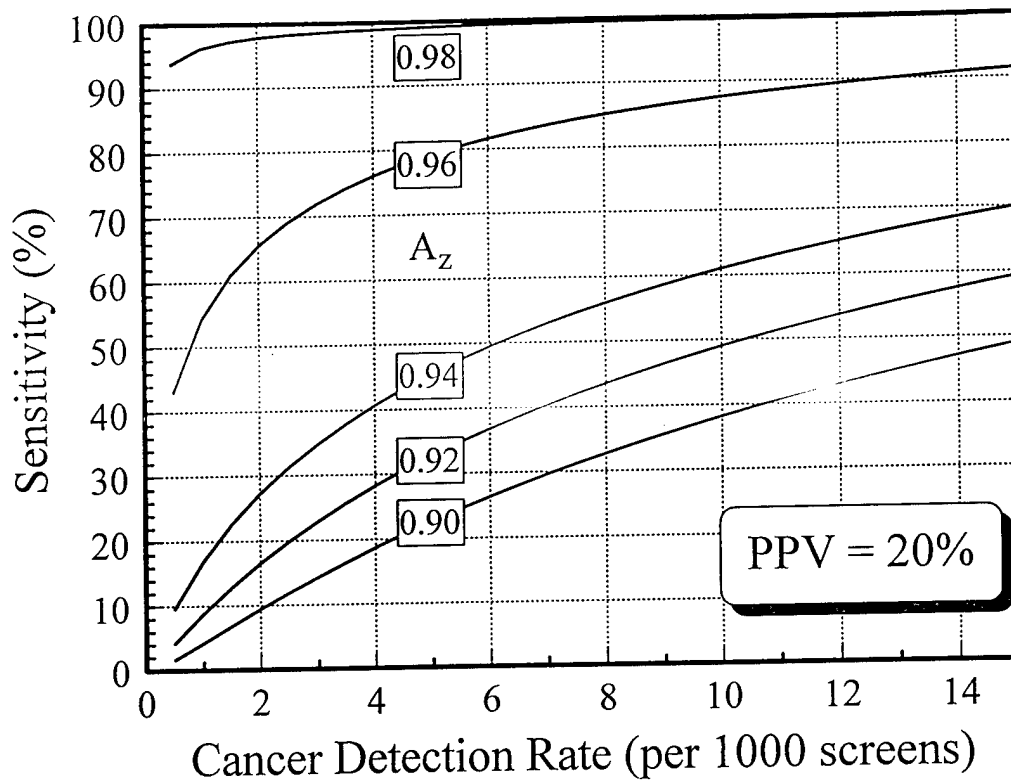


Figure 7

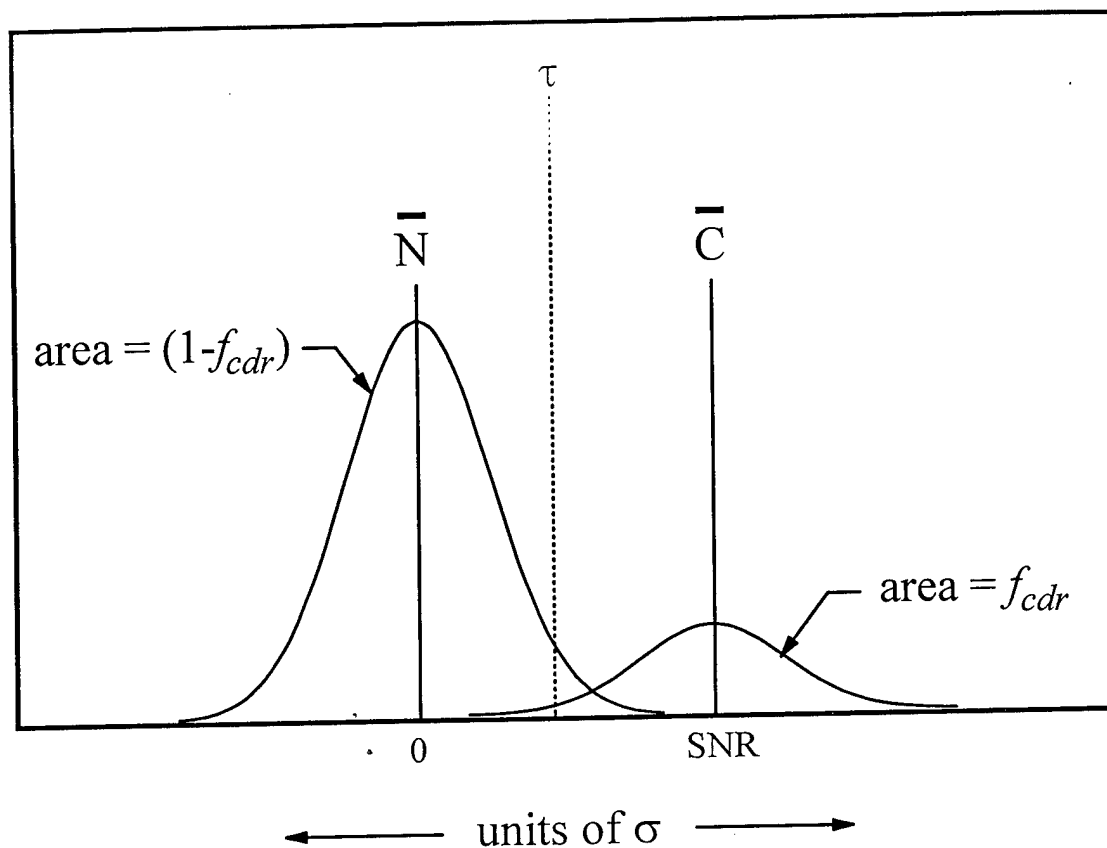


Figure 8

John M. Boone, PhD

### Index terms:

Breast radiography, radiation dose, 00.47, 0.99  
Breast radiography, technology, 00.12  
Breast radiography, utilization, 00.99  
Physics

Radiology 1999; 213:23-37

### Abbreviations:

$D_{gN}$  = normalized glandular dose  
HVL = half-value layer  
 $f(E)$  = fractional energy absorption  
Mo-Mo = molybdenum anode-molybdenum filter  
Mo-Rh = molybdenum anode-rhodium filter  
Rh-Rh = rhodium anode-rhodium filter  
W-Ag = tungsten anode-silver filter  
W-Pd = tungsten anode-palladium filter  
W-Rh = tungsten anode-rhodium filter

<sup>1</sup> From the Department of Radiology, University of California, Davis, Medical Center, 4701 X St., Radiology Research Laboratories, Sacramento, CA 95817. Received August 26, 1998; revision requested October 23; final revision received January 14, 1999; accepted March 26. Supported in part by grants from the United States Army Breast Cancer Research Program (DAMD17-94-J-4424 and DAMD17-98-1-8176), the California Breast Cancer Research Program (0192), and the National Cancer Institute (R21 CA 82077). Address reprint requests to the author (e-mail: jmboone@ucdavis.edu).

© RSNA, 1999

See also the editorial by Kimme-Smith (pp 7-10) in this issue.

### Author contribution:

Guarantor of integrity of entire study, J.M.B.

## Glandular Breast Dose for Monoenergetic and High-Energy X-ray Beams: Monte Carlo Assessment<sup>1</sup>

**PURPOSE:** To extend the utility of normalized glandular dose ( $D_{gN}$ ) calculations to higher x-ray energies (up to 120 keV) and to provide the tools for investigators to calculate  $D_{gN}$  values for arbitrary mammographic and x-ray spectra.

**MATERIALS AND METHODS:** Validated Monte Carlo methods were used to assess  $D_{gN}$  values. One million x-ray photons (1-120 keV, in 1-keV increments) were input to a semicircular breast geometry of thicknesses from 2 to 12 cm and breast compositions from 0% to 100% glandular.  $D_{gN}$  values for monoenergetic (1-120 keV) x-ray beams, polyenergetic (40-120 kV, tungsten anode) x-ray spectra, and polyenergetic mammographic spectra were computed. Skin thicknesses of 4-5 mm were used.

**RESULTS:** The calculated  $D_{gN}$  values were in agreement within approximately 1%-6% with previously published data, depending on breast composition.  $D_{gN}$  tables were constructed for a variety of x-ray tube anode-filter combinations, including molybdenum anode-molybdenum filter, molybdenum anode-rhodium filter, rhodium anode-rhodium filter, tungsten anode-rhodium filter, tungsten anode-palladium filter, and tungsten anode-silver filter.  $D_{gN}$  values also were graphed for monoenergetic beams to 120 keV and for general diagnostic x-ray beams to 120 kV.

**CONCLUSION:** The tables and graphs may be useful for optimizing mammographic procedures. The higher energy data may be useful for investigations of the potential of dual-energy mammography or for calculation of dose in general diagnostic or computed tomographic procedures.

The assessment of radiation dose to the breast during mammography has been of interest to many investigators (1-19). Over the years, the normalized glandular dose ( $D_{gN}$ ) has come to serve as the benchmark parameter, useful for calculating the glandular dose in clinical mammography. The  $D_{gN}$  values are essentially the roentgen-to-rad conversion values, calculated for the "at-risk" glandular component of the breast. Recent efforts to calculate  $D_{gN}$  tables for the mammography community have primarily been focused on clinically relevant spectra (4,5,7) with molybdenum anode-molybdenum filter (Mo-Mo), molybdenum anode-rhodium filter (Mo-Rh), or rhodium anode-rhodium filter (Rh-Rh) combinations in the 20-35-kV range.

In this work,  $D_{gN}$  tables were computed for much thicker breasts than for those in previous reports, with values reported here for breast thicknesses from 2 to 12 cm in 1-cm increments. While the typical compressed breast thickness in the United States is approximately 4.2 cm, there are many women with a compressed breast thickness that ranges to 12 cm or thicker. The tables provided in this article may be useful for these patients.

The motivation to extend  $D_{gN}$  tables to encompass higher energy levels was based on an interest in dual-energy mammography, where the optimal high-energy beam is likely to be very high (>100 keV), well beyond current clinical mammographic x-ray beam energies. In

addition, with the recent introduction of full-field digital mammography systems into the clinical environment, it is likely that slightly higher energy x-ray beams may become useful in some instances. This study was intended to extend the utility of  $D_{gN}$  calculations to higher x-ray energies (up to 120 keV) and to provide the tools for investigators to calculate  $D_{gN}$  values for arbitrary x-ray spectra, including monoenergetic x-ray beams (for example, produced by synchrotron sources [20], free-electron lasers [21], or other exotic x-ray sources). To this end, tables of  $D_{gN}$  values have been provided for the x-ray tube anode-filter combinations of Mo-Mo, Mo-Rh, Rh-Rh, tungsten anode-rhodium filter (W-Rh), tungsten anode-palladium filter (W-Pd), and tungsten anode-silver filter (W-Ag). Graphical data also are provided to demonstrate  $D_{gN}$  values for monoenergetic and polyenergetic x-ray beams.

## MATERIALS AND METHODS

### Details of the Monte Carlo Study

Monte Carlo procedures were used to compute the glandular dose to the breast. Although I have developed independent computer code for Monte Carlo studies (22,23), the TART97 Monte Carlo code was purchased from the Radiation Safety Information Computational Center, Oak Ridge National Laboratory (Oak Ridge, Tenn) for use in this study. The TART97 code was developed primarily at Lawrence Livermore National Laboratory (24) in Livermore, Calif, and is a thoroughly verified and mature Monte Carlo program. A full description of the TART97 Monte Carlo program is available in the literature (24); however, a brief description is appropriate here.

In a Monte Carlo simulation, each of the millions of photons traced in computations undergoes absorption or scattering, depending on the outcome of a random number generator. The probabilities of the multiple scattering calculations are weighted by the probability of that event at each x-ray energy studied. The TART97 Monte Carlo routine uses multiple scattering calculations, follows the history of all photons, and includes the photoelectric, Raleigh, and Compton scatter interaction mechanisms in the energy region reported. All photons were followed until they either left the volume of interest, were completely absorbed, or reached an arbitrarily small energy level (0.10 keV).

Monoenergetic x-ray photons at 1-keV intervals were input into a mathematic phantom in each of the simulation runs. Each photon run made use of 1 million photons at each monoenergetic energy level, and these data were used to construct monoenergetic  $D_{gN}$  tables in a procedure described later in this article. The lowest energy simulated was 1 keV, and the highest was 120 keV. For the polyenergetic spectra reported, weighted sums of the monoenergetic  $D_{gN}$  data were computed. The x-ray spectra used for this study were generated by using mathematic spectral models described previously (25,26). The x-ray attenuation coefficients for the filters also were reported previously (27).

### Geometry and Composition Issues

The geometry simulated in this study is shown in Figure 1. Instead of a D-shaped semicircular breast shape, as others (4,5) have used, a cylindric breast shape was simulated (Fig 1a). The cone-shaped radiation field emitted from the source was collimated to irradiate half of the breast (a semicircle). The semicircular field geometry was particularly simple to simulate with the TART97 code and was efficient to run. The semicircle of breast tissue that was not in the radiation field was intended to simulate the presence of the torso of the patient (the chest wall). For their geometries, Wu et al (4) and Dance (5) assumed a D-shaped breast (no chest wall). The presence of tissue outside of the radiation field may have a minor influence in terms of backscatter, and this is of particular concern in this study due to the much higher x-ray energies studied here. While the nonirradiated semicircle is not the exact geometry of the chest wall, it was thought that the presence of some tissue behind the breast was slightly more representative of the geometry encountered in mammography, rather than no tissue outside of the radiation field.

Various breast compositions were studied, from 0% glandular–100% adipose to 100% glandular–0% adipose, by mass.  $D_{gN}$  values were computed for the proportion of glandular tissue mass to total breast tissue mass. For concise reference henceforward, the breast composition is referred to in terms of the glandular percentage alone. The compositional data from Hammerstein et al (28) were used. X-ray coefficients for compound (multi-elemental) substances such as breast tissue were prorated on the basis of the weight fraction of the element; however,

in substances where the density changed with the composition, the calculation of proportions is a little more complicated, and the techniques described in the following paragraphs were used.

For a tissue containing a weight fraction  $f_g$  of glandular tissue (and, correspondingly, a weight fraction of  $1 - f_g$  for adipose tissue), it can be shown that the glandular volume fraction  $v_g$  is given by

$$v_g = \left[ \frac{(1 - f_g) \rho_g}{f_g \rho_a} + 1 \right]^{-1}, \quad (1)$$

where  $\rho_g$  is the density of 100% glandular tissue ( $\rho_g = 1.04$  g/cm<sup>3</sup>, from Hammerstein et al [28]) and  $\rho_a$  is the density of 100% adipose tissue ( $\rho_a = 0.93$  g/cm<sup>3</sup>). Let the total volume be set to unit volume (1 cm<sup>3</sup>) for simplicity, such that  $v_g + v_a = 1$  cm<sup>3</sup>, and the compound density is

$$\rho_{\text{compound}} = \rho_g v_g + \rho_a v_a. \quad (2)$$

The mass  $m$  of each component in the unit volume is simply  $m_g = \rho_g v_g$  and  $m_a = \rho_a v_a$ , where the "g" subscripts refer to glandular tissue and the "a" subscripts refer to adipose tissue. For completeness, the elemental compositions and densities for a variety of glandular fractions are given in the Appendix. By using the above procedure, the linear attenuation coefficients for 0%, 50%, and 100% glandular tissues were compared with those reported by Hammerstein et al (28). These data are shown in Figure 2.

The breast tissue (glandular and adipose compound) is enclosed in a layer of skin, as illustrated in Figure 1. The skin thickness was varied in this study. For comparison with the results of Dance (5), a skin thickness of 5 mm was used. For comparison with the results of Wu et al (4), a skin thickness of 4 mm was used. For a single geometry and breast composition, the influence of skin thickness from 2 to 6 mm was studied. The density and elemental composition of skin, taken from Hammerstein et al (28), are reported in the Appendix.

### Conversion of Monte Carlo Results to $D_{gN}$ Values

For a given breast composition, photon energy, and geometry, the output produced by the TART97 Monte Carlo package that was of interest in this study was the energy deposited (normalized per input photon) in the breast tissue compartment (Fig 1). The average energy to the breast tissue compartment, per incident x-ray photon to the breast, was normalized by means of the energy of the incident photons (all Monte

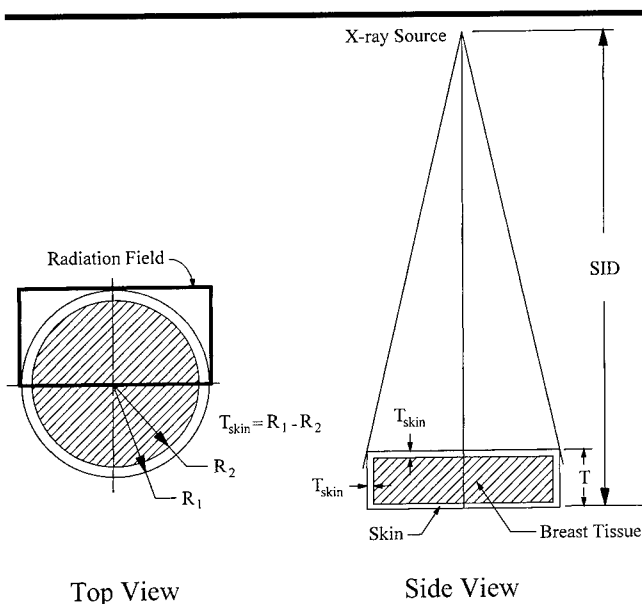


**Figure 1.** Diagram shows the geometry used for the Monte Carlo simulations.  $R_1$  = radius of breast (including skin layer) in millimeters,  $R_2$  = radius of breast (excluding skin layer) in millimeters,  $SID$  = source-to-image distance,  $T$  = breast thickness,  $T_{skin}$  = skin thickness in millimeters.

Carlo runs used monoenergetic spectra), such that the fractional energy absorption,  $f(E)$ , was calculated as follows:

$$f(E) = \frac{\text{energy absorbed per incident photon}}{\text{photon energy}}. \quad (3)$$

The value of  $E$  is expressed in kiloelectron volts, and the x-ray photon spectra  $\Phi(E)$  is normalized to the number of photons corresponding to 1 R (0.258 mC/kg) (for the entire spectrum). This type of normalization is typical (26) for investigators working with x-ray spectra.  $D_{gN}$  values were calculated by using

$$D_{gN} = \sum_{E=E_{min}}^{E_{max}} f(E) \times E(1.6021 \times 10^{-8}) \Phi(E) G \frac{\text{area}}{\text{mass}}, \quad (4)$$

where the value of  $f(E)$  was defined in Equation (3), the constant corrects for various unit conversions,  $G$  is defined later in Equation (6), area is the surface area at the top of the breast (in the entrance plane) exposed to x-rays, and mass is that of the purely glandular portion of the breast tissue. Let  $f_g$  be the glandular fraction, by weight, of the breast tissue. For example,  $f_g = 1.0$  for a 100% glandular breast, and  $f_g = 0.5$  for a 50%

glandular breast. For a semicircular breast tissue compartment of radius  $R_2$  (Fig 1), a breast density  $\rho$ , a compressed breast thickness  $T$ , and a skin layer thickness  $T_{skin}$ , the mass term in Equation 4 is given by

$$\text{mass} = f_g \frac{1}{2} \pi R_2^2 (T - 2T_{skin}) \rho. \quad (5)$$

The  $G$  term in Equation (4) corrects the normalized dose calculation specifically to the glandular component of the breast tissue ( $D_{gN}$ ) in a heterogeneous tissue matrix. Values for breasts with a 0% glandular fraction are computed by extrapolation from  $D_{gN}$  calculations of glandular fractions in the 2%–5% range:

$$G = \frac{f_g \left( \frac{\mu_{en}}{\rho} \right)_g}{\left[ f_g \left( \frac{\mu_{en}}{\rho} \right)_g + (1 - f_g) \left( \frac{\mu_{en}}{\rho} \right)_a \right]}, \quad (6)$$

where the mass energy absorption coefficients ( $\mu_{en}/\rho$ ) are specified with an "a" subscript for adipose tissue and with a "g" subscript for glandular tissue.  $D_{gN}$  and  $G$  were derived from first principles and by consulting previous publications (4,5). Units for  $D_{gN}$  (Eq [4]) were derived as follows:  $D_{gN}$  is expressed in millirad per roentgen,  $f(E)$  has no unit,  $E$  is expressed in kiloelectron

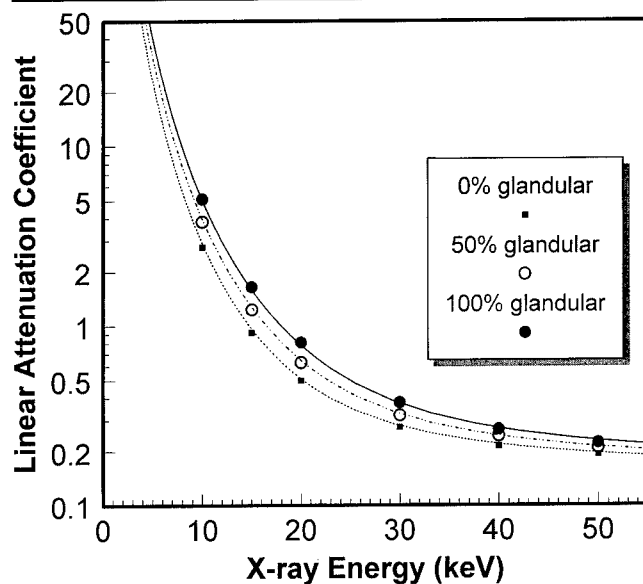


**Figure 2.** Graph shows comparison of the linear attenuation coefficients computed in the present study with those reported by Hammerstein et al (28) for 0%, 50%, and 100% glandular tissue. The data from Hammerstein et al are shown as the symbols, and the coefficients used in the present study are shown as lines. Excellent agreement in terms of attenuation coefficients was observed over the energy range compared.

volts per photon,  $\Phi(E)$  is expressed as photons per square millimeter per roentgen,  $G$  has no unit, area is in square millimeters, and mass is in grams. The constant  $1.6021 \times 10^{-8}$  was derived as follows:

$$\begin{aligned} & (1.6021 \times 10^{-8}) \frac{(\text{mrad g})}{(\text{keV})} \\ &= (1.6021 \times 10^{-9}) \frac{\text{ergs}}{\text{keV}} \\ &\times \frac{1000 \text{ mrad}}{\text{Rad}} \times \frac{\text{g rad}}{100 \text{ ergs}}. \quad (7) \end{aligned}$$

## RESULTS

### Monte Carlo Results for $f(E)$ Values

The Monte Carlo results for 0% and 100% glandular breasts are illustrated in Figure 3. If the breast tissue were not encapsulated in a layer of skin, these curves would be pseudoexponential,  $f(E)$  being unity at very low energy levels and decreasing almost exponentially with increasing energy level. However, x-ray photons of the lowest energy are unable to penetrate the relatively thin skin layer to contribute a fraction of their energy to the breast tissues; rather, the energy is deposited in the skin layer. The value of  $f(E)$  is, therefore, substantially dampened



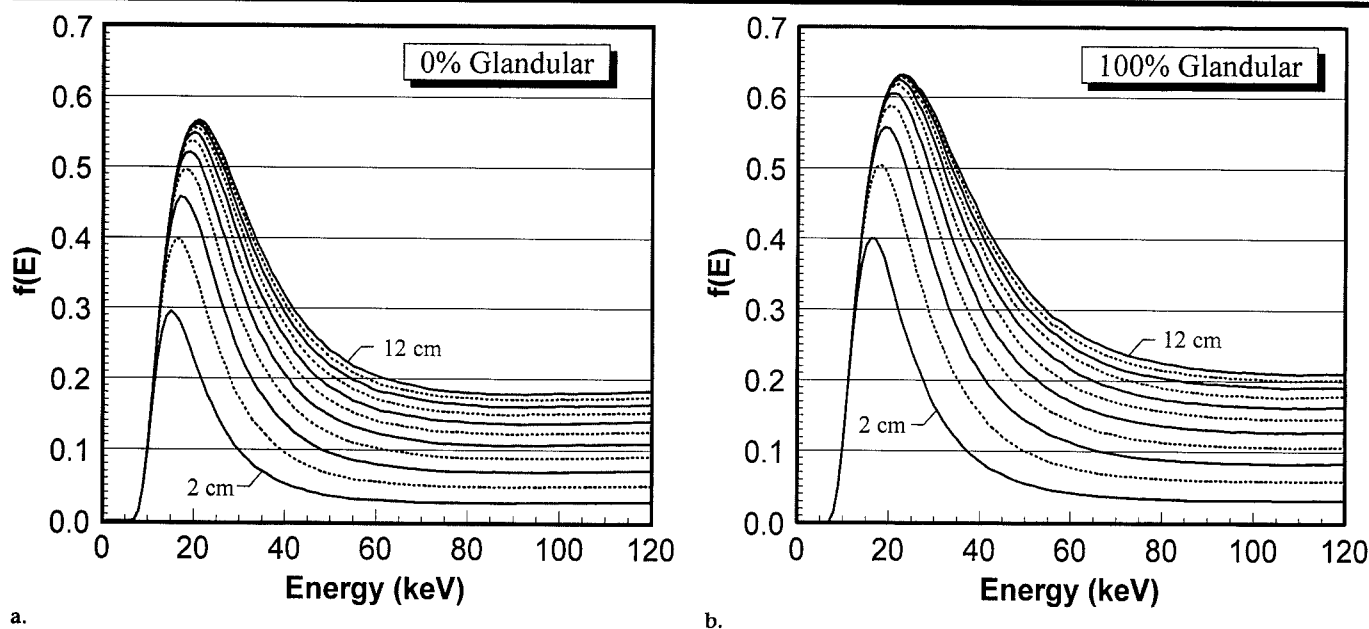


**Figure 3.** Graphs show  $f(E)$  as a function of incident x-ray energy for (a) 0% glandular tissue and (b) 100% glandular tissue. The curves are shown for 11 tissue thicknesses ranging from 2 to 12 cm in 1-cm increments. The bottom curve represents the data for the 2-cm breast thickness, and the top curve represents the data for the 12-cm-thick breast; intermediate curves are not marked for clarity, but are in order from 3 to 11 cm. Dotted lines = curves for odd-numbered tissue thicknesses (3, 5, 7, 9, and 11 cm), solid lines = curves for even-numbered thicknesses (2, 4, 6, 8, 10, and 12 cm).

at the low energy levels because of the effect of skin filtration. As the glandular fraction increases, the  $f(E)$  value of the incident x-rays increases slightly, as would be expected due to the changing composition and increasing density.

It is suspected that subject contrast will be near the maximum when imaging at the kiloelectron voltage corresponding to the peak  $f(E)$  value for each breast thickness and composition. If one plots the data illustrated in Figure 3 differently, one can see the nonlinear effects of breast thickness on  $f(E)$  (Fig 4). In Figure 4, the absorption of 10-keV photons was constant across breast thicknesses, which suggested that the absorption dynamics of these low-energy photons occurred in the first 2 cm of tissue. At higher incident photon energy levels, the  $f(E)$  value increased with increasing breast thickness, as would be expected.

Figure 5 demonstrates yet a different perspective on these data: The  $f(E)$  value is shown as a function of glandular fraction for different incident photon energy levels in a 4-cm-thick breast. Monte Carlo runs were performed with several intermediate glandular fractions (0%, 20%, 40%, 50%, 60%, 80%, and 100%) for the data shown in Figure 5. The curves shown in Figure 4— $f(E)$  versus breast thickness—are nonlinear, whereas the curves in Figure 5— $f(E)$  versus glandular fraction—are linear. This observation suggests that lin-

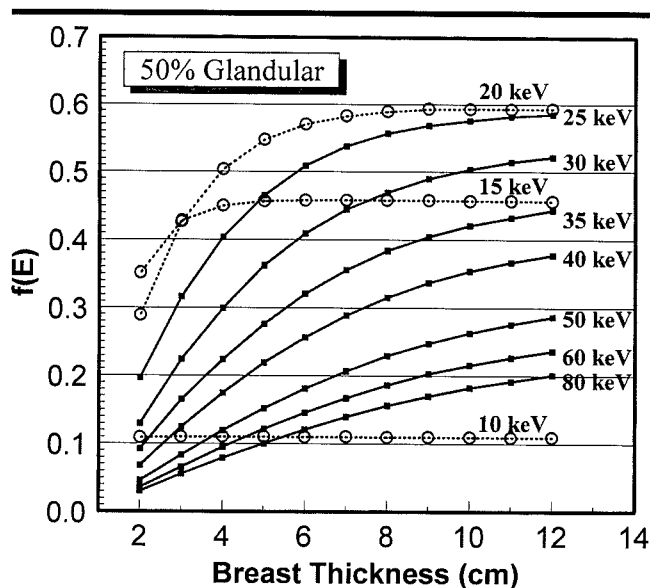


**Figure 4.** Graph shows data for a 50% glandular breast, with  $f(E)$  as a function of breast thickness. The  $f(E)$  value is almost constant as a function of breast thickness. The fact that the 10-keV photon absorption fraction is nonzero implies that 10-keV photons penetrate the skin layer, but the constant behavior as a function of breast thicknesses implies that the absorption kinetics take place principally in the first 2 cm of the breast. Higher energy photons show increased penetration of the skin layer ( $f(E)$  values are higher for the 2-cm breast thickness) and also demonstrate that increased tissue absorption occurs with thicker breasts, as would be expected. Different symbols (■ and ○) and solid and dotted lines do not represent differences in data but were used for ease of reading.

ear interpolation between glandular fraction data, for the  $f(E)$  values, was reasonable and preferable in comparison with

interpolation between breast thicknesses. As a result, only 0% glandular (100% adipose) and 100% glandular results need

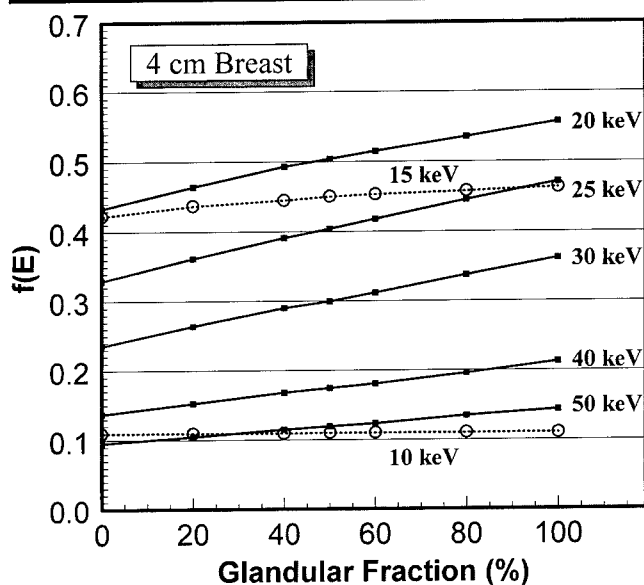


Figure 5. Graph shows  $f(E)$  as a function of glandular fraction for various x-ray energies and a 4-cm breast thickness. The  $f(E)$  curve is a nearly linear function of glandular fraction, as evidenced by the linearity of the curves. Different symbols (■ and ○) and solid and dotted lines do not represent differences in data but were used for ease of reading.

to be reported because other proportions can easily be calculated.

#### Comparison with $D_{gN}$ Values in the Literature

The  $D_{gN}$  values computed in the present study were compared with the results of Dance (5), as illustrated in Figure 6. Dance presented conversion factors in different units (mean glandular dose per incident air kerma,  $mGy \cdot mGy^{-1}$ ), which were recomputed to the units of millirad per roentgen for this comparison. The skin thickness was set to 5 mm, and a 50% glandular breast was modeled, consistent with Dance's method. Four breast thicknesses, 2, 4, 6, and 8 cm, were studied for this comparison. When the different Monte Carlo routines, and particularly the different x-ray spectra, used to produce these data are considered, the qualitative agreement seen in Figure 6 between Dance's data and the data from this study is good. The 4-cm-thickness data were subjected to quantitative comparison. Because the half-value layers (HVLs) corresponding to both data sets differed on a point-by-point basis, direct comparisons between the data sets were not possible. Therefore, both data sets were computer fit by using commercially available software (TABLECURVE 3.0; Jandel Scientific, Corta Madera, Calif), with excellent precision (4-cm-thickness data from Dance:  $r^2 = 0.9999$ ; 4-cm-thickness

data from present study:  $r^2 = 0.9975$ ), and comparison was then made between the computer-fit  $D_{gN}$  values (between data sets) over the HVL range of 0.25-mm aluminum to 1.3-mm aluminum. The 4-cm-thickness data from the present study were found to differ from those of Dance, on average, by  $-1.12\%$  (SD, 2.66). In terms of absolute  $D_{gN}$  values, the difference was  $-3.34$  mrad/R (SD, 10.6).

The data of Wu et al (4) are the most commonly used  $D_{gN}$  values in the United States. The  $D_{gN}$  values reported in the present study were calculated at exactly the same HVLs as those of Wu et al; thus, a direct comparison was possible. These comparative data are shown in Figure 7.  $D_{gN}$  values calculated at three breast thicknesses (4, 6, and 8 cm) and at seven kilovoltages (23–35 kV in increments of 2 kV) are shown for each breast composition. The  $D_{gN}$  values observed in this study were consistent with, but slightly lower than, those of Wu et al for a 0% glandular breast but were seen to be in excellent agreement with the values of Wu et al for 50% and 100% glandular breast compositions. The slight qualitative differences (5%–7%) in the data for a 0% glandular breast may be a consequence of different extrapolation techniques for a 0% glandular breast. The spectra computed for this study were hardened by adding an acrylic plastic sheet, such that the HVLs exactly matched those reported by Wu et al. While the kilovoltages and HVLs were identical, the  $D_{gN}$

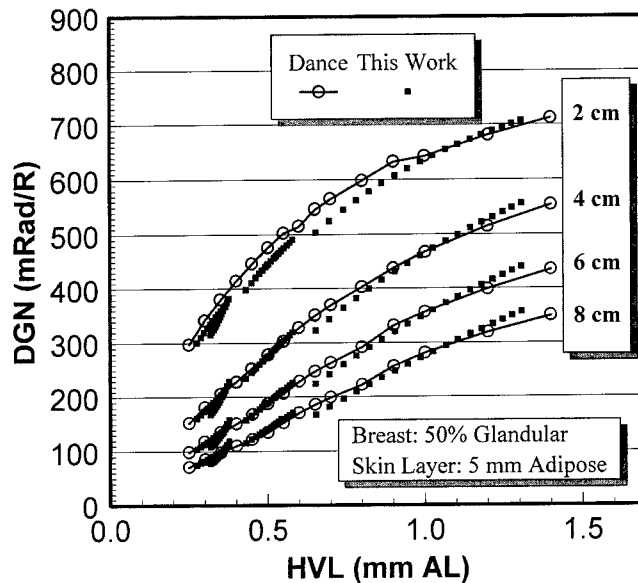


Figure 6. Graph shows  $D_{gN}$  values computed by Dance (5) (○) in comparison with those computed in the present study (■) for breast thicknesses of 2, 4, 6, and 8 cm. Dance reported  $D_{gN}$  values as a function of the HVL of the x-ray beam, and that approach was adopted here as well. A good qualitative comparison is shown.

values calculated in the present study did make use of a different spectral model (25) than that (29) used by Wu et al, and this may explain the slight differences between the  $D_{gN}$  values derived in the present study and those derived in the study by Wu et al.

For the 0% glandular data, the mean differences (and SDs) averaged over the seven spectra (23, 25, 27, 29, 31, 33, and 35 kV) were  $-5.5\%$  (SD, 1.3),  $-6.3\%$  (SD, 1.7), and  $-6.8\%$  (SD, 1.5) for the 4-, 6-, and 8-cm breast thicknesses, respectively. For the 50% glandular breast, the mean differences were  $-1.5\%$  (SD, 1.4),  $-1.9\%$  (SD, 1.5), and  $-2.3\%$  (SD, 1.6) for the 4-, 6-, and 8-cm breast thicknesses, respectively. For the 100% glandular breast, the mean differences were 0.6% (SD, 1.5), 1.0% (SD, 1.4), and 1.1% (SD, 1.7) for the 4-, 6-, and 8-cm breast thicknesses, respectively.

#### Influence of Skin Thickness

The calculation of glandular dose for a patient has many uncertainties associated with it, and estimation of cancer risk on the basis of the glandular dose has even more uncertainties. The uncertainties in calculating glandular dose include uncertainties not only in the tabulated  $D_{gN}$  values but also practical uncertainties in assessing the thickness of the breast, the breast composition, the precise milliampere-second value used, the differences between the actual mammographic

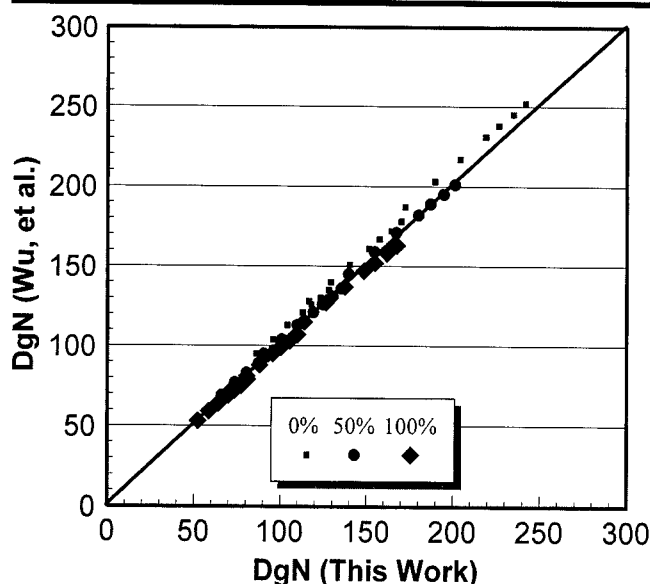


Figure 7. Graph shows  $D_{gN}$  values reported by Wu et al (4) along the y axis in comparison with  $D_{gN}$  values from the present study (along the x axis). Individual points represent the data obtained with an energy range of 23–35 kV (in 2-kV increments). The  $D_{gN}$  values reported here, averaged over all energy levels and breast thicknesses, differed from those of Wu et al by  $-6.2\%$  for the 0% glandular breast,  $-1.9\%$  for the 50% glandular breast, and  $+0.9\%$  for the 100% glandular breast.

geometry and that used in Monte Carlo simulations, and so on.

Figure 3 illustrates that the highest  $f(E)$  of incident x-ray photons occurred in the energy region from about 15 to 25 keV, where the  $f(E)$  curves peaked. Not coincidentally, this is the energy region where the vast majority of the x-ray photons in conventional x-ray spectra (eg, Mo-Mo combination at 26 kVp) exist. The fact that there was high absorption in the breast in this energy region also suggests that photons in this energy range are useful for the production of high-contrast images. As mentioned earlier, the left edges of the peaks of the  $f(E)$  curves seen in Figure 3 are a consequence of the absorption of incident x-rays by the skin layer. The steep slope of the left edges of the  $f(E)$  peaks suggests that a small difference in the assumption of skin thickness may have a large influence on the overall accuracy of the dose calculation.

To examine this in the case of the typical breast, Monte Carlo simulations were performed by using different skin thicknesses. Figure 8 illustrates the calculated  $D_{gN}$  values for a 50% glandular, 4-cm-thick breast. Averaged over the different x-ray spectra (23–35 kV), the change in  $D_{gN}$  values (relative to a 4-mm skin thickness) that resulted from different skin thicknesses was 15.2% (SD, 2.1) for a 2-mm-thick skin layer, 7.1% (SD, 0.9) for a 3-mm-thick skin layer,  $-6.4\%$  (SD,

0.7) for a 5-mm-thick skin layer, and  $-11.8\%$  (SD, 1.3) for a 6-mm-thick skin layer.

The observation that skin thickness has a large influence on the  $D_{gN}$  value is not surprising given the shape of the absorption curves (Fig 3). The purpose of presenting these data is to demonstrate that, among the uncertainties involved in dose calculations, it is likely that the slight differences ( $<6\%$ ) in tabulated  $D_{gN}$  values produced by different investigators are small, as compared with the large errors that can occur in making the wrong assumptions or generalizations about an individual patient's breast characteristics.

### Monoenergetic Beams

Figure 9 illustrates the monoenergetic  $D_{gN}$  values expressed in millirad per  $10^6$  photons per energy interval. Although the general shapes of these curves are similar to those of the  $f(E)$  curves in Figure 3, the influence of tissue thickness is inverted.  $D_{gN}$  values for the same x-ray energy and breast composition increased with decreasing breast thickness, because there is less self shielding in the thinner breast.

Although the  $D_{gN}$  values are high for thinner breasts, the entrance exposure during a mammogram is markedly lower in thin breasts; therefore, thin breasts typically receive substantially lower glandular doses than do thicker breasts. An alternate label

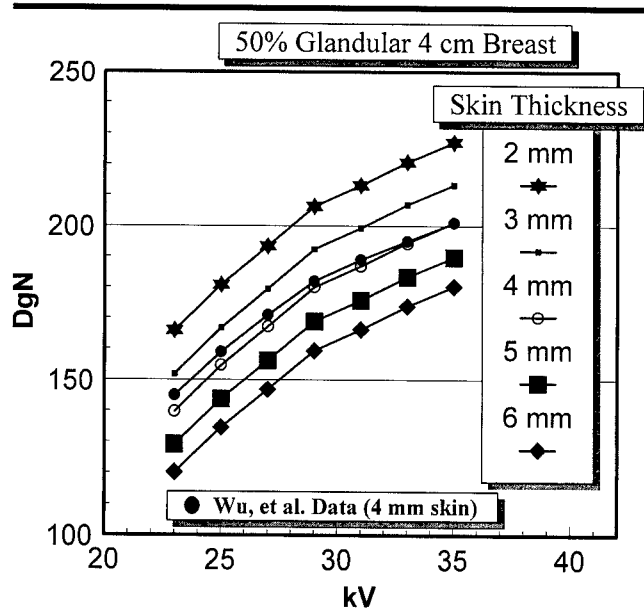


Figure 8. Graph illustrates the influence of skin thickness on the  $D_{gN}$  value. In comparison with the 4-mm skin thickness data from the study by Wu et al (4) (●), the  $D_{gN}$  values increased, on average, by 7% for a 3-mm skin thickness and by 15% for a 2-mm skin thickness. The  $D_{gN}$  values decreased by 6% for a 5-mm skin thickness and by 12% for a 6-mm skin thickness. These simulations used a Mo-Mo spectrum.

for the y axis in Figure 9 would be  $D_{gN} \times 10^{-6}$  per photon, or  $D_{gN}(E)$ . Therefore, by multiplying the data in Figure 9 by  $10^{-6}$  and then integrating the product of an incident x-ray spectrum ( $\Phi(E)$ ) and the appropriate curve in Figure 9 ( $D_{gN}(E)$ ), the  $D_{gN}$  value for an arbitrary spectrum can be calculated as shown below:

$$D_{gN} = \sum_{E=E_{min}}^{E_{max}} D_{gN}(E) \times 10^{-6} \times \Phi(E), \quad (8)$$

where it is understood that the total number of photons in  $\Phi(E)$  in Equation (8) is normalized to 1 R (0.258 mC/kg). The curves shown in Figure 9 coupled with the formula given in Equation (8) are most useful when one is dealing with an arbitrary x-ray spectrum, which is typically computed in units of photons per square millimeter per energy interval.

Photons at different energy levels contribute differently to exposure in air, owing to the energy dependence of the mass energy attenuation coefficient of air. As a consequence,  $D_{gN}$  values expressed in the traditional units of millirad per roentgen (vs x-ray energy) (Fig 10) have a different shape than those of the  $D_{gN}$  per photon curves in Figure 9. Figure 10 illustrates the millirad per roentgen  $D_{gN}$  values for 0% (Fig 10a) and 100% (Fig 10b) glandular tissue. Figure 10 is directly useful if one is interested in the  $D_{gN}$  value for a monoenergetic

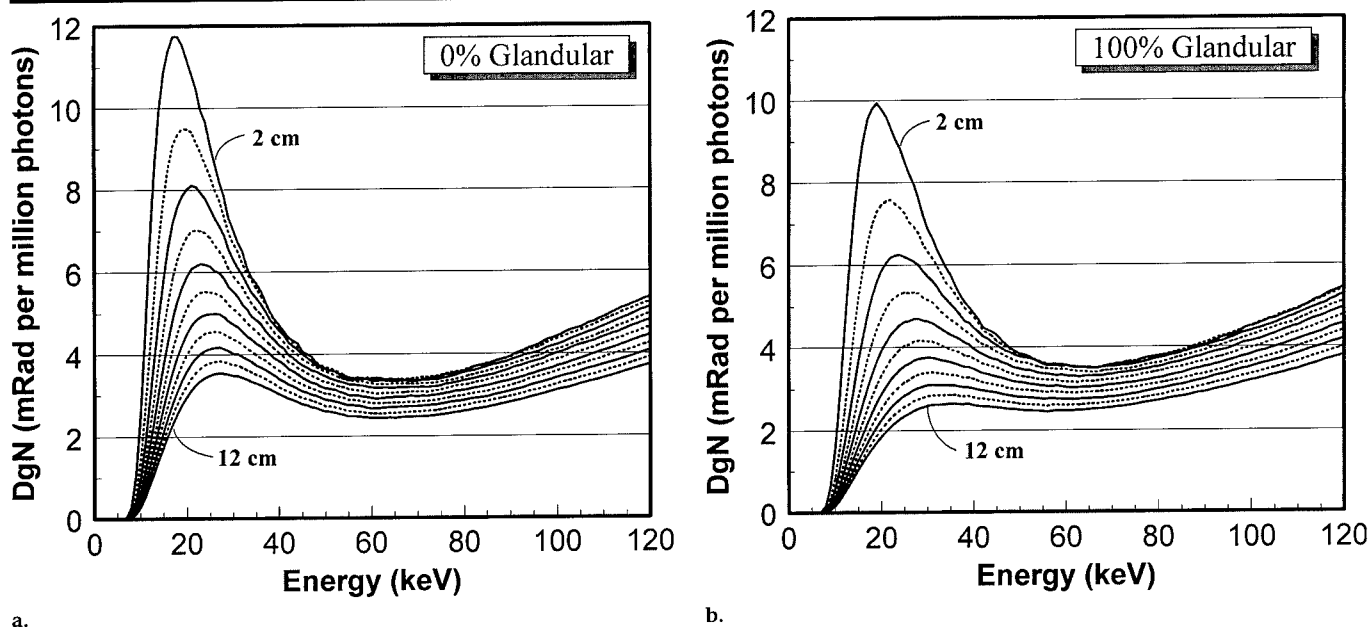


**Figure 9.** Graphs show  $D_{gN}$  values normalized per entrant photon instead of per roentgen (as is more typical) for (a) 0% glandular breasts and (b) 100% glandular breasts. Curves are shown for breast thicknesses ranging from 2 to 12 cm in 1-cm increments. The  $D_{gN}$  values shown here are higher for thin breasts and lower for thicker breasts, which is the reverse of the trend seen for  $f(E)$  in Figure 3. This graph illustrates that, on a per photon basis, photons in the energy region between approximately 12 and 30 keV contribute the most to the  $D_{gN}$  value. This is the energy region where most conventional mammographic x-ray spectra are centered.

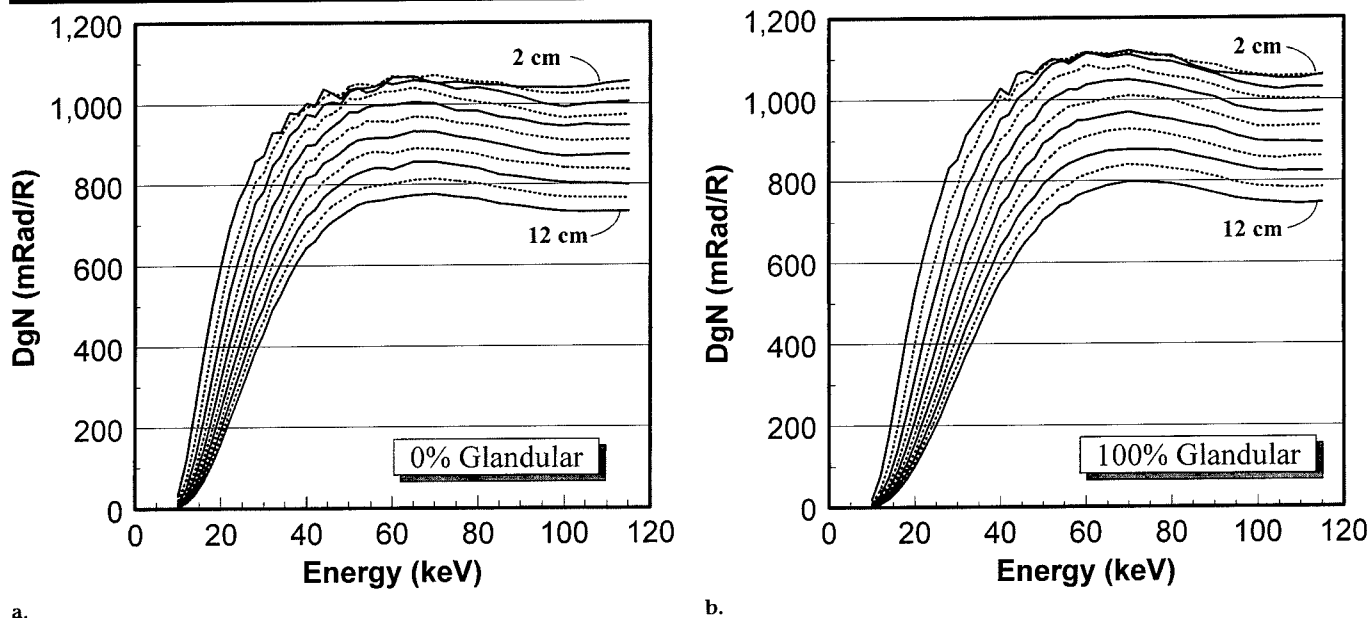


**Figure 10.** Graphs show  $D_{gN}$  values for monoenergetic x-ray energies for (a) 0% glandular breasts and (b) 100% glandular breasts. Breast thickness ranged from 2 to 12 cm in 2-cm increments. The  $D_{gN}$  values shown in these graphs are plotted in the conventional unit of millirad per roentgen, as opposed to millirad per photon as in Figure 9. The curves in this graph can be read directly when assessing  $D_{gN}$  for monoenergetic beams.

ergetic beam of 1-R (0.258-mC/kg) incident exposure to the breast.

### Mammographic Spectra

Tables 1–12 show the  $D_{gN}$  values for several conventional and unconventional

mammographic spectra. Tables 1, 3, 5, 7, 9, and 11 give  $D_{gN}$  values for the 0% glandular breast; Tables 2, 4, 6, 8, 10, and 12 give these values for the 100% glandular breast. For other glandular fractions,  $D_{gN}$  values may be linearly interpolated from the 0% and 100% glandular tables.

The data in Tables 1–12 were computed from simulations in which a 4-mm skin thickness was used. X-ray spectra were computed by using previously reported techniques (25). Tables 1–6 present  $D_{gN}$  values for conventional mammographic spectra, including Mo-Mo, Mo-Rh, and

**TABLE 1**  
 **$D_{gN}$  Values for Mo-Mo (30- $\mu$ m-thick) Anode-Filter Combination and a 0% Glandular Breast**

Energy (kV)	HVL	Breast Thickness (cm)										
		2	3	4	5	6	7	8	9	10	11	12
20	0.220	225	161	122	97	80	68	59	52	46	42	38
21	0.238	249	182	140	112	93	79	68	60	54	48	44
22	0.254	269	199	154	125	103	88	76	67	60	54	49
23	0.269	286	213	166	135	112	96	83	73	65	59	54
24	0.283	300	226	177	144	120	102	89	79	70	63	58
25	0.295	313	237	187	152	127	109	94	83	74	67	61
26	0.307	325	247	195	160	134	114	99	88	78	71	65
27	0.318	335	256	203	167	140	119	104	92	82	74	68
28	0.328	344	265	211	173	145	124	108	96	86	77	70
29	0.338	353	273	218	179	151	129	112	99	89	80	73
30	0.347	361	280	224	185	155	133	116	103	92	83	76
31	0.356	369	287	230	190	160	137	120	106	95	86	78
32	0.364	375	293	235	195	164	141	124	109	98	89	81
33	0.372	382	299	241	200	169	145	127	113	101	91	83
34	0.379	388	304	245	204	173	149	130	115	104	94	86
35	0.386	393	309	250	208	176	152	133	118	106	96	88
36	0.392	398	314	254	212	180	155	136	121	109	98	90
37	0.398	403	318	258	216	183	158	139	124	111	101	92
38	0.403	407	322	262	219	186	161	142	126	113	103	94
39	0.409	411	326	266	222	189	164	144	128	115	105	96
40	0.413	415	330	269	225	192	166	146	130	117	106	97

Note.— $D_{gN}$  values are expressed in millirad per roentgen. To convert to SI units ( $mGy \cdot mGy^{-1}$ ), multiply by  $873^{-1}$ .

**TABLE 2**  
 **$D_{gN}$  Values for Mo-Mo (30- $\mu$ m-thick) Anode-Filter Combination and a 100% Glandular Breast**

Energy (kV)	HVL	Breast Thickness (cm)										
		2	3	4	5	6	7	8	9	10	11	12
20	0.220	169	108	78	60	49	41	35	31	28	25	23
21	0.238	191	125	90	70	57	48	41	36	32	29	26
22	0.254	209	138	101	78	64	54	46	41	36	33	30
23	0.269	224	150	110	85	70	59	50	44	39	36	32
24	0.283	237	160	117	92	75	63	54	48	42	38	35
25	0.295	249	169	125	97	79	67	58	51	45	41	37
26	0.307	259	177	131	103	84	71	61	54	48	43	39
27	0.318	269	184	137	107	88	74	64	56	50	45	41
28	0.328	278	191	142	112	92	77	67	59	52	47	43
29	0.338	286	198	148	116	95	80	70	61	54	49	45
30	0.347	293	204	153	121	99	84	72	63	57	51	46
31	0.356	300	210	157	124	102	86	75	66	59	53	48
32	0.364	307	215	162	128	105	89	77	68	61	55	50
33	0.372	313	220	166	132	109	92	80	70	63	57	51
34	0.379	318	225	170	135	112	95	82	72	65	58	53
35	0.386	324	229	174	139	115	97	84	74	66	60	55
36	0.392	328	233	178	142	117	100	87	76	68	62	56
37	0.398	333	237	181	145	120	102	89	78	70	63	58
38	0.403	337	241	184	148	122	104	91	80	72	65	59
39	0.409	341	244	187	150	125	106	93	82	73	66	60
40	0.413	344	248	190	153	127	108	94	84	75	68	62

Note.— $D_{gN}$  values are expressed in millirad per roentgen. To convert to SI units ( $mGy \cdot mGy^{-1}$ ), multiply by  $873^{-1}$ .

Rh-Rh combinations. Tables 7-12 present  $D_{gN}$  values for unconventional mammographic spectra that are being considered as substitutes for use in women with thicker breasts and for digital mammography systems; these include W-Rh, W-Pd, and W-Ag combinations. Because of the strong L-characteristic x-ray emission of the tungsten anode around 12 keV, a

50- $\mu$ m thickness of filter material is needed to effectively eliminate these x-rays from the entrance beam.

Tables 1-12 allow interpolation across energy level (by using the HVL), thickness, and glandular fraction of the breast composition. For example, consider the case of a 4.2-cm-thick breast composed of 30% glandular and 70% adipose tissue

imaged at 26 kV with a Mo-Rh x-ray spectrum and an HVL of 0.37 mm aluminum: From Table 3 (0% glandular, Mo-Rh), the  $D_{gN}$  value at 4.2 cm and an HVL of 0.37 is interpolated from the four data points corresponding to 4- and 5-cm-thick breasts at HVLs of 0.363 mm aluminum (at 26 kV) and 0.375 mm aluminum (at 27 kV). In this case,  $D_{gN} = [236(0.8) +$

**TABLE 3**  
 **$D_{gN}$  Values for Mo-Rh (25- $\mu$ m-thick) Anode-Filter Combination and a 0% Glandular Breast**

Energy (kV)	HVL	Breast Thickness (cm)										
		2	3	4	5	6	7	8	9	10	11	12
20	0.241	247	178	136	109	90	76	66	58	51	46	42
21	0.265	276	204	158	128	106	90	78	69	62	55	51
22	0.288	303	228	179	146	121	103	90	79	71	64	58
23	0.310	326	249	197	162	135	116	101	89	80	72	65
24	0.331	346	267	213	175	147	126	110	97	87	79	72
25	0.348	362	281	225	186	157	135	118	104	93	84	77
26	0.363	374	293	236	195	165	141	124	109	98	89	81
27	0.375	385	302	244	202	171	147	129	114	102	92	84
28	0.387	394	310	251	209	177	152	133	118	105	95	87
29	0.397	402	317	257	214	181	156	137	121	109	98	90
30	0.406	409	324	263	219	186	160	140	124	112	101	92
31	0.415	415	329	268	224	190	164	143	127	114	103	94
32	0.422	420	335	273	228	194	167	146	130	117	106	96
33	0.429	425	339	277	232	197	170	149	133	119	108	98
34	0.436	430	344	281	235	200	173	152	135	121	110	100
35	0.442	434	348	285	239	203	176	154	137	123	112	102
36	0.447	438	351	288	242	206	178	157	139	125	114	104
37	0.453	442	355	291	245	209	181	159	142	127	115	105
38	0.457	445	358	294	247	211	183	161	143	129	117	107
39	0.462	448	361	297	250	214	185	163	145	131	119	108
40	0.466	451	364	299	252	216	187	165	147	132	120	110

Note.— $D_{gN}$  values are expressed in millirad per roentgen. To convert to SI units ( $mGy \cdot mGy^{-1}$ ), multiply by  $873^{-1}$ .

**TABLE 4**  
 **$D_{gN}$  Values for Mo-Rh (25- $\mu$ m-thick) Anode-Filter Combination and a 100% Glandular Breast**

Energy (kV)	HVL	Breast Thickness (cm)										
		2	3	4	5	6	7	8	9	10	11	12
20	0.241	187	121	87	67	54	46	39	35	31	28	25
21	0.265	215	142	103	80	65	55	47	42	37	33	30
22	0.288	239	161	119	93	76	64	55	48	43	39	35
23	0.310	261	178	133	104	85	72	62	54	48	44	40
24	0.331	279	193	145	114	93	79	68	60	53	48	44
25	0.348	294	205	154	122	100	84	73	64	57	51	47
26	0.363	306	215	162	128	105	89	77	68	60	54	49
27	0.375	315	223	168	133	110	93	80	70	63	57	52
28	0.387	324	230	174	138	114	96	83	73	65	59	53
29	0.397	331	236	179	142	117	99	86	75	67	61	55
30	0.406	338	241	183	146	120	102	88	78	69	62	57
31	0.415	344	246	187	149	123	104	90	79	71	64	58
32	0.422	349	250	191	152	126	107	92	81	73	66	60
33	0.429	354	255	195	155	128	109	95	83	74	67	61
34	0.436	358	258	198	158	131	111	96	85	76	69	62
35	0.442	362	262	201	161	133	113	98	87	77	70	64
36	0.447	366	265	204	164	136	115	100	88	79	71	65
37	0.453	370	269	207	166	138	117	102	90	81	73	66
38	0.457	373	271	209	168	140	119	104	92	82	74	67
39	0.462	376	274	212	170	142	121	105	93	83	75	69
40	0.466	379	277	214	173	144	123	107	94	85	76	70

Note.— $D_{gN}$  values are expressed in millirad per roentgen. To convert to SI units ( $mGy \cdot mGy^{-1}$ ), multiply by  $873^{-1}$ .

$195(0.2)] \times (0.417) + [244(0.8) + 202(0.2)] \times (0.583) = 232.35$  mrad/R. The values in parentheses are the interpolation weights, and the values in square brackets are the thickness-interpolation values. The corresponding calculation was used to compute the  $D_{gN}$  value for a 100% glandular breast by using the same interpolation coefficients and the  $D_{gN}$  val-

ues in Table 4, which yielded  $D_{gN} = [162(0.8) + 128(0.2)] \times (0.417) + [168(0.8) + 133(0.2)] \times (0.583) = 158.43$  mrad/R. By interpolating these two values to the 30% glandular fraction of the example, the result is  $D_{gN-30} = D_{gN-0}(0.7) + D_{gN-100}(0.3) = 232.35(0.7) + 158.43(0.3) = 210$  mrad/R, where  $D_{gN-30}$ ,  $D_{gN-0}$ , and  $D_{gN-100}$  are the  $D_{gN}$  values for 30%,

0%, and 100% glandular breasts, respectively.

### High-Energy Polyenergetic Beams

Figure 11 illustrates the  $D_{gN}$  values for polyenergetic x-ray beams in the general diagnostic energy region. Figure 11a shows results for the 0% glandular breast,

**TABLE 5**  
 **$D_{gN}$  Values for Rh-Rh (25- $\mu$ m-thick) Anode-Filter Combination and a 0% Glandular Breast**

Energy (kV)	HVL	Breast Thickness (cm)										
		2	3	4	5	6	7	8	9	10	11	12
20	0.245	252	182	140	112	93	79	68	60	53	48	44
21	0.265	278	206	160	130	108	92	80	70	63	57	52
22	0.278	293	219	171	139	116	99	86	76	68	61	56
23	0.294	311	236	187	153	128	110	95	84	75	68	62
24	0.312	330	254	203	167	141	121	105	93	83	75	69
25	0.329	348	270	218	180	152	131	114	101	91	82	75
26	0.345	363	285	231	192	163	140	123	109	97	88	80
27	0.361	377	299	243	203	172	149	130	116	104	94	86
28	0.376	390	311	254	213	181	157	137	122	110	99	91
29	0.391	402	322	264	222	189	164	144	128	115	104	95
30	0.405	412	332	274	231	197	171	150	134	120	109	99
31	0.418	422	342	283	239	204	177	156	139	125	113	103
32	0.431	431	351	291	246	211	183	161	144	129	117	107
33	0.443	440	359	299	253	217	189	167	148	133	121	111
34	0.454	447	367	306	259	223	194	171	153	137	125	114
35	0.465	455	374	312	265	229	199	176	157	141	128	117
36	0.476	461	380	318	271	234	204	180	161	145	131	120
37	0.486	467	386	324	276	238	208	184	164	148	135	123
38	0.495	473	392	329	281	243	212	188	168	151	138	126
39	0.504	479	397	335	286	247	216	192	171	154	140	129
40	0.513	484	402	339	290	251	220	195	174	157	143	131

Note.— $D_{gN}$  values are expressed in millirad per roentgen. To convert to SI units ( $mGy \cdot mGy^{-1}$ ), multiply by  $873^{-1}$ .

**TABLE 6**  
 **$D_{gN}$  Values for Rh-Rh (25- $\mu$ m-thick) Anode-Filter Combination and a 100% Glandular Breast**

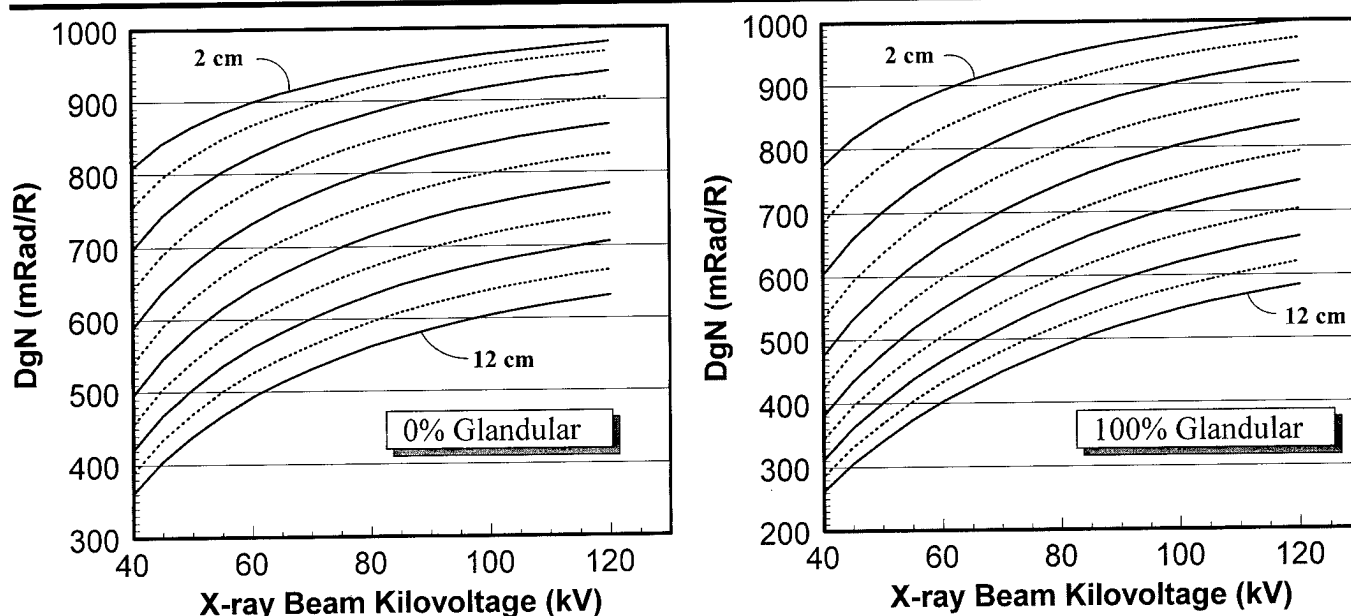
Energy (kV)	HVL	Breast Thickness (cm)										
		2	3	4	5	6	7	8	9	10	11	12
20	0.245	192	124	90	70	56	47	41	36	32	29	26
21	0.265	216	144	105	82	67	56	48	42	38	34	31
22	0.278	230	154	114	89	72	61	53	46	41	37	34
23	0.294	248	169	126	99	81	68	59	52	46	41	38
24	0.312	266	184	138	109	89	76	65	57	51	46	42
25	0.329	282	198	150	119	98	83	71	63	56	50	46
26	0.345	297	211	160	127	105	89	77	68	60	54	50
27	0.361	311	223	170	136	112	95	82	72	65	58	53
28	0.376	323	233	179	143	118	100	87	77	68	62	56
29	0.391	334	243	187	150	124	106	92	81	72	65	59
30	0.405	345	252	195	157	130	111	96	84	75	68	62
31	0.418	354	261	202	163	135	115	100	88	79	71	65
32	0.431	363	269	209	169	140	120	104	91	82	74	67
33	0.443	372	276	216	174	145	124	107	95	85	76	70
34	0.454	379	283	222	179	150	128	111	98	87	79	72
35	0.465	387	289	227	184	154	131	114	101	90	81	74
36	0.476	393	295	232	189	158	135	117	104	93	84	76
37	0.486	399	301	237	193	162	138	120	106	95	86	78
38	0.495	405	306	242	197	165	141	123	109	97	88	80
39	0.504	411	311	246	201	169	145	126	111	100	90	82
40	0.513	416	316	251	205	172	147	129	114	102	92	84

Note.— $D_{gN}$  values are expressed in millirad per roentgen. To convert to SI units ( $mGy \cdot mGy^{-1}$ ), multiply by  $873^{-1}$ .

and Figure 11b shows results for the 100% glandular breast. The x-ray spectra used for these calculations were generated by using a spectral model developed by the author (26). General radiographic (tungsten anode) x-ray spectra were computed from 40 to 120 kV, with the assumption of a 5% kilovoltage ripple (approximating an inverter generator), and with 2.5 mm

of added aluminum filtration. The HVL ranged from 1.6 mm aluminum at 40 kV to 5.0 mm aluminum at 120 kV, with an approximately linear relationship ( $r^2 = 0.998$ ) between HVL and kilovolt level, where  $kV = 23.318 \times HVL - 0.237$ . This relationship can be used to convert HVL values to the kilovolt values in Figure 11.

The  $D_{gN}$  values for these high-energy x-ray beams may be useful for calculating glandular breast dose in some general diagnostic radiographic studies (lateral views) or in computed tomographic studies, if certain assumptions are made. One of the higher energy beams may be useful as the high-energy component of a dual-energy mammography system.



a. b. **Figure 11.** Graphs show  $D_{gN}$  values for conventional polyenergetic x-ray beams in which a tungsten anode and 2.5 mm of added aluminum filtration are used.  $D_{gN}$  values are shown for (a) 0% glandular breasts and (b) 100% glandular breasts.

**TABLE 7**  
 $D_{gN}$  Values for W-Rh (50- $\mu$ m-thick) Anode-Filter Combination and a 0% Glandular Breast

Energy (kV)	HVL	Breast Thickness (cm)										
		2	3	4	5	6	7	8	9	10	11	12
20	0.338	342	258	202	164	136	116	101	89	79	71	65
21	0.365	368	282	224	183	153	131	114	100	90	81	74
22	0.392	392	306	245	202	170	146	127	112	101	91	83
23	0.420	415	328	266	221	187	161	140	124	111	101	92
24	0.444	434	347	284	237	201	174	152	135	121	109	100
25	0.462	447	360	296	248	211	183	160	142	128	116	106
26	0.477	457	370	305	257	219	190	167	148	133	120	110
27	0.489	465	378	313	264	226	195	172	153	137	124	113
28	0.500	472	385	320	270	231	200	176	157	141	128	116
29	0.509	478	391	326	275	236	205	180	160	144	131	119
30	0.518	484	397	331	280	241	209	184	164	147	134	122
31	0.527	489	403	336	285	245	213	188	168	151	137	125
32	0.535	494	408	342	290	250	218	192	171	154	140	128
33	0.544	499	413	347	295	254	222	196	175	158	143	131
34	0.552	504	418	352	300	259	226	200	179	161	146	134
35	0.560	509	424	357	306	264	231	205	183	165	150	137
36	0.569	514	429	363	311	269	236	209	187	169	154	141
37	0.577	519	434	368	316	275	241	214	192	173	158	144
38	0.585	524	440	373	321	280	246	218	196	177	161	148
39	0.593	528	444	379	327	285	251	223	200	181	165	152
40	0.601	532	449	383	331	289	255	227	204	185	169	155

Note.— $D_{gN}$  values are expressed in millirad per roentgen. To convert to SI units ( $\text{mGy} \cdot \text{mGy}^{-1}$ ), multiply by  $873^{-1}$ .

## DISCUSSION

In this study, Monte Carlo techniques were used to calculate  $D_{gN}$  values. As validation of the procedures used here,  $D_{gN}$  values for conventional mammographic spectra were compared with the results of the seminal work of Dance (5)

and Wu et al (4). The comparison with Dance's results showed agreement within about 1%, and comparisons with the data of Wu et al showed agreement within a range of about 1%–6%, depending upon breast glandularity. The influence of skin thickness was evaluated (Fig 8), and it was seen that a difference of 1

mm in skin thickness (eg, 3-mm instead of 4-mm skin thickness) had an influence of approximately 7% on the  $D_{gN}$  values and that a difference of 2 mm (eg, 2-mm instead of 4-mm skin thickness) had an influence of 15%. As a consequence, the difference between the  $D_{gN}$  values of Wu et al and those in the present study is



**TABLE 8**  
 **$D_{gN}$  Values for W-Rh (50- $\mu$ m-thick) Anode-Filter Combination and a 100% Glandular Breast**

Energy (kV)	HVL	Breast Thickness (cm)										
		2	3	4	5	6	7	8	9	10	11	12
20	0.338	271	182	133	104	84	71	61	54	48	43	39
21	0.365	296	203	150	118	96	81	70	61	55	49	45
22	0.392	320	223	167	132	108	91	79	69	61	55	50
23	0.420	342	243	184	146	120	101	88	77	69	62	56
24	0.444	361	260	199	158	131	111	96	84	75	68	62
25	0.462	374	272	209	167	138	117	101	89	80	72	65
26	0.477	384	281	217	174	144	122	106	93	83	75	68
27	0.489	392	289	223	179	149	126	109	96	86	77	70
28	0.500	399	295	229	184	153	130	112	99	88	80	73
29	0.509	405	301	234	188	156	133	115	102	91	82	75
30	0.518	411	306	239	193	160	136	118	104	93	84	76
31	0.527	417	311	244	197	164	140	121	107	95	86	78
32	0.535	422	317	248	201	168	143	124	110	98	88	80
33	0.544	427	322	253	206	172	147	127	112	100	91	83
34	0.552	433	327	258	210	176	150	131	115	103	93	85
35	0.560	438	333	263	215	180	154	134	119	106	96	88
36	0.569	443	338	269	220	185	158	138	122	109	99	90
37	0.577	449	344	274	225	190	163	142	126	113	102	93
38	0.585	454	350	280	230	194	167	146	130	117	105	96
39	0.593	459	355	285	235	199	172	151	134	120	109	99
40	0.601	464	360	290	240	204	176	155	137	124	112	102

Note.— $D_{gN}$  values are expressed in millirad per roentgen. To convert to SI units ( $mGy \cdot mGy^{-1}$ ), multiply by  $873^{-1}$ .

**TABLE 9**  
 **$D_{gN}$  Values for W-Pd (50- $\mu$ m-thick) Anode-Filter Combination and a 0% Glandular Breast**

Energy (kV)	HVL	Breast Thickness (cm)										
		2	3	4	5	6	7	8	9	10	11	12
20	0.341	345	260	204	166	138	117	102	90	80	72	66
21	0.369	371	285	226	185	155	132	115	102	91	82	75
22	0.396	396	309	247	204	172	147	128	114	102	92	84
23	0.424	418	331	268	223	189	162	142	126	113	102	93
24	0.452	439	352	288	241	205	177	155	138	124	112	102
25	0.478	458	371	306	258	220	191	167	149	134	121	110
26	0.497	471	384	319	270	231	200	176	157	141	128	117
27	0.514	482	395	329	279	239	208	183	163	147	133	121
28	0.527	490	403	337	286	246	214	189	168	151	137	125
29	0.539	497	410	344	293	252	219	193	173	155	141	129
30	0.550	503	417	350	298	257	224	198	177	159	144	132
31	0.560	509	423	356	304	262	229	202	181	163	148	135
32	0.570	514	428	362	309	267	233	206	184	166	151	138
33	0.579	520	434	367	314	272	238	211	188	170	154	141
34	0.588	525	439	372	319	277	242	215	192	173	158	144
35	0.597	530	444	378	325	282	247	219	196	177	161	148
36	0.606	534	449	383	330	287	252	223	200	181	165	151
37	0.615	539	455	388	335	292	257	228	205	185	169	155
38	0.624	543	460	393	340	297	261	233	209	189	172	158
39	0.632	548	464	398	345	301	266	237	213	193	176	161
40	0.640	552	469	403	350	306	270	241	217	197	179	165

Note.— $D_{gN}$  values are expressed in millirad per roentgen. To convert to SI units ( $mGy \cdot mGy^{-1}$ ), multiply by  $873^{-1}$ .

smaller than typical differences in skin thickness.

Once the results of the present study had been verified against existing results for conventional x-ray spectra, the methods were used to extend  $D_{gN}$  Monte Carlo calculations to 120 keV. A series of tables for possible mammographic spectral candidates has been provided to allow direct

calculations of breast dose. Monoenergetic results also were computed and are presented in Figure 10. These data may be useful for computing the  $D_{gN}$  values for arbitrary x-ray spectra, including those that may be useful for dual-energy mammography in the high-energy region.

Mammography as a modality continues to mature, and, at present, there are

several digital mammography systems nearing the marketplace. Digital images allow the ability to retrospectively manipulate the displayed contrast. While it is impossible to recover subject contrast that is not recorded by the detector, it is thought that the ability to enhance displayed contrast retrospectively will be useful in improving image contrast in the

**TABLE 10**  
 **$D_{gN}$  Values for W-Pd (50- $\mu$ m-thick) Anode-Filter Combination and a 100% Glandular Breast**

		Breast Thickness (cm)										
Energy (kV)	HVL	2	3	4	5	6	7	8	9	10	11	12
20	0.341	274	184	135	105	85	72	62	54	48	44	40
21	0.369	299	205	152	119	97	82	70	62	55	50	45
22	0.396	323	225	169	133	109	92	79	70	62	56	51
23	0.424	345	245	186	147	121	102	89	78	69	63	57
24	0.452	366	265	203	162	133	113	98	86	77	69	63
25	0.478	385	282	218	175	145	123	106	94	84	75	69
26	0.497	398	294	229	184	153	130	113	99	89	80	73
27	0.514	409	304	237	191	159	135	117	104	92	83	76
28	0.527	417	312	244	197	164	140	121	107	96	86	79
29	0.539	424	319	250	203	169	144	125	110	98	89	81
30	0.550	431	325	256	208	173	148	128	113	101	91	83
31	0.560	437	331	261	212	177	151	132	116	104	94	85
32	0.570	442	336	266	217	181	155	135	119	106	96	87
33	0.579	448	342	271	221	185	159	138	122	109	98	90
34	0.588	453	347	276	226	189	162	141	125	112	101	92
35	0.597	459	353	281	231	194	166	145	128	115	104	95
36	0.606	464	358	286	235	198	170	149	132	118	107	97
37	0.615	469	364	292	241	203	175	153	135	121	110	100
38	0.624	474	369	297	245	208	179	157	139	125	113	103
39	0.632	479	374	302	250	212	183	161	143	128	116	106
40	0.640	483	379	307	255	217	187	164	146	131	119	109

Note.— $D_{gN}$  values are expressed in millirad per roentgen. To convert to SI units ( $mGy \cdot mGy^{-1}$ ), multiply by  $873^{-1}$ .

**TABLE 11**  
 **$D_{gN}$  Values for W-Ag (50- $\mu$ m-thick) Anode-Filter Combination and a 0% Glandular Breast**

		Breast Thickness (cm)										
Energy (kV)	HVL	2	3	4	5	6	7	8	9	10	11	12
20	0.330	336	253	197	160	133	113	98	87	77	70	64
21	0.357	362	277	219	179	150	128	111	98	88	79	72
22	0.383	386	300	240	198	166	143	124	110	98	89	81
23	0.410	408	322	261	216	183	157	137	122	109	99	90
24	0.436	429	343	280	234	199	172	150	133	120	108	99
25	0.463	449	363	299	252	215	186	164	145	131	118	108
26	0.489	467	381	317	268	229	199	176	156	141	127	116
27	0.509	480	394	330	280	240	209	185	165	148	134	123
28	0.526	491	405	340	289	249	217	192	171	154	140	128
29	0.541	499	414	349	298	257	224	198	177	159	145	132
30	0.554	507	422	356	305	263	230	204	182	164	149	136
31	0.566	514	429	363	311	269	236	209	187	168	153	140
32	0.578	520	435	369	317	275	241	213	191	172	157	143
33	0.588	526	441	375	323	280	246	218	195	176	160	147
34	0.599	531	447	381	328	285	251	223	200	180	164	150
35	0.609	536	453	387	334	291	256	227	204	184	168	154
36	0.619	541	458	392	339	296	261	232	208	188	171	157
37	0.629	546	464	398	345	301	266	236	213	192	175	161
38	0.638	551	468	403	350	306	270	241	217	196	179	164
39	0.647	555	473	408	355	311	275	245	221	200	183	168
40	0.655	559	477	412	359	315	279	249	225	204	186	171

Note.— $D_{gN}$  values are expressed in millirad per roentgen. To convert to SI units ( $mGy \cdot mGy^{-1}$ ), multiply by  $873^{-1}$ .

clinical setting. If this assumption proves to be true after experience, it is likely that some compromises in subject contrast may be appropriate under some circumstances. For example, in women with larger breasts, where dose levels are much higher, a shift to harder x-ray spectra may be effective, and this is one reason why tungsten anodes with higher-atomic-

number filtration are under investigation (and why the relevant  $D_{gN}$  values are reported here). At least one design under commercial investigation involves a scanning slot beam of x rays; such a design places high heat-loading demands on the x-ray tube. Tungsten is a remarkable anode material because of its high melting point, and this is another reason why

tungsten may become more common in some digital mammography systems. To be fully evaluated, new spectra with unconventional anode and filter materials will be studied for their influence on both image quality and patient dose. The  $D_{gN}$  values reported here may be useful toward that end.

It is likely that alternate spectra will

**TABLE 12**  
 **$D_{gN}$  Values for W-Ag (50- $\mu$ m-thick) Anode-Filter Combination and a 100% Glandular Breast**

Energy (kV)	HVL	Breast Thickness (cm)										
		2	3	4	5	6	7	8	9	10	11	12
20	0.330	266	178	130	101	82	69	60	52	47	42	38
21	0.357	291	198	147	115	94	79	68	60	53	48	44
22	0.383	314	218	163	129	105	89	77	67	60	54	49
23	0.410	336	238	180	143	117	99	86	75	67	61	55
24	0.436	357	257	196	157	129	109	95	83	74	67	61
25	0.463	377	276	213	171	141	120	104	92	82	74	67
26	0.489	395	292	228	184	153	130	113	99	89	80	73
27	0.509	408	305	239	193	161	137	119	105	94	85	77
28	0.526	419	315	248	201	168	143	125	110	98	89	81
29	0.541	428	324	255	208	174	148	129	114	102	92	84
30	0.554	436	331	262	214	179	153	133	117	105	95	86
31	0.566	443	338	268	219	184	157	137	121	108	98	89
32	0.578	449	344	274	224	188	161	141	124	111	100	91
33	0.588	455	350	280	230	193	166	144	128	114	103	94
34	0.599	461	356	285	235	197	170	148	131	117	106	96
35	0.609	467	362	291	240	202	174	152	134	120	109	99
36	0.619	472	368	296	245	207	178	156	138	123	112	102
37	0.629	478	373	302	250	211	182	160	141	127	115	105
38	0.638	483	379	307	255	216	187	163	145	130	118	108
39	0.647	488	384	312	259	220	191	167	149	133	121	110
40	0.655	492	388	316	264	225	195	171	152	137	124	113

Note.— $D_{gN}$  values are expressed in millirad per roentgen. To convert to SI units ( $\text{mGy} \cdot \text{mGy}^{-1}$ ), multiply by  $873^{-1}$ .

continue to be studied to determine whether further optimization of the mammographic examination can be achieved, given various new technologic developments. Furthermore, there is a small group of women who have a compressed breast thickness exceeding 8 cm; in these cases,  $D_{gN}$  tables were not available, and, for such cases, x-ray spectra have not been optimized.

This study was intended to provide clinical medical physicists, as well as researchers, with the tools needed to calculate glandular breast dose for any arbitrary x-ray spectra in a simple but accurate manner. Efforts to computer fit these curves with adequate precision proved to be unsuccessful; therefore, the raw data in Figures 9 and 10 and in Tables 1–12 will be made available to all interested parties via e-mail request.

## APPENDIX

The elemental compositions and densities of breasts with different glandular proportions and of skin are given in Table A1.

**Acknowledgment:** Dermott Cullen, PhD, of the Lawrence Livermore National Laboratory (Livermore, Calif) was most helpful in discussions concerning the use of the TART97 code, and his contribution to this study is gratefully acknowledged.

## References

- Kulkarni RN, Supe SJ. Radiation dose to the breast during mammography: a comprehensive, realistic Monte Carlo calculation. *Phys Med Biol* 1984; 29:1257–1264.
- Doi K, Chan HP. Evaluation of absorbed dose in mammography: Monte Carlo simulation studies. *Radiology* 1980; 135:199–208.
- Dance DR. The Monte Carlo calculation of integral radiation dose in xeromammography. *Phys Med Biol* 1980; 25:25–37.
- Wu X, Barnes GT, Tucker DM. Spectral dependence of glandular tissue dose in screen-film mammography. *Radiology* 1991; 179:143–148.
- Dance DR. Monte Carlo calculation of conversion factors for the estimation of mean glandular breast dose. *Phys Med Biol* 1990; 35:1211–1219.
- Gingold EL, Wu X, Barnes GT. Contrast and dose with Mo-Mo, Mo-Rh, and Rh-Rh target-filter combinations in mammography. *Radiology* 1995; 195:639–644.
- Wu X, Gingold EL, Barnes GT, Tucker DM. Normalized average glandular dose in molybdenum target-rhodium filter and rhodium target-rhodium filter mammography. *Radiology* 1994; 193:83–89.
- Dance DR, Persliden J, Carlsson GA. Calculation of dose and contrast for two mammographic grids. *Phys Med Biol* 1992; 37:235–248.
- Ng KH, Aus RJ, DeWerd LA, Vetter JR. Entrance skin exposure and mean glandular dose: effect of scatter and field gradient at mammography. *Radiology* 1997; 205:395–398.
- Arfelli F, Bonvicini V, Bravin A, et al. A linear array silicon pixel detector: images

**TABLE A1**  
**Weight Fractions of Elements and Total Tissue Density as a Function of Glandular Weight Fraction**

Glandular Weight Fraction (%)	Total Tissue Density	Hydrogen	Carbon	Nitrogen	Oxygen	Phosphorus
0	0.9301	0.112	0.619	0.017	0.251	0.001
10	0.9399	0.111	0.576	0.019	0.294	0.001
20	0.9501	0.110	0.532	0.020	0.336	0.002
30	0.9605	0.109	0.488	0.022	0.379	0.002
40	0.9711	0.108	0.445	0.023	0.421	0.003
50	0.9819	0.107	0.401	0.025	0.464	0.003
60	0.9930	0.106	0.358	0.026	0.507	0.003
70	1.0044	0.105	0.315	0.028	0.549	0.004
80	1.0160	0.104	0.271	0.029	0.592	0.004
90	1.0278	0.103	0.227	0.030	0.634	0.005
100	1.0400	0.102	0.184	0.032	0.677	0.005
Skin	1.0900	0.098	0.178	0.050	0.667	0.007

Source.—Reference 28.

- of a mammographic test object and evaluation of delivered doses. *Phys Med Biol* 1997; 42:1565-1573.
11. Thilander-Klang AC, Ackerholm PH, Berlin IC, et al. Influence of anode-filter combinations on image quality and radiation dose in 965 women undergoing mammography. *Radiology* 1997; 203:348-354.
  12. Calicchia A, Gambaccini M, Indovina PL, Mazzei F, Pugliani L. Niobium/molybdenum K-edge filtration in mammography: contrast and dose evaluation. *Phys Med Biol* 1996; 41:1717-1726.
  13. Thiele DL, Craig AR. Mean glandular dose and the standard breast. *Australas Phys Eng Sci Med* 1996; 19:94-96.
  14. Gentry JR, DeWerd LA. TLD measurements of in vivo mammographic exposures and the calculated mean glandular dose across the United States. *Med Phys* 1996; 23:899-903.
  15. Monticciolo DL, Sprawls P, Kruse BD, Peterson JE. Optimization of radiation dose and image quality in mammography: a clinical evaluation of rhodium versus molybdenum. *South Med J* 1996; 89:391-394.
  16. Lee KH, Kandaiya S. Estimation of breast radiation dose in a mammographic system. *Appl Radiat Isot* 1996; 47:361-363.
  17. Faulkner K, Law J, Robson KJ. Assessment of mean glandular dose in mammography. *Br J Radiol* 1995; 68:877-881.
  18. Helvie MA, Chan HP, Adler DD, Boyd PG. Breast thickness in routine mammograms: effect on image quality and radiation dose. *AJR* 1994; 163:1371-1374.
  19. Boone JM, Shaber GS, Tecotzky M. Dual-energy mammography: a detector analysis. *Med Phys* 1990; 17:665-675.
  20. Burattini E, Cossu E, Di Maggio C, et al. Mammography with synchrotron radiation. *Radiology* 1995; 195:239-244.
  21. Tompkins PA, Abreu CC, Carroll FE, Xiao QF, MacDonald CA. Use of capillary optics as a beam intensifier for a Compton x-ray source. *Med Phys* 1994; 21:1777-1784.
  22. Boone JM, Seibert JA. Monte Carlo simulation of the scattered radiation distribution in diagnostic radiology. *Med Phys* 1988; 15:713-720.
  23. Boone JM, Seibert JA. Scattered energy deposition under shielding. *Invest Radiol* 1988; 23:627-631.
  24. Cullen DE. TART97 a coupled neutron-photon 3-D, combinatorial geometry Monte Carlo transport code. Livermore, Calif: Lawrence Livermore National Laboratory, 1997.
  25. Boone JM, Fewell TR, Jennings RJ. Molybdenum, rhodium, and tungsten anode spectral models using interpolating polynomials with application to mammography. *Med Phys* 1997; 24:1863-1874.
  26. Boone JM, Seibert JA. An accurate method for computer-generating tungsten anode x-ray spectra from 30 to 140 kV. *Med Phys* 1997; 24:1661-1670.
  27. Boone JM, Chavez AE. Comparison of x-ray cross sections for diagnostic and therapeutic medical physics. *Med Phys* 1996; 23:1997-2005.
  28. Hammerstein GR, Miller DW, White DR, Masterson ME, Woodard HQ, Laughlin JS. Absorbed radiation dose in mammography. *Radiology* 1979; 130:485-491.
  29. Tucker DM, Barnes GT, Wu XZ. Molybdenum target x-ray spectra: a semiempirical model. *Med Phys* 1991; 18:402-407.

# An edge spread technique for measurement of the scatter-to-primary ratio in mammography

Virgil N. Cooper III,<sup>a)</sup> John M. Boone,<sup>b)</sup> J. Anthony Seibert, and Claire J. Pellot-Barakat  
*University of California, Davis, Department of Radiology, 4701 X Street, Sacramento, California 95817*

(Received 13 September 1999; accepted for publication 1 March 2000)

An experimental measurement technique that directly measures the magnitude and spatial distribution of scatter in relation to primary radiation is presented in this work. The technique involves the acquisition of magnified edge spread function (ESF) images with and without scattering material present. The ESFs are normalized and subtracted to yield scatter-to-primary ratios (SPRs), along with the spatial distributions of scatter and primary radiation. Mammography is used as the modality to demonstrate the ESF method, which is applicable to all radiographic environments. Sets of three images were acquired with a modified clinical mammography system employing a flat panel detector for 2, 4, 6, and 8 cm thick breast tissue equivalent material phantoms composed of 0%, 43%, and 100% glandular tissue at four different kV settings. Beam stop measurements of scatter were used to validate the ESF methodology. There was good agreement of the mean SPRs between the beam stop and ESF methods. There was good precision in the ESF-determined SPRs with a coefficient of variation on the order of 5%. SPRs ranged from 0.2 to 2.0 and were effectively independent of energy for clinically realistic kVps. The measured SPRs for 2, 4, and 6 cm 0% glandular phantoms imaged at 28 kV were  $0.21 \pm 0.01$ ,  $0.39 \pm 0.01$ , and  $0.57 \pm 0.02$ , respectively. The measured SPRs for 2, 4, and 6 cm 43% glandular phantoms imaged at 28 kV were  $0.20 \pm 0.01$ ,  $0.35 \pm 0.02$ , and  $0.53 \pm 0.02$ , respectively. The measured SPRs for 2, 4, and 6 cm 100% glandular phantoms imaged at 28 kV were  $0.22 \pm 0.02$ ,  $0.42 \pm 0.03$ , and  $0.88 \pm 0.08$ , respectively. © 2000 American Association of Physicists in Medicine. [S0094-2405(00)02705-X]

Key words: scatter, scatter-to-primary ratio (SPR), measurement technique, edge spread function (ESF), mammography

## I. INTRODUCTION

It is well known that scattered x-rays reduce image contrast and therefore lower lesion conspicuity, especially for low contrast lesions.<sup>1-5</sup> This has important implications for breast imaging since, other than those containing microcalcifications, lesions are generally of similar composition and density to surrounding breast tissue. Hence, degradation of inherently low lesion contrast has important clinical repercussions. As a result, scatter in mammography and methods of reducing its effects have been studied by several authors.<sup>4,6-19</sup>

The first step in reducing the effects of scatter is to understand the nature of scatter and its resulting image signal. Heretofore, the classic beam stop technique was used to quantify the magnitude of scatter relative to primary radiation, and various theoretical and semi-empirical methods were used to separate the distribution of scatter and primary radiation signals.<sup>8,20-23</sup> In this work, an experimental technique that quantifies both the magnitude and spatial distribution of scatter is demonstrated. The technique involves the acquisition of spatially registered primary and primary-plus-scatter radiation edge spread images. The resulting edge spread functions (ESFs) are normalized and subtracted resulting in separate measurements of scatter and primary ra-

diation. The principal advantages of this technique are that the magnitude and spatial distribution of the scatter signal are measured directly and extrapolation techniques are not required as they are in using the beam stop method. The latter is important because the shape of the extrapolation function requires an assumption concerning the shape of the scatter point spread function (PSF) and is a source of ambiguity. This ambiguous extrapolation function can have a strong influence on the results.

As a vehicle to demonstrate the experimental ESF methodology, experimental measurement of scatter in the mammography setting is revisited 20 years after the early work of Barnes and Brezovich.<sup>7</sup> Many improvements in mammography have occurred since then, including the development of dedicated mammography systems employing molybdenum and rhodium targets, digital detectors, and x-ray generators with low kV ripple. The current availability of breast-mimicking phantoms allows scatter assessment in tissue equivalent phantoms. Scatter is studied for a range of breast compositions and thicknesses imaged over a range of beam qualities. Breast equivalent material slabs were used as the scattering media and a flat panel digital radiographic imaging system (Varian Imaging Products, Palo Alto, CA) was used for image acquisition.

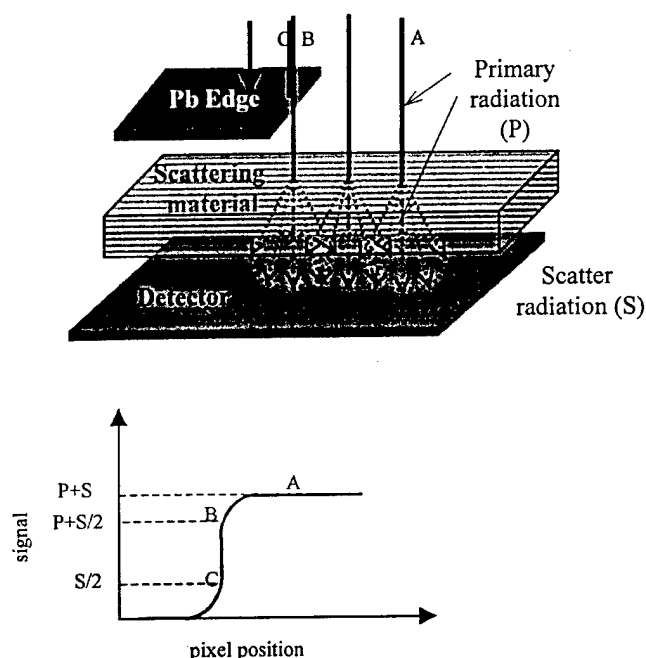


FIG. 1. The basic acquisition geometry: X-rays incident on a Pb edge placed on a scattering phantom. The edge is oriented parallel to the anode-cathode axis and bisects the x-ray field. A digital detector resides beneath the scattering medium. Below: the resulting signal profile.

## II. MATERIALS AND METHODS

### A. Theory

An experimental technique using edge spread functions (ESFs) to quantify the detected scattered radiation in relation to primary radiation is described in this section. This technique also gives a direct measurement of the spatial distribution of scatter, differentiating it from the beam stop technique. The direct measurement of the spatial distribution of scatter may be useful for the development of scatter correction algorithms pertinent to quantitative digital mammography (e.g., dual energy mammography or breast density analysis).

A parallel beam of x-rays incident on an elevated thick Pb sheet with the Pb edge oriented parallel to the anode-cathode axis is illustrated in Fig. 1. A digital detector is positioned beneath the Pb sheet and intercepts the entire field. A slab of scattering material resides between the sheet and detector. Labels "A," "B," and "C," refer to the points centrally located in the open field, located adjacent to the edge in the open field, and located adjacent to the edge in the closed field, respectively. The resulting image profile or edge spread function (ESF) is also depicted in Fig. 1.

If the edge were re-oriented 180 degrees from its original position, a mirror image profile would result. Figure 2 shows the resulting profiles, denoted by ESF\_L and ESF\_R, and their sum. Qualitatively, the addition of those two profiles results in a flat profile across the field (ignoring field edge effects) and this profile is equivalent to a profile measured for a fully open field. Since the ESF profiles are mirror images of one another, the toe of one ESF curve compensates for the shoulder of the other curve. Physically, the toe of the

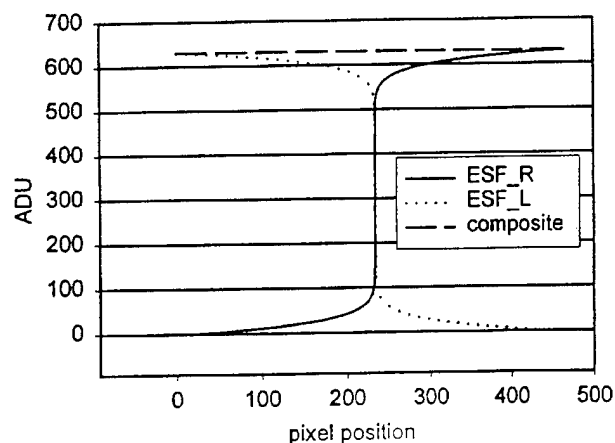


FIG. 2. This schematic illustration shows that for an effectively infinite field, primary plus scatter ESF profiles acquired 180 degrees from one another sum to the profile for a totally open field.

profile is composed of scattered radiation signal and the plateau of the curve is composed of scatter and primary radiation signals. The shoulder is also composed of scatter and primary radiation signals. The presence of this shoulder is a manifestation of scattered radiation signal that "leaks" across the discontinuity of the edge and forms the toe. Therefore, it follows that, by subtracting the different parts of the edge profile, scatter and primary radiation may be separated in a single edge profile.

The signals arising from scatter and primary radiation may be separated by the following argument. Referring to Fig. 3, if the length,  $L$ , and width,  $W$ , of the open field are

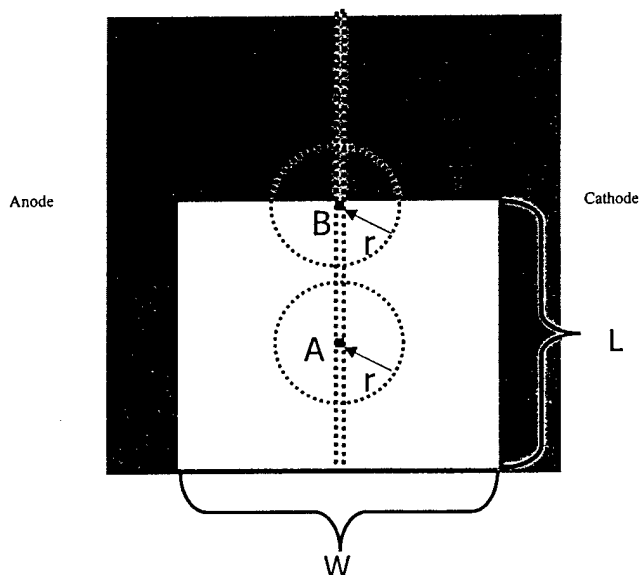


FIG. 3. This schematic illustration shows that an effectively infinite open field in this work, is one that is at least twice as wide (width denoted by  $W$ ) as the radial range of scatter,  $r$ , and at least twice as long (length denoted by  $L$ ). In this case point B (adjacent to the edge but in the open field) will receive one-half the scatter that point A (centrally located in the open field) receives. The dotted line denotes a 10 pixel wide region of interest (ROI) perpendicular to the anode-cathode axis from which the edge spread function (ESF) is derived.

each greater than twice the effective radial range of scatter,  $r$  (found to be between 4 and 6 cm in this work), then the scatter component of the signal at point B is one-half the scatter component at point A. This is because point A receives scatter from the scattering medium over  $2\pi$  geometry, while point B receives scatter from the scattering medium over  $\pi$  geometry since  $\pi$  radians adjacent to point B are covered by the Pb sheet and therefore do not generate first order scatter. Points A and B receive essentially the same amount of primary radiation. Hence, the scatter-to-primary ratio (SPR) at point B is one-half the SPR at point A.

Given the composition of the signals at pixel positions A and B, the scatter-to-primary ratio may be calculated. The signals at A and B may be, respectively, written as

$$ESF_A = P + S, \quad (1)$$

$$ESF_B = P + S/2, \quad (2)$$

where  $P$  is the signal due to primary radiation and  $S$  is the maximum signal due to scatter radiation (corresponding to the center of the open field, point A) and  $ESF_m$  is the signal value at the  $m$ th pixel position due to scatter and primary radiation. Therefore, scatter, primary, and the scatter-to-primary ratio at point A (SPR) may be computed from the digital signal values (among other ways) as:

$$S = 2 \times (ESF_A - ESF_B), \quad (3)$$

$$P = ESF_A - S, \quad (4)$$

$$SPR = S/P. \quad (5)$$

Since the imaging system under consideration does not exhibit perfect resolution, nor does it use parallel rays, these effects must be considered. If the scattering material in the experimental setup is removed without disturbing the rest of the system, then image acquisition results in a primary profile that is spatially aligned with the primary-plus-scatter (P+S) profile. However, with the removal of the scattering material, the shape of the primary profile will be slightly different than that with the scattering material present because the primary photons traveling at different angles will traverse different pathlengths through the phantom. For the field sizes, source-to-object distance, energies, and scattering materials involved, the maximum parallax error was found to be on the order of 0.5%, and therefore was considered negligible.

In the acquisition of the primary-only image, the x-ray intensity may be normalized such that the maximum open field signal matches the open field signal acquired with the scattering material present. Figure 4(a) shows the matched primary and primary plus scatter (P+S) profiles. The non-zero signal of the P+S profile under the radiopaque sheet arises from the detection of scatter originating from x-ray interactions with the phantom in the open field. The presence of the shoulder in the P+S profile, positioned near the edge of the open field, is due to the scatter lost to the covered field region.

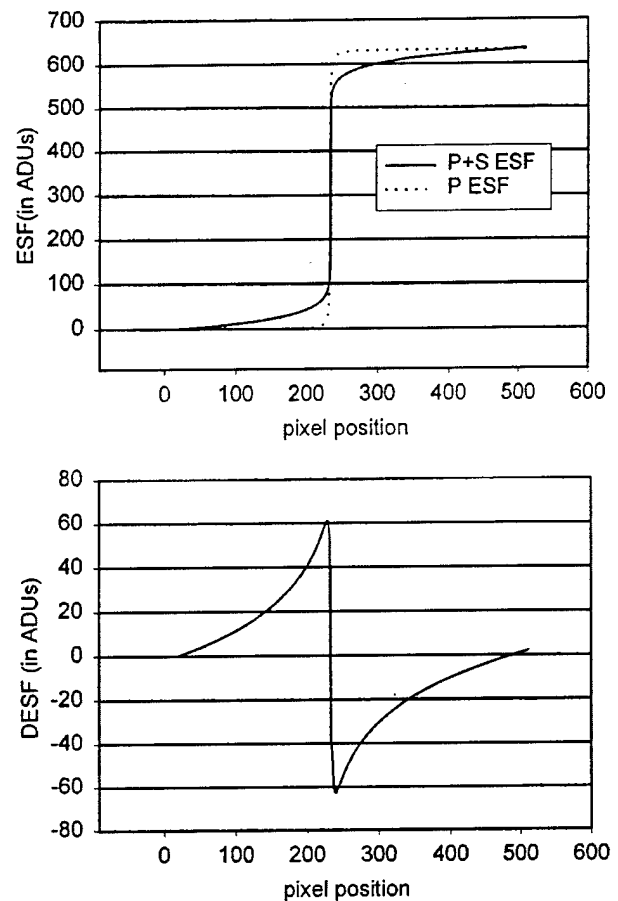


FIG. 4. (a) Matched primary-only and primary plus scatter ESFs and (b) the resulting profile if the primary ESF is subtracted from the primary plus scatter ESF. The magnitude of the discontinuity in this profile is equal to the scatter signal at the center of the open field (previously denoted by point A).

While there are several ways of quantifying the maximum scatter signal, a difference profile may be computed from Fig. 4(a) as

$$DESF_m = ESF_m - PESF_m, \quad (6)$$

where  $DESF_m$  is the signal difference at the  $m$ th pixel position,  $ESF_m$  is the signal value at the  $m$ th pixel position due to scatter and primary radiation, and  $PESF_m$  is the signal value at the  $m$ th pixel position due to primary radiation.

Figure 4(b) shows the resultant  $DESF$ . The positive and negative peaks, respectively, correspond to the maximum scatter gain in the covered field and maximum scatter loss in the open field. Thus, the signal due to scatter at the center of the open field in Eq. (3) may be rewritten as:

$$S = 2 \times |DESF_B|, \quad (7)$$

where  $DESF_B$  corresponds to the difference profile value at point B in Fig. 1. Since there is symmetry in the scatter losses from the open field and scatter gains in the covered field about the discontinuity of the edge, scatter signal may also be calculated as

$$S = DESF_C + |DESF_B|, \quad (8)$$

where  $DESFC$  corresponds to the difference profile value at point C in Fig. 1. Since the scatter signal at the center of the open field, point A, is isolated by Eq. (8), the primary signal component and the SPR may be calculated, respectively, from Eqs. (4) and (5).

Since the primary signal at point A, given by  $P$ , and the functional form of primary signal are known, the primary-only ESF may be renormalized such that the value at point A is equivalent to  $P$ . Thus the entire primary ESF would be correctly scaled and give the signal due to primary radiation along the center of the field. Given the renormalized primary ESF, the scatter ESF,  $SESF$ , is computed by subtracting the renormalized primary ESF,  $NPESF$ , from the total signal profile and is given as:

$$SESF_m = ESF_m - NPESF_m. \quad (9)$$

$SESF$  is then differentiated to yield the scatter line spread function.

## B. Experimental conditions

Breast equivalent material phantoms representing 0%, 43%, and 100% glandular tissue (Computerized Imaging Reference Systems, Inc., Norfolk, VA) were imaged with a clinical mammography system employing a molybdenum target and 30  $\mu\text{m}$  thick molybdenum filter (Senographe 600T Senix H.F., General Electric Medical Systems). The images were acquired with a flat panel imaging system employing thin film transistor circuitry, 127  $\mu\text{m}$  pixels, and a 60  $\text{mg}/\text{cm}^2$   $\text{Gd}_2\text{O}_2\text{S}$  intensifying screen (Varian Imaging Products, Palo Alto, CA). As calculated by simple attenuation methods, the detection system represented greater than 90% interaction efficiency for all spectra employed. The flat panel detector resided under a custom fabricated stand which allowed placement of the breast equivalent material with a 1.5 cm air gap on the incident surface of the detector and beneath the top surface of the stand. The focal spot to image receptor distance was 122 cm. The top surface of the stand was located 111 cm from the focal spot and was covered by lead except for a square cutout representing a projected 10  $\text{cm} \times 10$  cm "open" field of view. Lead (1.5 mm thick) with finely cut straight edges was used to confine this field. An edge was oriented parallel to the anode-cathode axis and bisecting the x-ray field and was used for computing the ESFs. Since scatter is a known low-frequency phenomenon and occurs well below the Nyquist frequency of the flat panel imaging system, there was no need to angle the edge for oversampling. Phantoms ranging from 2 to 8 cm in thickness in 2 cm increments were imaged from 24 to 36 kVp in 4 kVp increments. Each data set was acquired three times for repeated measures estimation of error. Table I lists the half-value layers for the incident spectra used in this study.

The breast equivalent phantoms were imaged at very similar radiation exposures incident to the detector. The resultant signal data due to scattered and primary radiation measured in the open field were consequently very similar in amplitude. After imaging the breast phantoms, they were carefully removed so as not to disturb the setup. Images were

TABLE I. Beam quality parameters.

kVp	HVL (mm Al)
24	0.30
28	0.32
32	0.37
36	0.38

again acquired, representing primary-only images. It was found that there was no appreciable difference in the spatial distribution of the primary-only images of the edge as a function of kVp.

## C. Image correction

All images were gain and offset-corrected using gain and offset maps constructed from five image acquisitions each of white (x-rays on) and dark (x-rays off) fields. The gain map was constructed such that the radiation exposure levels to the incident surface of the detector were very similar to those exposure levels during the ESF acquisitions.

Careful examination of the images showed a non-negligible amount of low-frequency signal in the images similar to that that would be expected from veiling glare. (This low-frequency signal variation is hereafter referred to as "glare" in this manuscript.) Lead beam stop experiments (with no phantom present) were subsequently performed to quantify this glare using the methodology of Seibert *et al.*<sup>24</sup> The glare point spread function,  $h(r)$ , was found to have the form given by:

$$h(r) = (1 - \rho) \times \frac{\delta(r)}{r} + \frac{\rho}{2kr} \times e^{-r/k}, \quad (10)$$

where  $r$  is radial distance,  $\delta(r)$  is the Dirac delta function,  $\rho$  is the fraction of strongly scattered light, and  $k$  is the mean propagation distance of that light. For the detector used in this work,  $\rho$  and  $k$  were found to have values of 0.069 and 7.33 mm, respectively.

The images were cropped to  $1024 \times 1024$  and deconvolved<sup>25</sup> with the inverse filter given by

$$H(f)^{-1} = \frac{\sqrt{1 + (2\pi kf)^2}}{\rho + (1 - \rho) \times \sqrt{1 + (2\pi kf)^2}}, \quad (11)$$

where  $f$  is the spatial frequency. For the two dimensional images,  $f$  was taken to be given by

$$f = \sqrt{u^2 + v^2}, \quad (12)$$

where  $u$  and  $v$  are the spatial frequencies across rows and columns.

## D. ESF calculations

After the images were deconvolved for glare, a rectangular region of interest (ROI) was positioned on the images and an ESF was calculated for each image. The ROI was chosen such that it was sufficiently wide to allow reasonable averaging (10 pixels or 1.27 mm), while narrow enough such that there was no appreciable difference between the profiles of



the lateralmost extents of the ROI (i.e., no rotation). The length of the ROI was 600 pixels (76 mm), sufficiently long to encompass the ESF from the center of the field of view to well beyond the collimated edge of the field. The ESF was calculated as:

$$ESF_m = \frac{1}{N} \times \sum_{n=1}^N ADU_{m,n}, \quad (13)$$

where  $n$  is the column index,  $N$  is the number of columns in the ROI, and the summation is along the anode-cathode axis (i.e., across the short-axis dimension of the ROI).  $ADU_{m,n}$  is the digital signal value at the  $m$ th by  $n$ th pixel. The same ROI/averaging protocol was done for the primary-only ESF as well. The magnitudes of scatter signal, primary signal, and their spatial distributions were calculated from the measured data using Eqs. (4)–(6), (8), and (9).

The resulting scatter ESFs were functionally fitted using commercially available software (Table Curve 2D, Jandel Scientific, Corta Madera, CA) and numerically differentiated to yield line spread functions (LSFs). These LSFs were subsequently Fourier transformed and normalized to yield scatter MTFs.

### E. Beam stop measurements

To validate the ESF methodology, images were acquired and SPRs were calculated using the conventional beam stop method. A linear extrapolation function,<sup>26</sup> and six beam stops having 0.3, 0.4, 0.5, 1.0, 2.0, and 3.0 cm diameters, were used in the beam stop experiments. The same field size and *a priori* selected exposure scenarios covering the entire range of realistic clinical conditions were utilized. As with the ESF measurements, all images were acquired for each beam stop in sets of three for repeated-measures estimation of error. The ROIs used in the centers of the beam stop shadows were 3-pixel-wide squares. Each image was deconvolved for glare using the same inverse filter as in the ESF methodology. Linear regression analysis was performed on the mean SPRs measured with both methodologies.

## III. RESULTS AND DISCUSSION

Figure 5(a) and (b) shows the comparison of the mean SPRs calculated via the ESF and beam stop methods. There is good agreement ( $r^2=0.97$ , slope=0.98, intercept=0.02) between the beam stop method and ESF method.

Figure 6(a)–(c) gives the resultant SPR plots as functions of kVp for each thickness under consideration. Figure 6(d) shows the SPRs as a function of thickness and glandularity at 28 kVp. Table II lists the SPRs in tabular form. The SPRs for the different compositions and thicknesses are effectively energy independent above certain energy thresholds. At the lower energies for the thicker breast phantoms the SPRs were markedly elevated (e.g., the 6 cm, 43% glandular phantom imaged at 24 kVp, the 8 cm, 43% glandular phantom imaged at 28 kVp, the 6 cm, 100% glandular breast imaged at 28 kVp, etc.). This phenomenon could represent inadequate penetration of the phantoms due to generator power

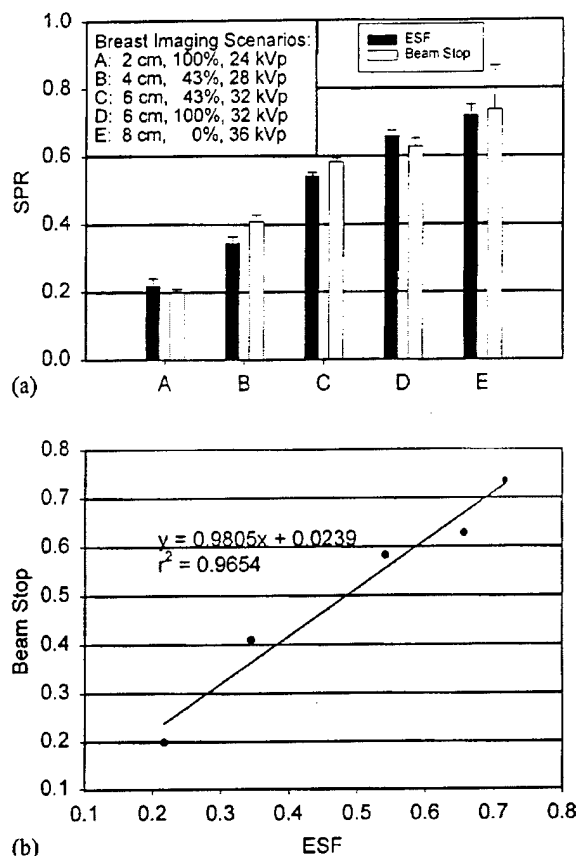


FIG. 5. Comparison of the edge spread and beam stop methods. There is good agreement between the two methods.

constraints and limited detector dynamic range. Therefore these SPRs are artificially elevated and should be looked upon with great suspicion. Furthermore, the imaging scenarios (kVp, thickness, and glandularity) that produced these SPRs are probably clinically unrealistic. Nevertheless, they are included for completeness.

It is difficult to compare this work with the work of Barnes and Brezovich, as they used a tungsten target and (presumably) a single-phase generator, a 0 cm air gap, and markedly different kVps. In addition, Lucite was used as the scattering phantom in the Barnes and Brezovich research. Lucite has a higher density (1.19 g/cm<sup>3</sup>) and different elemental composition than breast tissue, and is not consistent with the scattering media used in this work. For the purposes of comparison, however, SPRs for the exposure scenarios most closely resembling those used by Barnes and Brezovich are presented in Table III(a). Poor agreement between the two data sets is observed.

Table III(b) presents a comparison with the work of Dance and Day. The SPRs listed do not include the extraneous sources of scatter as described in their work. Since they simulated a 50% glandular breast at monochromatic energies and since the effective energies of the beams used in this work ranged between 14.22 and 15.24 keV, the SPRs contained in this work for the 43% glandular breast were averaged across energy and are presented for comparison. The SPR listed in Table III(b) for the 6 cm breast does not in-

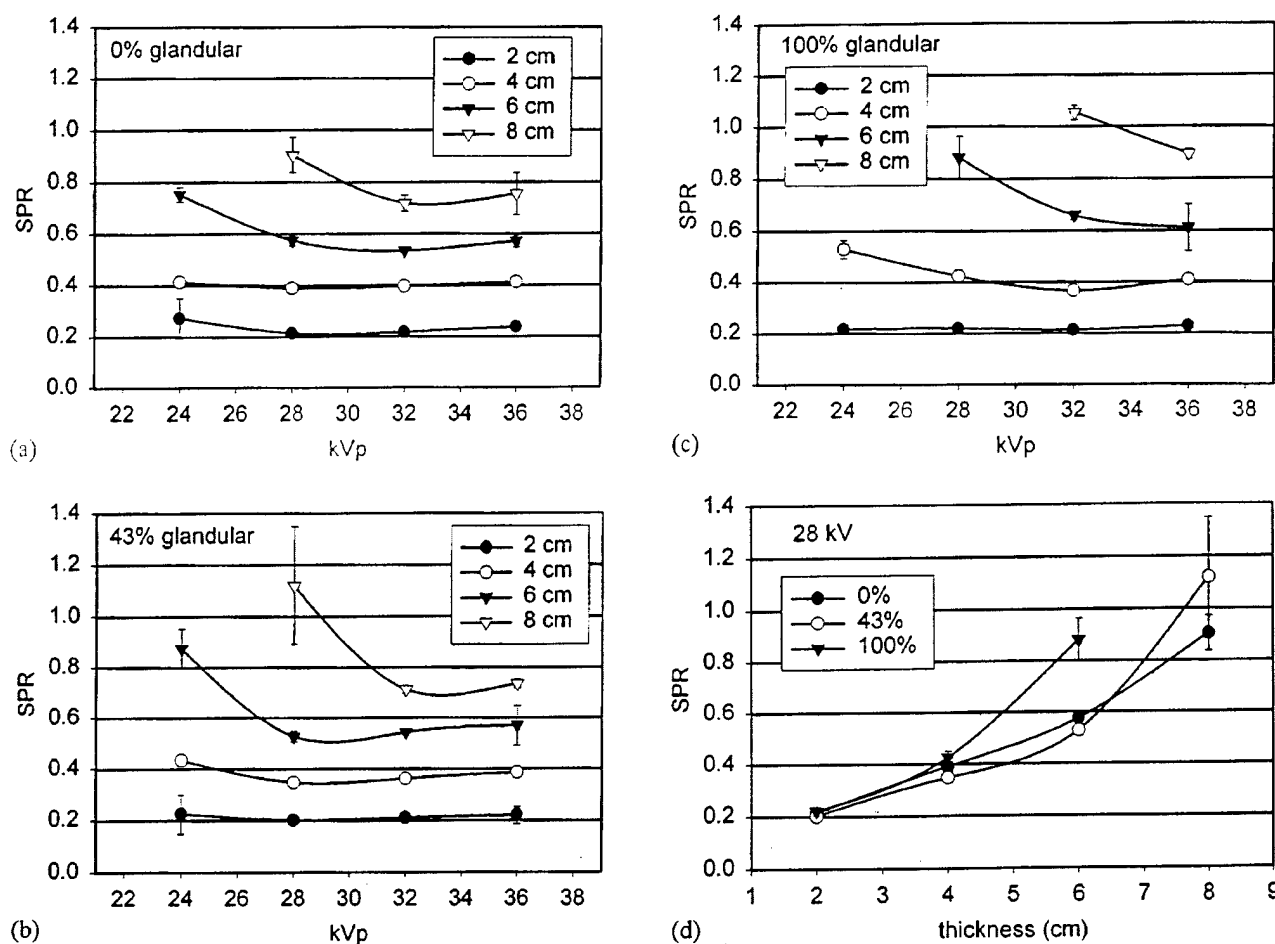


FIG. 6. Scatter-to-primary ratios (SPRs) for (a) 0% glandular breast phantoms, (b) 43% glandular breast, (c) 100% glandular breast phantoms, and (d) 0%, 43%, and 100% glandular breast phantoms imaged at 28 kVp.

clude the 24 kVp data point due to inadequate penetration/limited detector dynamic range. Inclusion of this point elevates the SPR to 0.63. The SPR shown for the 8 cm breast for the work of Dance and Day is for an energy of 25 keV. Overall, there is very good agreement (within 7%) between the two data sets ( $r^2=0.991$ , slope= $1.066 \pm 0.020$ ).

Scatter MTFs for selected exposure scenarios were measured. Figure 7(a) illustrates a representative example of the fit ESFs ( $r^2 > 0.992$  for all fits) (2 cm, 100% glandularity, 24 kVp). Figure 7(b) illustrates a representative LSF (2 cm, 100% glandularity, 24 kVp). Figure 8(a)–(c) shows representative scatter-only MTFs as functions of thickness, kVp, and glandularity, respectively. The spatial distribution of scatter was not strongly influenced by kVp or glandularity based on these data. However, there was a clear trend with thickness. The overall scatter MTF decreased for increasing breast thickness between 2 and 6 cm, after which there was essentially no effect, as witnessed by the 6 and 8 cm breast data plotted in Fig. 8(a). This effect is consistent with the effective range of the scatter being between 4 and 6 cm. The scatter generated in the incident 2 cm of the 8 cm breast probably did not reach the detector plane in any detectable quantity. If it did, it would have widened the scatter PSF purely due to geometry. Although the geometry differs by 90

degrees, this finding is also consistent with the work of Barnes and Brezovich, as there was little change in their reported SPRs for circular field sizes with radii greater than 5 cm.

For breast thicknesses less than the effective range of scatter, increasing thickness yields widening scatter spatial distributions. For thinner phantoms, scatter originating from the entrance layers (sub-volumes) of the scattering medium has the penetrability and geometry to reach the detector and be recorded. Increasing the thickness beyond some effective range of scatter results in self-attenuation of the scatter originating near the entrance surface of the phantom. After this point, increasing thickness has little effect on the scatter distribution. Theoretically, with *a priori* knowledge of the above MTFs, inverse filters could be constructed to counteract the effects of scatter degradation of low contrast detectability.

#### IV. FURTHER DISCUSSION

There are several advantages to the ESF methodology. The ESF method directly gives the spatial distribution of scatter, including small angle scatter effects. Although the spatial distribution of scatter may be inferred from the

TABLE II. SPRs for a 10 cm×10 cm field size.

		2		4		6		8	
kVp		SPR	st. dev.	SPR	st. dev.	SPR	st. dev.	SPR	st. dev.
Thickness (cm) (0% glandular)									
(a)	24	0.27±0.08		0.41±0.01		0.75±0.03		1.93±0.17	
	28	0.21±0.01		0.39±0.01		0.57±0.02		0.90±0.07	
	32	0.22±0.01		0.40±0.01		0.53±0.01		0.72±0.03	
	36	0.24±0.00		0.41±0.01		0.57±0.02		0.75±0.08	
Thickness (cm) (43% glandular)									
(b)	24	0.22±0.07		0.43±0.01		0.87±0.08		—±—	
	28	0.20±0.01		0.35±0.02		0.53±0.02		—±—	
	32	0.21±0.01		0.36±0.00		0.54±0.01		0.71±0.01	
	36	0.22±0.03		0.38±0.01		0.57±0.08		0.73±0.02	
Thickness (cm) (100% glandular)									
(c)	24	0.22±0.02		0.53±0.03		—±—		—±—	
	28	0.22±0.02		0.42±0.03		0.88±0.08		—±—	
	32	0.21±0.01		0.37±0.01		0.66±0.02		1.05±0.03	
	36	0.23±0.01		0.41±0.01		0.61±0.09		0.89±0.02	

method of Seibert *et al.* using the beam stop method, this is not a direct measurement<sup>26</sup> as an assumption about the functional form of the scatter spatial distribution is required. Furthermore, the ESF method does not require extrapolation in order to quantify SPR. The beam stop method does, and the extrapolation function, which is generally not well known, can have a significant impact on the calculated SPR. The ESF method has another advantage in that only two image acquisitions are needed for each SPR measurement. The beam stop method requires multiple acquisitions so that an adequate regression/extrapolation may be performed.

There are some disadvantages to the ESF method compared to the beam stop method. The ESF method requires that the resolution and primary plus scatter images be acquired under identical conditions with respect to the location and alignment of the edge. This is easily achieved, however, with a simple stand that allows immobilization of the edge with easy removal of the scattering material. The ESF method assumes the use of a spatially uniform scattering medium and in its current form does not allow for measure-

ment of SPRs for scattering media involving image structure (e.g., a bone embedded in soft tissue, breasts with "lumpy image texture," etc.). However, the SPRs and scatter spatial distributions did not vary widely for the studied 0%, 43%, and 100% glandular tissues when imaged under clinically realistic conditions. This suggests that regardless of the texture of the breast (i.e., lumpy, dense, fatty, etc.) the tissues contained therein may be thought of as a single homogeneous scattering medium.

Finally, the ESF method of measuring scatter radiation and its distribution has a potential clinical use in digital mammography. One of the advantages of digital mammography is the ability to process the digital image data such that the displayed images coincide with a specific visual perception task. In this scenario, the direct measurement of the spatial distribution of detected scatter resulting from the use of edge spread functions promotes the construction of filters that would enhance low frequencies thereby increasing image contrast and hence, increasing low-contrast detectability. Moreover, quantitative techniques such as dual energy mam-

TABLE III. SPR comparison with Barnes and Brezovich (a) and Dance and Day (b).

		Barnes and Brezovich		This work		
		Lucite thickness (cm)		100% glandular thickness		
		3	6	2	4	6
(a)	Field size (cm)					
	10.0	0.39	0.80	-	-	-
	10.0 square	-	-	0.21±0.01	0.37±0.01	0.66±0.02
	14.0	0.40	0.86	-	-	-
(b)	Thickness (cm)	Dance and Day		This work		
	2	0.25		0.21		
	4	0.42		0.38		
	6	0.59		0.55		
	8	0.75		0.72		

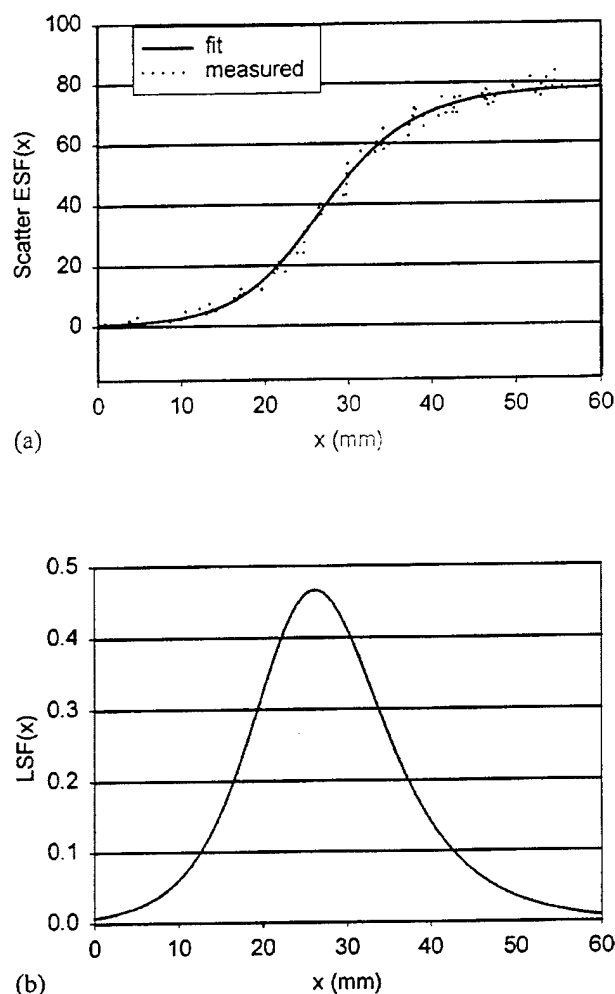


FIG. 7. (a) Measured and fit ( $r^2=0.993$ ) scatter ESFs for a 2 cm 100% glandular breast phantom, 24 kVp, and (b) the resulting scatter LSF calculated by numerically differentiating the fit scatter ESF.

mography may be improved if the low-frequency bias from scatter is removed. Since lesions of the breast are inherently low contrast in nature, this has substantial clinical implications. Furthermore, the data suggest a weak kVp dependence and a weak glandularity dependence for scatter, thus a family of filters constructed for different breast thicknesses should be reasonably robust for a range of clinical conditions. This family of filters could be derived from measurements such as these described in this manuscript. The field size and shape dependence of the filter could be readily solved numerically by way of convolving the measured scatter point spread function (measured all the way to 0 in the tails) with the breast image. In this scenario, one could use the image to estimate the object and hence, the SPR and spatial distribution of scatter, similar to that estimation used where the image power spectrum is used to estimate the object power spectrum for other filtering techniques such as Wiener filtering. The inverse filter that would be derived from this approach could then be applied to the image. Whether this approach is feasible or not is a subject that may require future research.

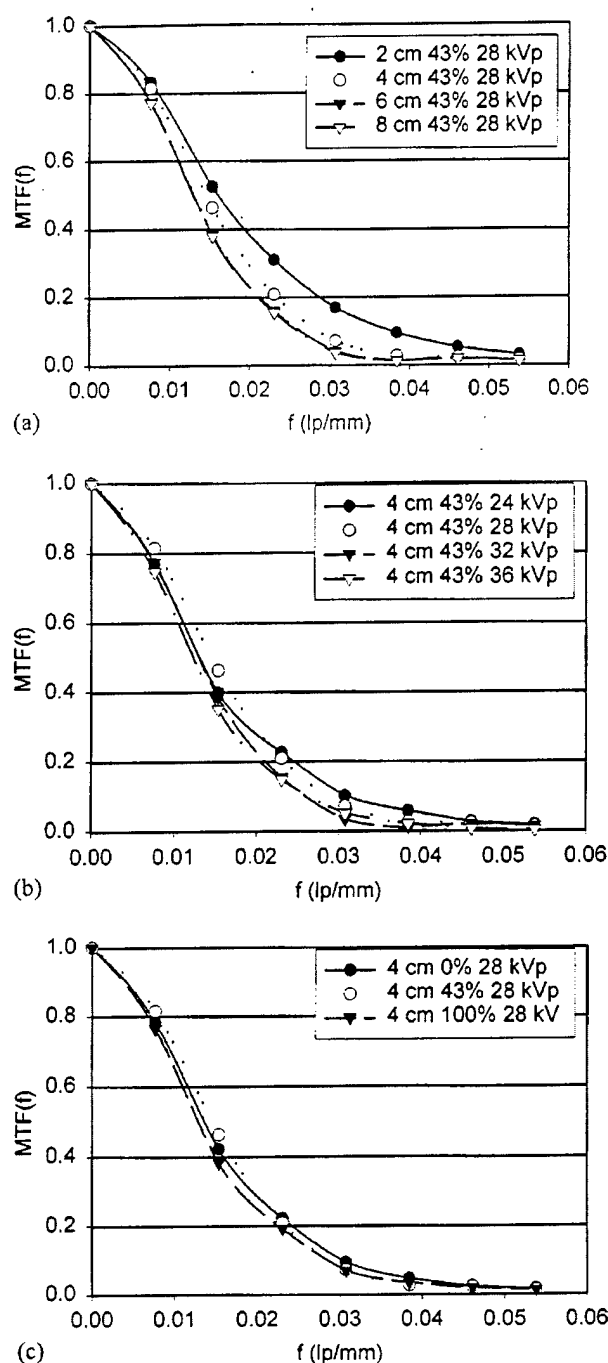


FIG. 8. Scatter MTFs demonstrating (a) thickness dependence, (b) kVp dependence, and (c) glandularity dependence.

## V. CONCLUSIONS

An experimental method of directly measuring the magnitude and spatial distribution of scattered radiation in relation to primary radiation has been presented. The method involves subtracting spatially aligned primary radiation and primary-plus-scatter radiation edge spread functions. The method shows good agreement with the more conventional beam stop technique of measuring scatter in relation to primary radiation. Demonstration of the method in measuring scatter-to-primary ratios under the conditions using current

image acquisition spectra and breast-mimicking phantoms suggest that SPRs in mammography may be lower than those reported in the early work of Barnes and Brezovich.

## ACKNOWLEDGMENTS

This research was supported in part by grants from the US Department of Defense Breast Cancer Research Program (DAMD17-94-4424 and DAMD17-98-8176), the California Breast Cancer Research Program (1RB-0912 and 2RB-0071), and the National Cancer Institute (R21-CA82077). The authors are grateful to Varian Imaging Products for the use of the flat panel imager used in this study.

<sup>a</sup>Address for correspondence: Virgil N. Cooper III, 4701 X Street, Sacramento, CA 95817, electronic mail: vncooper@ucdavis.edu

<sup>b</sup>Address for reprint requests: John M. Boone, 4701 X Street, Sacramento, CA 95817, electronic mail: jmboone@ucdavis.edu

- <sup>1</sup>G. T. Barnes, "Contrast and scatter in x-ray imaging," *Radiographics* **11**, 307-323 (1991).
- <sup>2</sup>R. H. Miettinen and O. A. Korhola, "The effect of scatter reduction on the signal-to-noise ratio in computed radiography," *Eur. J. Radiol.* **12**, 167-170 (1991).
- <sup>3</sup>J. W. Motz and C. E. Dick, "X-ray scatter background signals in transmission radiography," *Med. Phys.* **2**, 259-267 (1975).
- <sup>4</sup>B. Nielsen and G. Fagerberg, "Image quality in mammography with special reference to anti-scatter grids and the magnification technique," *Acta Radiol.: Diagn.* **27**, 467-479 (1986).
- <sup>5</sup>D. M. Tucker, M. Souto, and G. T. Barnes, "Scatter in computed radiography," *Radiology* **188**, 271-274 (1993).
- <sup>6</sup>M. J. Yaffe, "Direct digital mammography using a scanned-slot CCD imaging system," *Med. Prog. Technol.* **19**, 13-21 (1993).
- <sup>7</sup>G. T. Barnes and I. A. Brezovich, "The intensity of scattered radiation in mammography," *Radiology* **126**, 243-247 (1978).
- <sup>8</sup>D. R. Dance and G. J. Day, "The computation of scatter in mammography by Monte Carlo methods," *Phys. Med. Biol.* **29**, 237-247 (1984).
- <sup>9</sup>R. L. Egan, M. B. McSweeney, and P. Sprawls, "Grids in mammography," *Radiology* **146**, 359-362 (1983).
- <sup>10</sup>R. Fahrig, J. G. Mainprize, N. Robert, A. Rogers, and M. J. Yaffe, "Performance of glass fiber antiscatter devices at mammographic energies," *Med. Phys.* **21**, 1277-1282 (1994).
- <sup>11</sup>S. L. Fritz, C. H. J. Chang, and W. H. Livingston, "Scatter/primary ratios for x-ray spectra modified to enhance iodine contrast in screen-film mammography," *Med. Phys.* **10**, 866-870 (1983).
- <sup>12</sup>Z. Jing, W. Huda, and J. K. Walker, "Scattered radiation in scanning slot mammography," *Med. Phys.* **25**, 1111-1117 (1998).
- <sup>13</sup>E. P. Muntz, "Analysis of the significance of scattered radiation in reduced dose mammography, including magnification effects, scatter suppression, and focal spot and detector blurring," *Med. Phys.* **6**, 110-117 (1979).
- <sup>14</sup>K. H. Ng, R. J. Aus, L. A. DeWerd, and J. R. Vetter, "Entrance skin exposure and mean glandular dose: Effect of scatter and field gradient at mammography," *Radiology* **205**, 395-398 (1997).
- <sup>15</sup>P. S. Rezentes, A. de Almeida, and G. T. Barnes, "Mammography grid performance," *Radiology* **210**, 227-232 (1999).
- <sup>16</sup>G. T. Barnes, X. Wu, and A. J. Wagner, "Scanning slit mammography," *Med. Prog. Technol.* **19**, 7-12 (1993).
- <sup>17</sup>A. Krol, D. A. Bassano, C. C. Chamberlain, and S. C. Prasad, "Scatter reduction in mammography with air gap," *Med. Phys.* **23**, 1263-1270 (1996).
- <sup>18</sup>E. P. Muntz and W. W. Logan, "Focal spot size and scatter suppression in magnification mammography," *Am. J. Roentgenol.* **133**, 453-459 (1979).
- <sup>19</sup>M. V. Yester, G. T. Barnes, and M. A. King, "Experimental measurements of the scatter reduction obtained in mammography with a scanning multiple slit assembly," *Med. Phys.* **8**, 158-162 (1981).
- <sup>20</sup>H. Bernstein and E. P. Muntz, "Experimental verification of a technique for predicting scattered radiation transfer: Application to low photon energies," *Med. Phys.* **13**, 836-842 (1986).
- <sup>21</sup>C. E. Floyd, Jr., J. Y. Lo, H. G. Chotas, and C. E. Ravin, "Quantitative scatter measurement in digital radiography using a photostimulable phosphor imaging system," *Med. Phys.* **18**, 408-413 (1991).
- <sup>22</sup>C. E. Floyd, Jr., J. A. Baker, J. Y. Lo, and C. E. Ravin, "Posterior beam-stop method for scatter fraction measurement in digital radiography," *Invest. Radiol.* **27**, 119-123 (1992).
- <sup>23</sup>D. J. Klein, H.-P. Chan, E. P. Muntz, K. Doi, K. Lee, P. Chopelas, H. Bernstein, and J. Lee, "Experimental and theoretical energy and angular dependencies of scattered radiation in the mammography energy range," *Med. Phys.* **10**, 664-668 (1983).
- <sup>24</sup>J. A. Seibert, O. Nalcioğlu, and W. W. Roeck, "Characterization of the veiling glare PSF in x-ray image intensified fluoroscopy," *Med. Phys.* **11**, 172-179 (1984).
- <sup>25</sup>J. A. Seibert, O. Nalcioğlu, and W. W. Roeck, "Removal of image intensifier veiling glare by mathematical deconvolution techniques," *Med. Phys.* **12**, 281-288 (1985).
- <sup>26</sup>J. A. Seibert and J. M. Boone, "X-ray scatter removal by deconvolution," *Med. Phys.* **15**, 567-575 (1988).

# A lesion detectability simulation method for digital x-ray imaging<sup>a)</sup>

V. N. Cooper III, J. M. Boone, and J. A. Seibert

*Department of Radiology, University of California Davis, 4701 X Street, Sacramento, California 95831*

(Received 16 February 1999; accepted for publication 22 October 1999)

A simulation method is described in this work that aids in quantifying the upper limits of lesion detectability as a function of lesion size, lesion contrast, pixel size, and x-ray exposure for digital x-ray imaging systems. The method entails random lesion placement with subsequent simulated imaging on idealized x-ray detectors with no additive noise and 100% quantum detective efficiency. Lesions of different size and thickness were simulated. Mean (expectation) lesion signal-to-noise ratios (LSNRs) were calculated and receiver operating characteristic (ROC) curves were constructed based on LSNR ensembles. Mean (expectation) values of the areas under the ROC curves were calculated for lesions of varying size on pixel arrays of varying size at different exposures. Analyses were performed across several parameters, including lesion size, pixel size, and exposure levels representative of various areas of radiography. As expected, lesion detectability increased with lesion size, contrast, pixel size, and exposure. The model suggests that lesion detectability is strongly dependent on the relative alignment (phase) of the lesion with the pixel matrix for lesions on the order of the pixel size. © 2000 American Association of Physicists in Medicine. [S0094-2405(00)01801-0]

**Key words:** simulations, digital radiography, lesion detectability, signal-to-noise ratio (SNR), receiver operating characteristic curve (ROC)

## I. INTRODUCTION

Since the infancy of digital x-ray imaging, there has been much interest in pixel size requirements for adequate detection of lesions. Observational and experimental studies on lesion detectability as a function of pixel size abound in the literature.<sup>1-9</sup> Typically, these studies involve human detection of a specific type of lesion from images acquired with different pixel sizes. These studies then utilize some form of receiver operating characteristic curve (ROC)<sup>10</sup> analysis to demonstrate lesion detectability as a function of pixel size. The data in the literature are somewhat limited, however, concerning theoretical studies<sup>11</sup> that describe the mechanism of lesion detectability as a function of pixel size.

This paper demonstrates a simple simulation model that may be used to gain insight into the maximum possible lesion detectability as a function of several variables, in particular pixel size. The mean lesion signal-to-noise ratio (LSNR), integrated over the entire lesion, was calculated as a function of lesion size, lesion transmission, x-ray exposure level, and pixel size. Standardized receiver operating characteristic (ROC) curves were constructed for lesion-present and lesion-absent LSNRs. The areas under the generated ROC curves, the  $A_z$ 's, corresponded to the detectability of the lesions in their entirety and were used as the measures of lesion detectability.

## II. METHODS

### A. Phase-dependent signal

It is well understood that discrete detectors inherently are shift-variant. As a consequence of this shift-variant nature,

the position of the lesion with respect to the pixel matrix can have a significant impact on lesion detectability. Lesion signals at discrete phases of the pixel array were calculated for an ideal digital stationary<sup>12,13</sup> detection system employing varying pixel sizes with 100% active area. The system was modeled with no additive noise, 100% quantum detection efficiency, with an ideal point spread function (i.e.,  $\delta$ -function), and under scatter-free conditions. The number of quanta incident on a pixel is large in diagnostic radiology, and for large values of  $N$ , the Gaussian distribution is a good approximation to the Poisson distribution.<sup>15</sup> Thus the Gaussian distribution with the standard deviation,  $\sigma$ , equal to the square root of the mean,  $\mu$ , was used to simulate x-ray exposure to the detector. A Gaussian random number generator (GRNG) was used.<sup>14-16</sup>

Square lesions differing in size, composition, and thickness were considered. The lesions were assumed to be superimposed on homogeneous background tissue (i.e., see Fig. 1). The lesion under consideration was assumed to have the upper left-hand corner of its x-ray shadow fall on a reference pixel with pixel phase determined randomly with a uniform probability density function (PDF) for both detector plane ( $x$  and  $y$ ) dimensions. The outputs of a uniform random number generator (URNG), on the interval  $\{0,1\}$  were multiplied by the linear pixel dimensions and these values were used to define the translational phases,  $\Omega_x$  and  $\Omega_y$  (Fig. 2). This physically corresponded to the upper left-hand corner of the lesion having an equally likely chance of occurring at any location in the reference pixel. The locations of the other three corners of the lesion were determined by its dimensions.

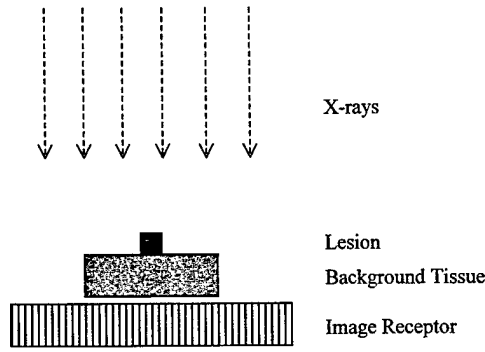


FIG. 1. The basic x-ray imaging geometry.

Following the placement of the lesion, x-ray exposure using a 50-keV monoenergetic beam was simulated and the total quanta at each pixel location were tallied. This was done for both lesion pixels and background pixels. The 50-keV monoenergetic beam is effectively equivalent to an 80-kVp beam with 2-mm Al filtration passing through 20 cm of tissue.<sup>17</sup> The exposure-dependent total number of quanta captured by the pixels corresponding to the lesion shadow,  $Q(X)_L$ , were summed over the total number of lesion pixels,  $M_L$

$$Q(X)_L = X \times \sum_{m=1}^{M_L} q_m, \quad (1)$$

where  $X$  is the radiation exposure expressed in mR.  $q_m$  is the number of quanta per mR captured by the  $m$ th pixel corresponding to the lesion shadow and is expressed as

$$q_m = q(\phi a^2, \sigma)_m \times (tf_m + (1 - f_m)), \quad (2)$$

where

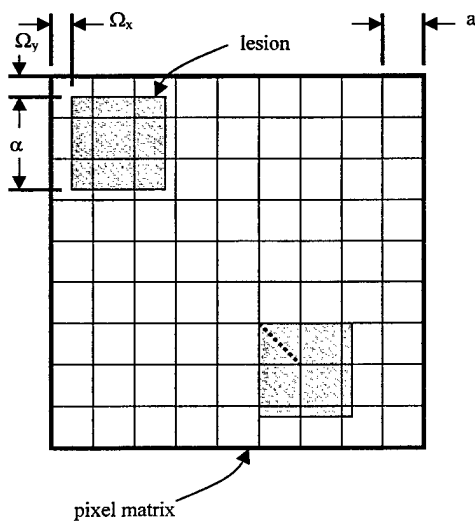


FIG. 2. A square lesion of side length  $\alpha$  is shifted  $\Omega_x$  and  $\Omega_y$  from the origin of a square pixel of side length  $a$ . In the lower right corner is a lesion starting in-phase with a pixel of the array. The dots represent calculation points for demonstrating the shift-dependent nature of the LSNR. For the expectation LSNR, the phase was randomly selected and LSNR calculated multiple times effectively averaging over the entire pixel.

$$\sigma = \sqrt{\phi a^2} \quad (3)$$

and where  $\phi$  is the x-ray photon fluence per unit exposure at 50 keV ( $260\,718\text{ mm}^{-2}\text{ mR}^{-1}$ );<sup>17</sup>  $a^2$  is the pixel area ( $a$  is the length of the pixel sides);  $\phi a^2$  is the mean number of x-ray photons incident on that pixel per unit exposure; and  $\sigma$  is the Poisson noise associated with that number.  $q(\phi a^2, \sigma)_m$  is the  $m$ th pixel realization of the unit-exposure x-ray quanta. The transmission associated with the lesion is given by  $t$ , and the fraction of the  $m$ th pixel covered by the lesion is represented by  $f_m$ .

Likewise, the background quanta,  $q_b$ , were summed over the total number of background pixels,  $M_B$ , to yield the total number of exposure dependent background quanta,  $Q_B$ :

$$Q(X)_B = X \times \sum_{b=1}^{M_B} q_b. \quad (4)$$

In general,  $M_B$  was significantly larger than  $M_L$  (typically by a factor of 100). Physically, this represents visualization and detection of a relatively small lesion in a relatively large background.

$Q_L$  was divided by  $M_L$  to yield the mean lesion signal per pixel,  $N(X)_L$ ,

$$N(X)_L = \frac{Q(X)_L}{M_L} \quad (5)$$

and likewise for the mean background signal per pixel,  $N(X)_B$ ,

$$N(X)_B = \frac{Q(X)_B}{M_B}. \quad (6)$$

## B. Lesion SNR (LSNR)

The mean lesion signal per pixel,  $N(X)_L$ , was subtracted from the mean background signal per pixel,  $N(X)_B$ ,

$$N(X)'_L = N(X)_B - N(X)_L, \quad (7)$$

where  $N(X)'_L$  is the background-corrected lesion signal. This signal,  $N(X)'_L$ , described on a per pixel basis, is summed over all  $M_L$  pixels corresponding to the lesion shadow. Physically, this represents the integration of signal over the entire lesion. The total lesion signal,  $S(X)_L$ , is given by:

$$S(X) = M_L \times N(X)'_L. \quad (8)$$

The variance in the integrated signal is physically represented as image noise and was quantified using standard error propagation techniques<sup>18</sup> for Eqs. (7) and (8), and was given as:

$$\sigma(X)^2 = M_L^2 \times (\sigma(X)_{N(X)_L}^2 + \sigma(X)_{N(X)_B}^2), \quad (9)$$

where  $\sigma(X)_{N(X)_B}$  is the background noise per pixel, and  $\sigma(X)_{N(X)_L}$  is the lesion noise per pixel. The background noise per pixel was calculated as the standard deviation of the background pixel quanta and was found not to depend on  $M_B$ , which is consistent with the ergodicity<sup>12,13</sup> principle

TABLE I. Lesion size, pixel size, and exposure parameter values.

Lesion size ( $\mu\text{m}$ )	Pixel size ( $\mu\text{m}$ )	Exposure (mR)
25	25	0.0010
50	50	0.0025
75	75	0.0050
100	100	0.0075
150	150	0.010
200	200	0.025
250	250	0.050
300	300	0.075
350	400	0.10
400	500	0.25
450		0.50
500		0.75
600		1.0
700		2.5
800		5.0
900		7.5
1000		10
1250		25
1500		50
2000		

often invoked in noise quantification in x-ray imaging. The lesion variance per pixel,  $\sigma(X)_{N(X)_L}^2$ , was calculated as

$$\sigma(X)_{N(X)_L}^2 = \frac{\sum_{m=1}^{M_L} (q_m - N(X)_B \times [f_m t + (1 - f_m)])^2}{(M_L - 1)}, \quad (10)$$

where the numerator is the summed variance in the x-ray quanta corrected for partial pixel coverage by the lesion. Lesion SNR (LSNR) was then calculated as

$$\text{LSNR} = \frac{S(X)}{\sigma(X)}. \quad (11)$$

### C. (LSNR)

Random lesion placement and subsequent SNR calculation were performed 100 times to yield an ensemble of LSNRs. The expectation (mean) lesion SNR,  $\langle \text{LSNR} \rangle$ , was calculated as the mean of the lesion SNRs in the ensemble:

$$\langle \text{LSNR} \rangle = \frac{1}{K} \sum_{k=1}^K \text{LSNR}_k, \quad (12)$$

where  $\text{LSNR}_k$  is the  $k$ th realization of LSNR and  $K$  is the number of realizations in the ensemble.

### D. $\langle A_Z \rangle$

Ensembles of 100 LSNRs were computed both for the cases of lesion present and lesion absent. The lesion absent ensemble was constructed by setting transmission,  $t$ , equal to 1.0. Both ensemble LSNR arrays were ordered and ROC analysis was performed. The area under the ROC curve,  $A_Z$ , was calculated via Reimann trapezoidal integration.<sup>16</sup>  $A_Z$  was calculated ten different times, each time from different LSNR data to yield an expectation (mean) value,  $\langle A_Z \rangle$ , and an error estimate

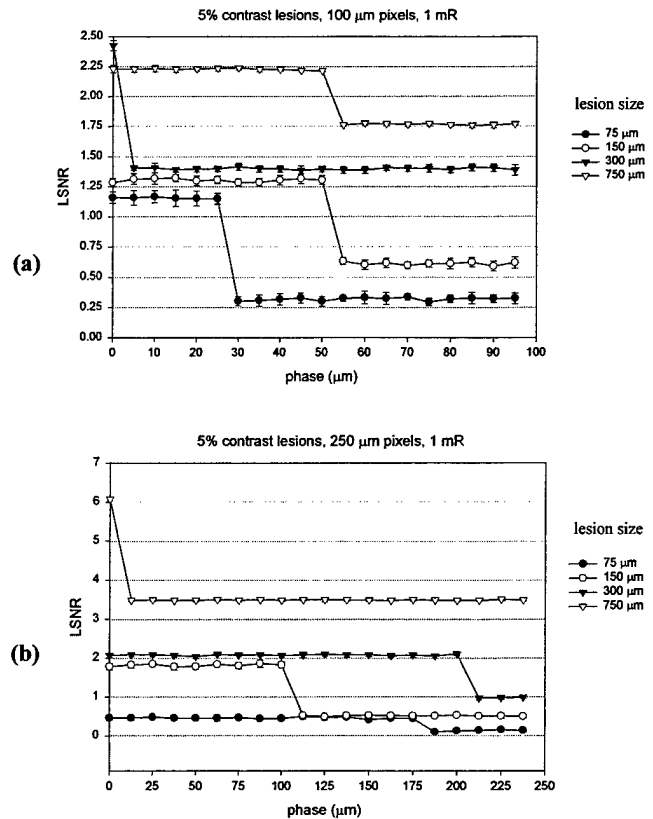


FIG. 3. The resulting shift-dependent ( $x$  and  $y$  simultaneous shifts) LSNR for a 95% transmitting lesion (constant) with (a) 1-mR exposure incident on an array with 100- $\mu\text{m}$  pixels and (b) 1-mR exposure on 250- $\mu\text{m}$  pixels. The error bars represent  $\pm \sigma$ .

$$\langle A_Z \rangle = \frac{1}{K} \sum_{k=1}^K (A_Z)_k, \quad (13)$$

where  $(A_Z)_k$  is the  $k$ th realization in a  $K$ -length ensemble of  $A_Z$ 's.  $\langle A_Z \rangle$  was used as the ultimate measure of lesion detectability.

### E. Parameter values

$\langle A_Z \rangle$  and  $\langle \text{LSNR} \rangle$  were calculated for several different combinations of lesion size, pixel size, and exposure level. Table I gives the values of all three parameters that were used in this study. Every permutation of the three parameters was simulated.

## III. RESULTS

### A. Phase-dependent SNR

To demonstrate the effects of pixel phase on LSNR, lesions of varying sizes were placed at discrete phases with  $\Omega_x = \Omega_y \equiv \Omega_{xy}$ . LSNR as a function of pixel phase was calculated 100 times at each phase and the results were averaged to yield a mean LSNR at a given phase. This process was repeated ten different times at each phase to yield the mean LSNRs with smaller uncertainty (i.e., the mean of the sample means). Figure 2 illustrates the discrete phases used for this demonstration. Figure 3(a) shows the phase-dependent LSNR of 75-, 150-, 300-, and 750- $\mu\text{m}$  lesions



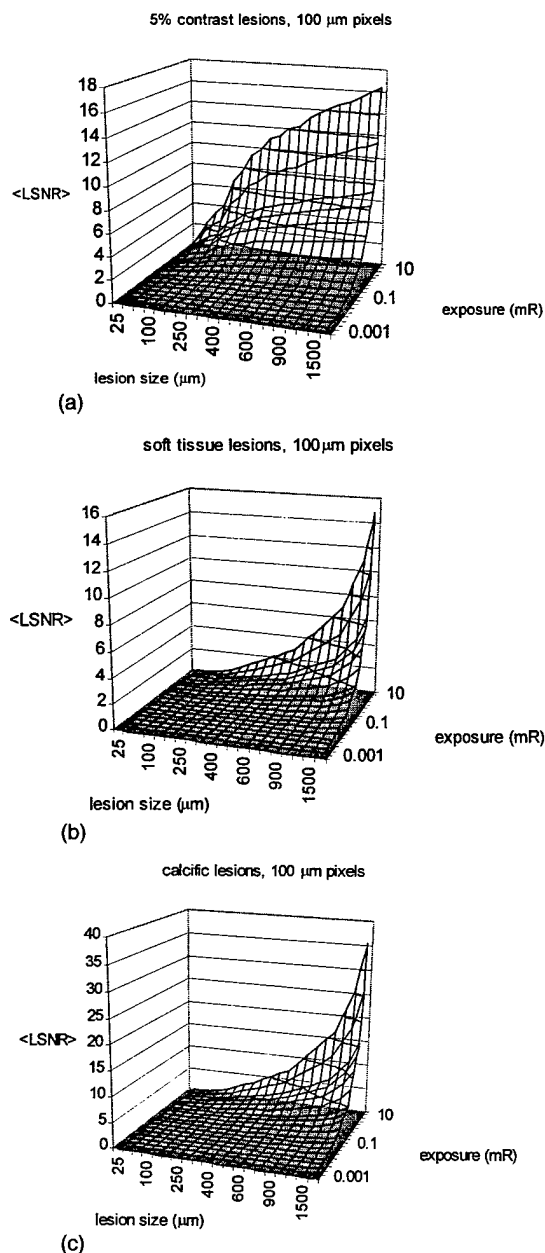


FIG. 4.  $\langle \text{LSNR} \rangle$  for (a) 5% constant contrast lesions and 100- $\mu\text{m}$  pixels, (b) cubic soft-tissue lesions and 100- $\mu\text{m}$  pixels, and (c) cubic calcific lesions and 100- $\mu\text{m}$  pixels.

with constant 5% contrast (95% transmission), 100- $\mu\text{m}$  pixels, and 1-mR exposure. As the lesion size increased beyond the pixel size, the phase effects on the LSNR decreased. Notice that the 75- $\mu\text{m}$  lesion, starting in-phase, had constant LSNR until the 25- $\mu\text{m}$  shift value. The SNR plummeted at this point as the lesion was shifted into four different pixels with each pixel having lowered signal and greater coefficients of variation (relative noise). Physically, in these partially covered pixels, this represents a degradation of contrast and hence signal, due to a partial area effect, similar to the degradation of contrast due to the partial volume effect in computed tomography.

The 150- $\mu\text{m}$  lesion had constant SNR until  $\Omega_{xy} = 50 \mu\text{m}$ , after which it covered nine pixels instead of four.

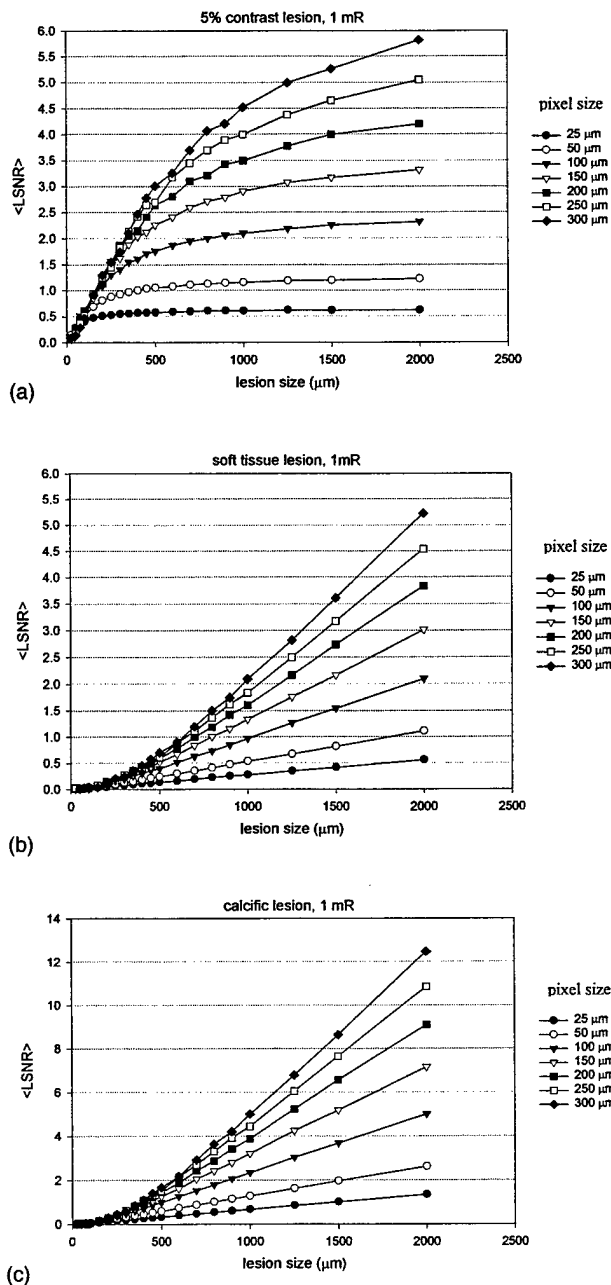


FIG. 5.  $\langle \text{LSNR} \rangle$  at 1 mR for different pixel sizes for (a) 5% contrast lesions, (b) cubic soft tissue lesions, and (c) cubic calcific lesions.

The 750- $\mu\text{m}$  lesion had a less-pronounced LSNR drop at  $\Omega_{xy} = 50 \mu\text{m}$ . The smaller drop was due to the fact that this large lesion had a greater proportion of pixels that were entirely covered by the lesion, somewhat mitigating the variational effects of edge pixels. Figure 3(b) shows the shift-dependent LSNR of 75-, 150-, 300-, and 750- $\mu\text{m}$  lesions with constant 5% contrast, 1 mR, and 250- $\mu\text{m}$  pixels. Similar phase-related behavior is exhibited. The effects of the larger pixel size are discussed in Sec. IV.

## B. $\langle \text{LSNR} \rangle$

$\langle \text{LSNR} \rangle$  was calculated for various pixel sizes, lesion sizes, and exposures with 100 realizations of LSNR com-

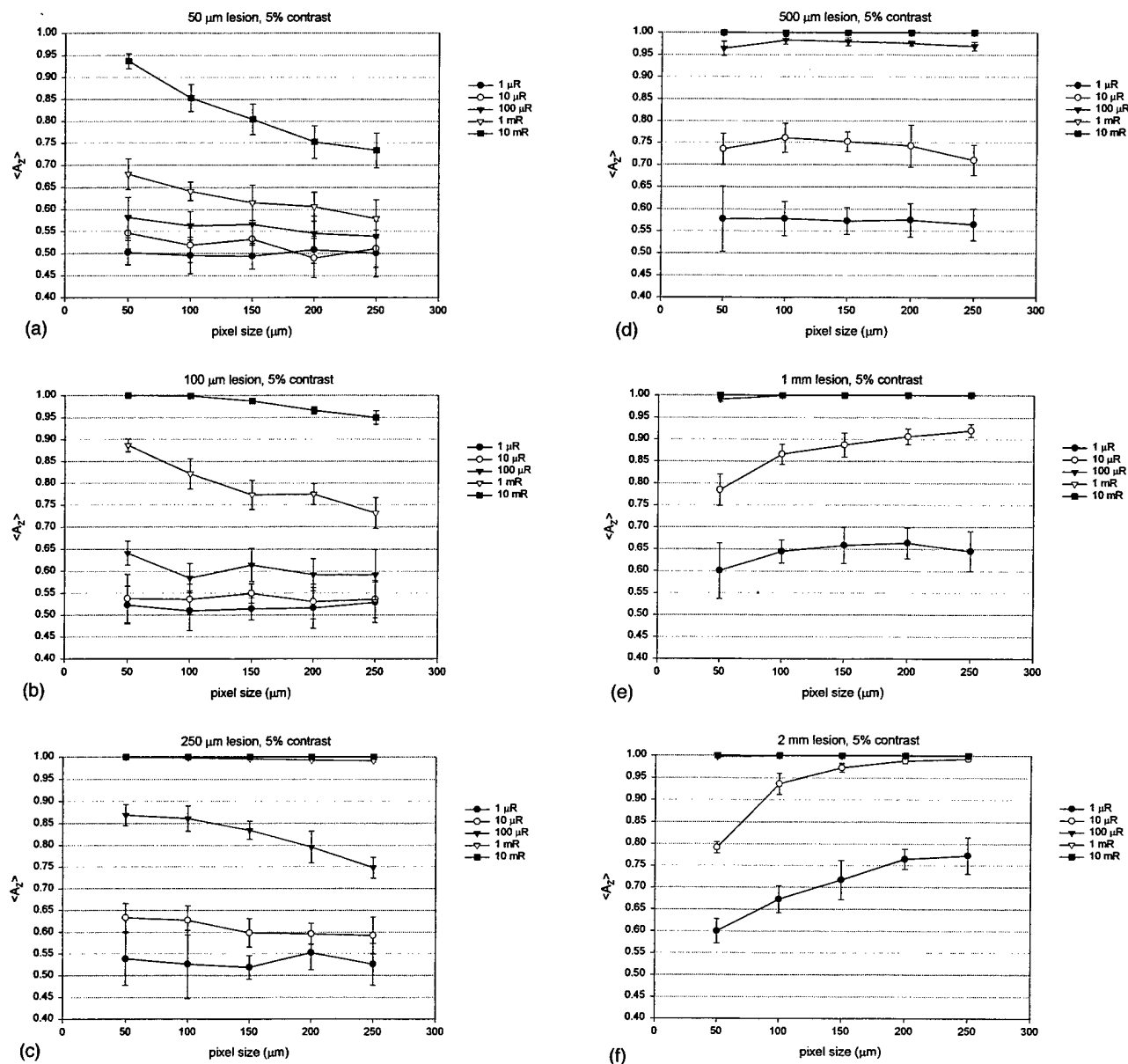


FIG. 6. 5% constant contrast lesion detectability,  $\langle A_Z \rangle$ , for (a) 50-μm lesions, (b) 100-μm lesions, (c) 250-μm lesions, (d) 500-μm lesions, (e) 1-mm lesions, and (f) 2-mm lesions. The error bars represent  $\pm \sigma$ . Note: In parts (d), (e), and (f), the data are obscured with  $\langle A_Z \rangle$  equal to 1.0 at all pixel sizes for the highest exposures.

puted for each combination of pixel size, lesion size, and exposure. Both constant contrast (transmission) lesions and cubic lesions (thickness=length=width) were considered. Transmission was given by  $e^{-\mu\alpha}$  for the cubic lesions where  $\alpha$  is the thickness and  $\mu$  is the linear attenuation coefficient at 50 keV and is equal to  $0.57 \text{ cm}^{-1}$  for bone and  $0.23 \text{ cm}^{-1}$  for soft tissue.<sup>19</sup> Figure 4(a) shows the surface plot of  $\langle \text{LSNR} \rangle$  of a lesion with constant 5% contrast for 100-μm pixels. Figure 4(b) shows the surface plot of  $\langle \text{LSNR} \rangle$  for cubic soft tissue lesions for 100-μm pixels. Figure 4(c) shows the surface plot of  $\langle \text{LSNR} \rangle$  for cubic calcific lesions for 100-μm pixels. Figure 5(a), (b), and (c) illustrates  $\langle \text{LSNR} \rangle$  at 1 mR as a function of lesion size for a series of

pixel sizes, for 5% contrast lesions, soft tissue lesions, and calcific lesions, respectively. Error bars were not included in these figures for clarity.

### C. $\langle A_Z \rangle$

$\langle A_Z \rangle$  was calculated from an ensemble of 10  $A_Z$  realizations each based on 100 realizations each of lesion and no-lesion LSNRs. Figure 6(a)–(f) shows  $\langle A_Z \rangle$  for 5% contrast lesions; Fig. 7(a)–(f) shows  $\langle A_Z \rangle$  for cubic soft tissue lesions, and Fig. 8(a)–(f) shows  $\langle A_Z \rangle$  for cubic calcific lesions. To clarify the interesting behavior of  $\langle A_Z \rangle$  for lesion sizes on the order of pixel sizes,  $\langle \text{LSNR} \rangle$  data at different exposures

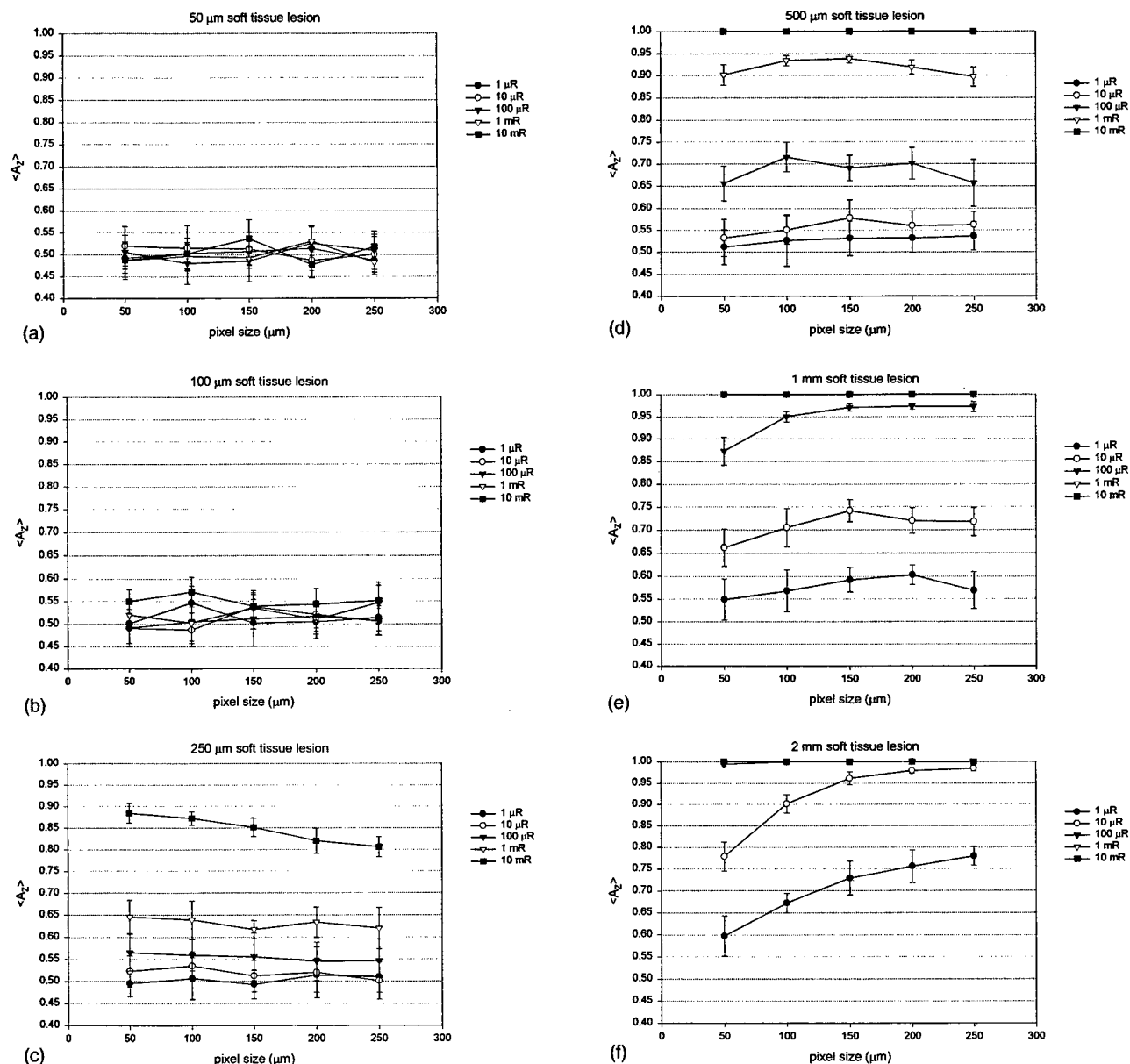


FIG. 7. Soft tissue lesion detectability,  $\langle A_Z \rangle$ , for (a) 50-μm cubic lesions, (b) 100-μm cubic lesions, (c) 250-μm cubic lesions, (d) 500-μm cubic lesions, (e) 1-mm cubic lesions, and (f) 2-mm cubic lesions. The error bars represent  $\pm \sigma$ . Note: In parts (e) and (f), the data are obscured with  $\langle A_Z \rangle$  equal to 1.0 at all pixel sizes for the highest exposures.

for given lesion sizes with 5% contrast were replotted against pixel size. Figure 9(a)–(g) shows  $\langle \text{LSNR} \rangle$  for 5% contrast lesions.

#### IV. DISCUSSION

A probabilistic model was presented whereby lesion SNR was calculated as a function of phase, lesion size, exposure, and pixel size. ROC methodology was utilized to quantify lesion detectability. As expected, lesion detectability mostly increased with increasing exposure, lesion size, and pixel size as a consequence of increased x-ray quanta involved in image formation. However, due to phase effects, there were some departures from expected behavior.

How a lesion aligns with the pixel matrix is a purely random phenomenon; however, detectability is strongly in-

fluenced by this pixel phase parameter as seen in Fig. 3. Consequently, the phase parameter can cause decreases in the  $\langle \text{LSNR} \rangle$  due to the partial area effect (i.e., a degradation of contrast and hence, signal). Thus the error bars in the graphs of  $\langle \text{LSNR} \rangle$  [Fig. 9(a)–(g)] are not entirely a function of x-ray quantum statistics, but include phase variability from partially covered pixels as well. The extent of this variability is strongly dependent on lesion size relative to pixel size. For large lesions covering many pixels, the abundance of pixels entirely covered by the lesion somewhat mitigates this phase effect. Conversely, for lesions covering a few pixels, the partially covered pixels make up a larger fraction of the total number of lesion pixels, hence, there is more LSNR variability, and  $\langle A_Z \rangle$  is reduced accordingly. Consider Figs. 6(c) and 9(c) and 9(g). A 5% contrast 250-μm lesion imaged

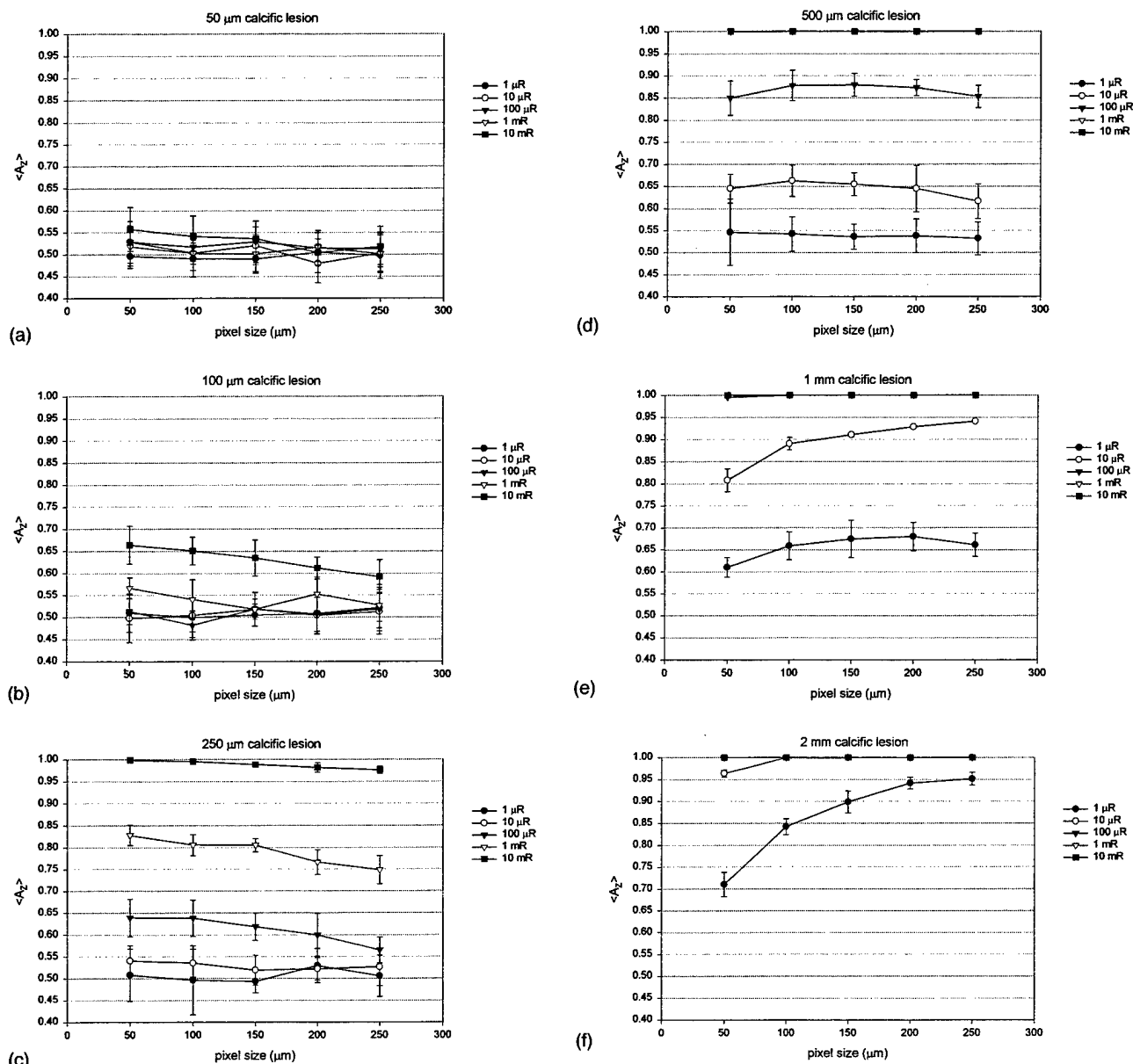


FIG. 8. Calcific lesion detectability,  $\langle A_Z \rangle$ , for (a) 50- $\mu\text{m}$  cubic lesions, (b) 100- $\mu\text{m}$  cubic lesions, (c) 250- $\mu\text{m}$  cubic lesions, (d) 500- $\mu\text{m}$  cubic lesions, (e) 1-mm cubic lesions, and (f) 2-mm cubic lesions. The error bars represent  $\pm\sigma$ . Note: In parts (d), (e), and (f), the data are obscured with  $\langle A_Z \rangle$  equal to 1.0 at all pixel sizes for the highest exposures.

at 100  $\mu\text{R}$  shows small error bars at 50- $\mu\text{m}$  pixel size and progressively larger ones as pixel size is increased. For the 50- $\mu\text{m}$  pixel size, the 250- $\mu\text{m}$  lesion involves at least 25 pixels, and the majority of those pixels are inner or totally covered pixels. This large number of inner pixels mitigates the effects that the edge pixels have on the LSNR variability. On the other hand, the larger pixel sizes image the lesion with fewer pixels. Thus these edge pixels play larger roles in determining LSNR variability. Hence, the variability increases with pixel size, due to phase effects. Since  $\langle A_Z \rangle$  is based on these LSNR realizations, and these LSNR realizations are not very different from the no-lesion case of zero SNR plus or minus some standard deviation, the LSNR variability plays a crucial role in determining  $\langle A_Z \rangle$ . The increasing LSNR variability at increasing pixel sizes yields decreas-

ing lesion detectability. In Fig. 9(c), that same 5% contrast 250- $\mu\text{m}$  lesion imaged at 10 mR yields even larger variability as witnessed by the size of the error bars, yet  $\langle A_Z \rangle$  remains at 1 when pixel size is increased. In this case, the LSNR variability increases compared to the 100- $\mu\text{R}$  data due to the increased number of quanta used in the 10-mR data. The higher photon fluence magnifies the variability due to phase or edge pixel effects in an absolute sense. However, this higher fluence reduces this variability relative to the mean LSNR,  $\langle \text{LSNR} \rangle$ , by proportionately elevating  $\langle \text{LSNR} \rangle$  more. That is, variability increases with increasing exposure in an absolute sense, but variability decreases in a relative sense to the mean signal. So, variability alone does not determine  $\langle A_Z \rangle$ ; variability relative to the mean LSNR,  $\langle \text{LSNR} \rangle$ , must be considered. In this case, although the in-

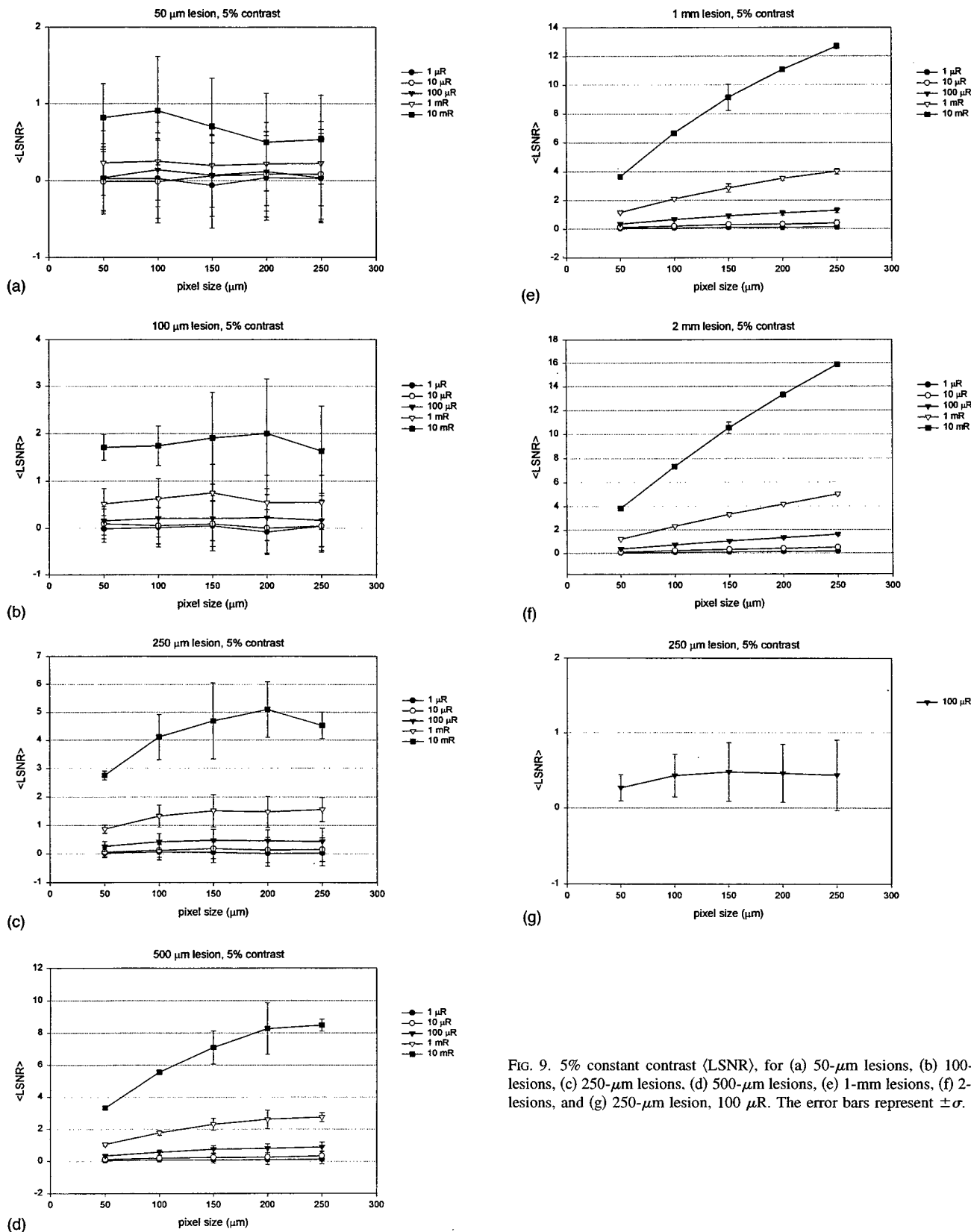


FIG. 9. 5% constant contrast  $\langle \text{LSNR} \rangle$ , for (a) 50- $\mu\text{m}$  lesions, (b) 100- $\mu\text{m}$  lesions, (c) 250- $\mu\text{m}$  lesions, (d) 500- $\mu\text{m}$  lesions, (e) 1-mm lesions, (f) 2-mm lesions, and (g) 250- $\mu\text{m}$  lesion, 100  $\mu\text{R}$ . The error bars represent  $\pm\sigma$ .

creased quanta of the 10-mR image yielded increased LSNR variability, the LSNR estimates are elevated due to the increased quanta, and are far above the no-lesion case of zero SNR plus or minus some standard deviation for every stud-

ied pixel size. Hence,  $\langle A_Z \rangle$  remains at 1 for each studied pixel size. Consider Figs. 6(f) and 9(f) and the 2-mm lesions.  $\langle \text{LSNR} \rangle$  increases as expected with increasing pixel size and has little variability. The very low LSNR variability in this

case is due to the fact that the 2-mm lesion is much larger than the pixel sizes. Hence, there are numerous fully covered pixels to mitigate the variational effects of edge pixels. Since the larger pixels collect more quanta per pixel, lesion detectability increases with increasing pixel size.

In this work, both fixed contrast and cubic lesions were considered. Although, the fixed contrast scenario aids in separating the effects of lesion contrast and areal coverage on lesion detectability, in reality, as lesions increase in area, they generally increase in thickness. Hence, the cubic lesion scenario is physically more appealing. The effects of increasing contrast with increasing lesion areal dimension may be inferred by comparing Figs. 6–8. Lesion detectability is shown to rapidly increase in the case of calcific lesions where contrast rapidly increased (Fig. 8). Although less pronounced, the same behavior was exhibited by the soft tissue lesion detectability (Fig. 7).

The preceding discussion is based on an ideal detector under ideal conditions. As such, this work represents the upper limits in lesion detectability. However, there are some potential modifications that may be made to the methodology for a more clinically representative simulation. Monte Carlo techniques in the study of scatter and dose distribution abound in the literature. While in this simulation study, the quanta incident on a pixel were studied in aggregate, it is not inconceivable to study the quanta, one photon at a time and trace the individual photon histories through scattering in the tissue and deposition of energy in the detector. This would allow study of lesion detectability in the presence of degraded contrast and hence, signal, due to photon scattering. In addition, electronic (additive) noise may be incorporated by way of a separate random number generator that simulates the dark electronic signal distribution.

## ACKNOWLEDGMENTS

This work was supported in part by grants from the U.S. Department of Defense Breast Cancer Research Program (DAMD17-94-4424 and DAMD17-98-8176), the California Breast Cancer Research Program (1RB-0912 and 2RB-0071), and the National Cancer Institute (R21-CA82077). The first author is grateful to Dr. Claire Pellot-Barakat, for useful discussions on the topics of image noise and general image science, and Ms. Renee Rees for useful discussions of probabilistic models.

<sup>a)</sup>This work was supported by the U.S. Department of Defense Breast Cancer Research Program (DAMD17-94-4424 and DAMD17-98-8176), the

California Breast Cancer Research Program (1RE-0912 and 2RB-0071) and the National Cancer Institute (R21-CA82077).

- <sup>1</sup>H. P. Chan, C. J. Vyborny, H. MacMahon, C. E. Metz, K. Doi, and E. A. Sickles, "Digital mammography. ROC studies of the effects of pixel size and unsharp-mask filtering on the detection of subtle microcalcifications," *Invest. Radiol.* **22**, 581–589 (1987).
- <sup>2</sup>H. P. Chan, L. T. Niklason, D. M. Ikeda, K. L. Lam, and D. D. Adler, "Digitization requirements in mammography: Effects on computer-aided detection of microcalcifications," *Med. Phys.* **21**, 1203–1211 (1994).
- <sup>3</sup>J. Ikezoe, S. Kido, N. Takeuchi, H. Kondoh, J. Arisawa, and T. Kozuka, "Image quality of digital chest radiography: evaluation of subtle interstitial lung abnormalities (preliminary study)," *Comput. Methods Programs Biomed.* **43**, 107–114 (1994).
- <sup>4</sup>J. Ikezoe, N. Kohno, S. Kido, N. Takeuchi, T. Johkoh, J. Arisawa, and T. Kozuka, "Interpretation of subtle interstitial chest abnormalities: Conventional radiography versus high-resolution storage-phosphor radiography—A preliminary study," *J. Digit. Imaging* **8**, 31–36 (1995).
- <sup>5</sup>A. Jonsson, S. Laurin, G. Karner, K. Herrlin, P. Hochbergs, K. Jonsson, O. Rudling, S. Sandstrom, M. Sloth, G. Svahn, and H. Pettersson, "Spatial resolution requirements in digital radiography of scaphoid fractures. An ROC analysis," *Acta Radiol.* **37**, 555–560 (1996).
- <sup>6</sup>H. MacMahon, C. J. Vyborny, C. E. Metz, K. Doi, V. Sabeti, and S. L. Solomon, "Digital radiography of subtle pulmonary abnormalities: A ROC study of the effect of pixel size on observer performance," *Radiology* **158**, 21–26 (1986).
- <sup>7</sup>M. D. Murphey, "Digital skeletal radiography: Spatial resolution requirements for detection of subperiosteal resorption," *AJR, Am. J. Roentgenol.* **152**, 541–546 (1989).
- <sup>8</sup>M. D. Murphey, J. M. Bramble, L. T. Cook, N. L. Martin, and S. J. Dwyer, "Nondisplaced fractures: spatial resolution requirements for detection with digital skeletal imaging," *Radiology* **174**, 865–870 (1990).
- <sup>9</sup>M. K. Shrout, J. Weaver, B. J. Potter, and C. F. Hildebolt, "Spatial resolution and angular alignment tolerance in radiometric analysis of alveolar bone change," *J. Periodontol.* **67**, 41–45 (1996).
- <sup>10</sup>C. E. Metz, "ROC methodology in radiologic imaging," *Invest. Radiol.* **21**, 720–733 (1986).
- <sup>11</sup>M. L. Giger and K. Doi, "Investigation of basic imaging properties in digital radiography. 3. Effect of pixel size on SNR and threshold contrast," *Med. Phys.* **12**, 201–208 (1985).
- <sup>12</sup>J. C. Dainty and R. Shaw, *Image Science* (Academic, London, 1974).
- <sup>13</sup>M. J. Yaffe and R. M. Nishikawa, "X-ray imaging concepts: Noise, SNR and DQE," in *Specification, Acceptance Testing and Quality Control of Diagnostic X-ray Imaging Equipment*, edited by J. A. Seibert, G. T. Barnes, and R. G. Gould (American Institute of Physics, Woodbury, NY, 1994), pp. 109–144.
- <sup>14</sup>R. L. Morin, *Monte Carlo Simulation in the Radiological Sciences* (CRC Press, Boca Raton, FL, 1988), pp. 14–52.
- <sup>15</sup>G. E. P. Box and M. E. Muller, "A note on the generation of random normal deviates," *Ann. Math. Stat.* **29**, 610–611 (1958).
- <sup>16</sup>W. H. Press, S. A. Teukolsky, W. T. Vetterling, and B. P. Flannery, *Numerical Recipes in C: The Art of Scientific Computing*, 2nd ed. (Cambridge University Press, New York, 1992).
- <sup>17</sup>J. M. Boone, "Spectral modeling and compilation of quantum fluence in radiography and mammography," *Proc. SPIE* **3336**, 592–601 (1998).
- <sup>18</sup>P. R. Bevington and D. K. Robinson, *Data Reduction and Error Analysis for the Physical Sciences*, 2nd ed. (McGraw-Hill, New York, 1983).
- <sup>19</sup>H. E. Johns and J. R. Cunningham, *The Physics of Radiology*, 4th ed. (Charles C. Thomas, Springfield, IL, 1983).



# A Monte Carlo study of x-ray fluorescence in x-ray detectors

John M. Boone<sup>a)</sup> and J. Anthony Seibert

*Department of Radiology, University of California, Davis, UC Davis Medical Center, Sacramento, California 95817*

John M. Sabol

*Sterling Diagnostic Imaging, Brevard, North Carolina 28712*

Melvin Tecotzky

*Department of Radiology, Thomas Jefferson University, Philadelphia, Pennsylvania 19107*

(Received 5 November 1998; accepted for publication 25 March 1999)

Advances in digital x-ray detector systems have led to a renewed interest in the performance of x-ray phosphors and other detector materials. Indirect flat panel x-ray detector and charged coupled device (CCD) systems require a more technologically challenging geometry, whereby the x-ray beam is incident on the front side of the scintillator, and the light produced must diffuse to the back surface of the screen to reach the photoreceptor. Direct detector systems based on selenium have also enjoyed a growing interest, both commercially and academically. Monte Carlo simulation techniques were used to study the x-ray scattering (Rayleigh and Compton) and the more prevalent x-ray fluorescence properties of seven different x-ray detector materials,  $\text{Gd}_2\text{O}_2\text{S}$ , CsI, Se, BaFBr,  $\text{YTaO}_4$ ,  $\text{CaWO}_4$ , and  $\text{ThO}_2$ . The redistribution of x-ray energy, back towards the x-ray source, in a forward direction through the detector, and lateral reabsorption in the detector was computed under monoenergetic conditions (1 keV to 130 keV by 1 keV intervals) with five detector thicknesses, 30, 60, 90, 120, and 150  $\text{mg}/\text{cm}^2$  (Se was studied from 30 to 1000  $\text{mg}/\text{cm}^2$ ). The radial distribution (related to the point spread function) of reabsorbed x-ray energy was also determined. Representative results are as follows: At 55 keV, more (31.3%) of the incident x-ray energy escaped from a 90  $\text{mg}/\text{cm}^2$   $\text{Gd}_2\text{O}_2\text{S}$  detector than was absorbed (27.9%). Approximately 1% of the total absorbed energy was reabsorbed greater than 0.5 mm from the primary interaction, for 90  $\text{mg}/\text{cm}^2$  CsI exposed at 100 kVp. The ratio of reabsorbed secondary (fluorescence+scatter) radiation to the primary radiation absorbed in the detectors (90  $\text{mg}/\text{cm}^2$ ) ( $S/P$ ) was determined as 10%, 16%, 2%, 12%, 3%, 3%, and 0.3% for a 100 kVp tungsten anode x-ray spectrum, for the  $\text{Gd}_2\text{O}_2\text{S}$ , CsI, Se, BaFBr,  $\text{YTaO}_4$ ,  $\text{CaWO}_4$ , and  $\text{ThO}_2$  detectors, respectively. The results indicate significant x-ray fluorescent escape and reabsorption in common x-ray detectors. These findings suggest that x-ray fluorescent radiation redistribution should be considered in the design of digital x-ray imaging systems. © 1999 American Association of Physicists in Medicine. [S0094-2405(99)01006-8]

**Key words:** X-ray fluorescence, K-edge, Monte Carlo, digital image detectors, imaging science

## I. INTRODUCTION

For general diagnostic radiology, screen film systems employ dual-emulsion, dual-screen cassettes. In this design, the x-ray phosphor is essentially sliced into two halves, with the photoreceptor (the dual-emulsion film) sandwiched between the two x-ray phosphor screens. This is possible because x rays pass efficiently through the film base and emulsion. Positioning the photoreceptor in the middle of the intensifying screen layers reduces the distance in the screen that light must diffuse through to reach the film emulsion, improving spatial resolution. With digital radiographic systems based on amorphous silicon thin film transistor technology ( $\alpha$ -Si TFT),<sup>1,2</sup> charge coupled devices (CCDs),<sup>3,4</sup> or complementary metal oxide semiconductors (CMOS),<sup>5</sup> however, only a single x-ray screen can be used because these photodetectors are radio-opaque. With such systems, the x rays are incident upon the x-ray phosphor from the front, while the photoreceptor collects the light behind the screen. Thus the light emitted by the screen, which is produced preferentially near

the front of the screen, must diffuse through the thickness of the intensifying screen in this geometry. Because of this important difference in x-ray detection geometry, the search for x-ray phosphors for digital systems has led to more exotic detector materials for the digital radiographic application. Because of differences in applications between digital x-ray detectors and screen/film cassettes, the constraints of cost, durability, and high-end spatial resolution are quite different, and this has also fueled a renewed investigation of x-ray detectors for digital imaging.

The K-edge of an x-ray detector material is an important consideration in the detector performance for a given diagnostic imaging task. While it is widely assumed that it is desirable to have the majority of the x-ray photons incident upon the detector with energies above the K-edge, to improve quantum detection efficiency, the re-emission of characteristic radiation (x-ray fluorescence) will reduce the overall absorption efficiency. Worse, when x-ray fluorescence is reabsorbed by the detector adjacent to the primary x-ray in-



teraction, a loss of spatial resolution and an increase in image noise may occur. X-ray fluorescence and related energy absorption phenomena occurring in imaging detectors has been investigated by others.<sup>6-9</sup> Previous studies primarily focused on screen-film radiography. In this study, Monte Carlo procedures were used in an analysis of several different possible candidates for x-ray detectors:  $\text{Gd}_2\text{O}_2\text{S}$ , CsI, Se,  $\text{YTaO}_4$ ,  $\text{CaWO}_4$ , and  $\text{ThO}_2$ .

This study focused solely on the Monte Carlo transport of x-ray photons, however, the transport of optical photons in an x-ray scintillation detector (intensifying screen) is also an important consideration and certainly plays the predominant role in broadening the point spread function of the screen. Whereas x-ray intensifying screens are indirect detectors in which optical energy ultimately stimulates the photoreceptor, direct detectors such as Se do not make use of intermediary optical photons. Rather, the detector reads out the charge (electrons) liberated in the detector by direct x-ray interaction. This study was designed in part to compare the x-ray scatter and photoelectric reabsorption contribution to the point spread function in both direct (selenium) and indirect x-ray detectors.

## II. METHODS AND MATERIALS

Monte Carlo simulations were employed to study the x-ray absorption, scatter, and x-ray fluorescent reabsorption in a direct x-ray detector material (selenium), a photostimulable phosphor (BaFBr) used in "computed radiography" (CR), and in various x-ray scintillators. The conventional x-ray phosphors studied were  $\text{Gd}_2\text{O}_2\text{S}$ ,  $\text{YTaO}_4$ , and  $\text{CaWO}_4$ . We have an interest in the potential of  $\text{ThO}_2$  as an x-ray phosphor, and therefore included it in this study. Many prototype  $\alpha$ -Si TFT systems currently make use of CsI as a scintillator, and hence it is included here as well.

The TART 98 Monte Carlo simulation package was used to study the x-ray transport dynamics in this study. TART is a completely verified Monte Carlo set of programs which has a development history spanning several decades. The current generation of this code was developed at Lawrence Livermore National Laboratory,<sup>10</sup> and distributed on CD ROM by Oakridge National Laboratory.<sup>11</sup> The Monte Carlo code uses a script language which allows the user to define relatively complex geometries, and to specify x-ray source properties, emission characteristics, and arbitrary detector chemical compositions and densities. The newest version of TART, TART 98-2, was provided by its developer<sup>12</sup> and was used for the Monte Carlo studies reported here.

The detector under study was partitioned into a series of annuli of increasing radius encompassing a center circle [Fig. 1(A)]. X-ray photons were normally incident upon the center of the circle at a point. The spacing of the concentric annuli was 0.100 mm extending out to 4.5 mm. For each detector composition and thickness,  $10^6$  x-ray photons were input to the detector at each x-ray energy. X-ray energies ranging from 1 keV to 130 keV by 1 keV increments were studied. For each composition, phosphor thickness, and x-ray energy, two Monte Carlo runs were initiated each with  $10^6$  photons.

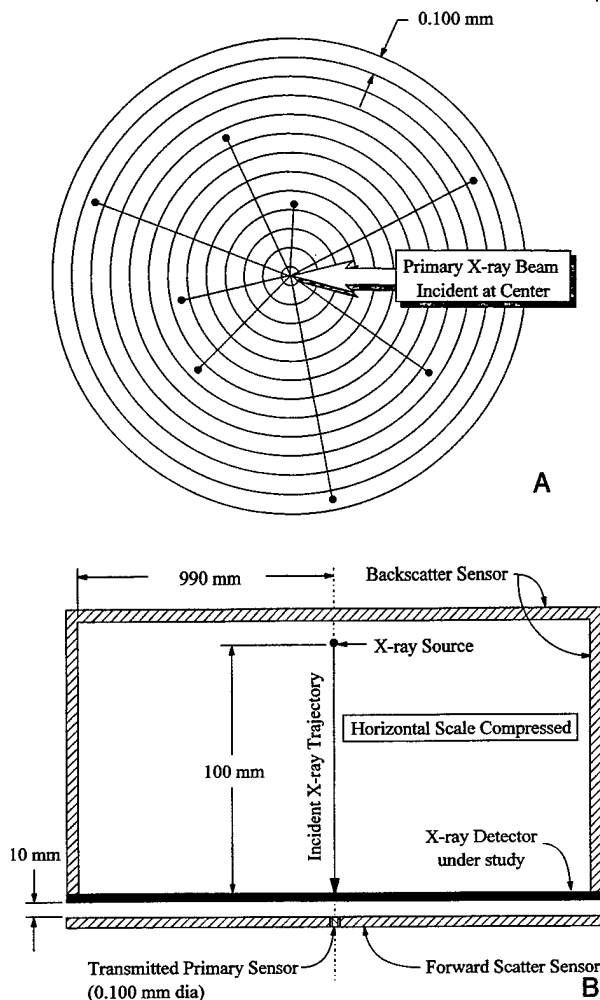


FIG. 1. (A) The geometry of the Monte Carlo simulation is illustrated. The x-ray beam was normally incident upon the x-ray detector under study. For the purposes of the Monte Carlo evaluation, "sensors" were positioned as illustrated in order to measure the backscattered energy, the transmitted primary radiation, and the forward scatter generated in the x-ray detector. (B) The x-ray detector was subdivided into a series of annular regions, each differing in radius by 0.100 mm. The energy absorbed in the center circle and in each annulus was tallied independently in the Monte Carlo simulations.

The first Monte Carlo run ("tracking ON mode") tracked all scattering (Rayleigh and Compton) and x-ray characteristic photons through the detector matrix and the surround. A second Monte Carlo run ("tracking OFF mode") tracked all scatter interactions, however, with this mode the energy resulting from x-ray fluorescence was considered completely deposited at the spatial coordinates of the photoelectric interaction. The results of these two Monte Carlo runs were compared to better understand the relative contributions of scatter (Rayleigh and Compton) compared to x-ray fluorescence.

Densities used for each phosphor composition are given in Table I. With the exception of the amorphous Se and CsI, all the other scintillators were considered to be combined with a 5% weight fraction of binder. The elemental composition (C, H, and O) of CarboSet 526 (BF Goodrich, Cleveland, OH) was utilized as the binder, and was added to the various intensifying screen compositions. The physical den-

TABLE I. Physical characteristics of the x-ray detector materials studied.

Detector	Density <sup>a</sup> (g/cm <sup>3</sup> )	Element 1 <sup>b</sup>	Element 2 <sup>b</sup>	Binder?
Gd <sub>2</sub> O <sub>3</sub> S	7.34	Gd: Z=64, K=50.3 keV	...	✓
CsI	4.51	Cs: Z=55, K=36.0 keV	I: Z=53, K=33.2 keV	
Se	4.79	Se: Z=34, K=12.6 keV	...	
BaFBr	4.56	Ba: Z=56, K=37.5 keV	Br: Z=35, K=13.4 keV	✓
YTbO <sub>4</sub>	7.57	Y: Z=39, K=17.0 keV	Ta: Z=73, K=67.6 keV	✓
CaWO <sub>4</sub>	6.12	W: Z=74, K=69.7 keV	...	✓
ThO <sub>2</sub>	9.86	Th: Z=90, K=110.1 keV	...	✓

<sup>a</sup>Densities vary depending on the source. The densities used here were developed by consensus from industrial contacts.

<sup>b</sup>Only the K-edges or atomic numbers of the principal x-ray absorbing elements in the detector material are reported.

sities indicated in Table I were used to adjust the physical thickness of the various x-ray phosphors appropriately. A series of different mass thicknesses (mg/cm<sup>2</sup>) was studied, ranging from 30 mg/cm<sup>2</sup> to 150 mg/cm<sup>2</sup> by 30 mg/cm<sup>2</sup> intervals. The mass thicknesses reported here do not include the contribution of the CarboSet binder, as this is the convention used in the x-ray screen industry.

The x-ray source for each Monte Carlo run consisted of monoenergetic photons normally incident on the x-ray screen [Fig. 1(B)]. The source to detector distance was 100 mm, and a parallel pencil x-ray beam was simulated using a cone with an extremely small cone angle (0.001 deg or 17.5  $\mu$ rad). In addition to the source and x-ray detector, a series of x-ray monitors referred to here [and on Fig. 1(B)] as "sensors" were used to monitor the x-ray energy redistribution away from the detector itself. Two sensors forming a closed cylinder on top of the detector were positioned above and around the x-ray source. Together these sensors effectively measured the x-ray fluorescent re-emission and x-ray scatter emanating from the front surface of the x-ray detector [labeled "backscatter sensor" in Fig. 1(B)]. Another sensor, 0.100 mm in diameter, was placed behind the x-ray detector (separated from the bottom of the detector plane by 10 mm) to measure the transmitted primary radiation. A sensor was also placed parallel to and just outside the transmitted primary sensor, and was used to measure the x-ray energy from x-ray fluorescence and scatter mechanisms that were forward-directed. The sensors referred to here and shown in Fig. 1(B) are a fabrication of computer simulation, and in effect are ideal detector systems; they simply measure all the radiation energy striking them, and no scattering, x-ray fluorescence, or transmission occurs at these sensors.

The Monte Carlo experiments led to the generation of a lot of detailed information, however an attempt was made to make the reported results concise. While the Monte Carlo runs themselves were performed using monoenergetic x-ray beams, such beams are not available in radiology departments in general. Therefore, the monoenergetic results were spectrally weighted in some situations using typical polychromatic tungsten-anode spectra in the 40–130 kVp range.<sup>13</sup>

Validation of Monte Carlo studies is essential towards an understanding of the limitations and accuracy of the method. The TART 98 code package is a fully validated Monte Carlo

transport code for photons and neutrons, and is used at national weapons laboratories for simulating energy transport. Additionally, the authors have recently performed extensive comparisons between the TART 98 code and other sources of medical physics related data, derived both experimentally and by the Monte Carlo methods of others. While the comparison work is still in progress, comparisons pertinent to radiation dose levels in mammography have been published<sup>14</sup> and demonstrate excellent agreement with two other sources of data.

The Monte Carlo simulations were performed on 333 MHz and 400 MHz Pentium-based computers running NT 4.0 (Microsoft Corporation, Redmond, WA). A significant amount of custom software (Visual C/C++ 5.0, Microsoft Corporation, Redmond, WA) was used for the generation of the input script files and subsequent analysis of the output results of the TART 98 Monte Carlo package. Some of the data presented in this study were produced by straightforward numerical calculations utilizing the mass attenuation coefficients.<sup>15</sup>

### III. RESULTS WITH DISCUSSION

#### A. Stopping power comparisons

In any comparison between various x-ray detectors, it is useful to explore the relative stopping power of different x-ray detector materials. Figure 2 illustrates both the 50% stopping power [Fig. 2(A)] and the 90% stopping power [Fig. 2(B)] for the seven detector materials under study. The photon thickness required to attenuate a given fraction (0.5 or 0.9) of the incident x-ray photons is shown for each detector material as a function of x-ray energy. In general, detector materials with greater density and higher atomic number attenuate efficiently. Selenium, with Z=34 and a relatively low density is the poorest x-ray absorber (Fig. 2), implying that selenium detectors need to be much thicker. In conventional intensifying screens, increasing thickness is usually accompanied by a loss of spatial resolution due to the spread of optical light photons. Selenium detectors, on the other hand, are used to directly detect the charges released in the detector by x-ray ionization. Selenium detector systems currently being studied<sup>16,17</sup> employ an electric field across the detector surface, which acts to limit (and almost elimi-

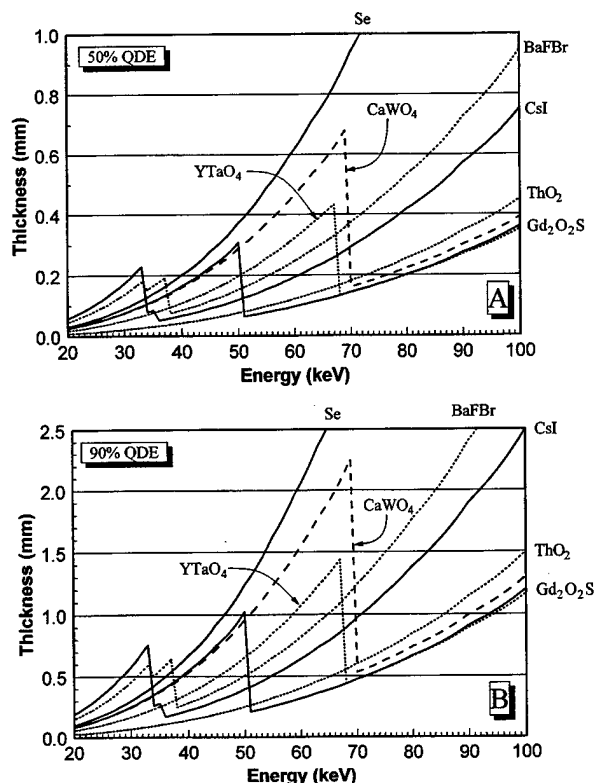


FIG. 2. (A) The thickness' of various x-ray detector materials needed to attenuate 50% of the incident x-ray photons is illustrated. (B) The thickness' of the detector materials required to achieve 90% quantum detection efficiency, illustrated.

nate) lateral charge diffusion, meaning that the Se thickness can be increased substantially without a loss in spatial resolution. Because of this, the thicknesses of Se studied was extended beyond the thickness range used for the other detector materials, from 30 to 1000 mg/cm<sup>2</sup>. While light spread blurring is not a consideration with Se detectors, extremely thick flat detectors may suffer from parallax problems at the periphery of the field of view and this effect is not considered here.

The detector materials with better absorption properties are the ones with curves near the bottom of Figs. 2(A) and 2(B), indicating a smaller thickness of material is needed to detect the same fraction of incident photons. The BaFBr phosphor, the most common component of CR systems, is seen in Fig. 2 to possess a fairly low x-ray detection efficiency, compared to the other intensifying screen materials illustrated. The advantage that Gd<sub>2</sub>O<sub>2</sub>S has over CaWO<sub>4</sub> in terms of detection efficiency, and one of the several reasons why this "rare earth" phosphor became dominant in the intensifying screen business in the 1970s, is apparent from Figs. 2(A) and 2(B). These two phosphors are roughly equivalent up to 50 keV, although Gd<sub>2</sub>O<sub>2</sub>S clearly outperforms CaWO<sub>4</sub> between the Gd *K*-edge at 50.3 keV and the W *K*-edge at 69.7 keV.

Thorium oxide (ThO<sub>2</sub>) is a phosphor that the authors have been interested in for some time.<sup>18,19</sup> It is a known scintillator,<sup>19</sup> with a conversion efficiency of approximately 5%–8%. However, ThO<sub>2</sub> has a radioactive aspect to it that

has precluded its use in screen–film radiography. Since film may in some cases sit next to the intensifying screen in the cassette for hours or even weeks, depending on the cassette usage, radiation-induced artifacts (black spots) would be a serious problem. For use in digital radiography, however, where the total integration time of the photoreceptor signal is very short (comparable to the x-ray exposure time, typically  $\ll 1.0$  s), the radioactivity of ThO<sub>2</sub> becomes much less of an issue. As seen from Figs. 2(A) and 2(B), based on its x-ray energy absorption properties, ThO<sub>2</sub> has excellent potential as a radiographic detector. There are advantages of having the *K*-edge of the detector above (110 keV) and the *L*-edge below (20 keV) the x-ray energies used most commonly for general radiography, since this eliminates x-ray characteristic emission.

## B. The relative magnitude of energy redistribution

Figure 3 illustrates the way in which incident x-ray energy is distributed phenomenologically for the seven x-ray detector materials studied. Monte Carlo experiments were performed at thicknesses ranging from 30 to 150 mg/cm<sup>2</sup>; however only the 90 mg/cm<sup>2</sup> thickness data are presented in Fig. 3 for brevity. The 90 mg/cm<sup>2</sup> thickness is probably close to the practical thickness used clinically for single-screen, general purpose digital radiography. In Fig. 3, the ordinate axis is logarithmic in order to better present the wide range of the results. For Fig. 3(A) (Gd<sub>2</sub>O<sub>2</sub>S), at 55 keV (a little above the Gd *K*-edge), the amount of x-ray energy redirected back towards the x-ray tube by backscattering and x-ray fluorescence was 16.5% [as measured by the "backscatter sensor" in Fig. 1(B)] whereas 14.8% of the x-ray energy incident on the detector was directed forward through the detector as secondary emissions [and measured by the "forward scatter sensor" in Fig. 1(B)]. Another 7.6% of the incident energy was redistributed in the x-ray detector itself [Fig. 1(A)] as reabsorbed scatter and fluorescence. At 55 keV, therefore, a total of 38.9% of the incident x-ray energy is redistributed by scattering or x-ray fluorescent events, while only 27.9% of the energy is absorbed as primary. Figure 3(A) demonstrates clearly that the backscatter fraction, forward scatter fraction, and secondary radiation reabsorbed in the screen each experience a dramatic increase at the *K*-edge, implying that the principal component of this redistributed secondary radiation is actually photoelectric re-emission (x-ray fluorescence). There is also a small peak ( $\sim 3\%$ ) in backscatter at 8 keV, corresponding to the *L*-edge fluorescence of gadolinium.

Figures 3(A)–3(G) illustrate the absorbed primary and transmitted primary energy distributions. These curves can be calculated fairly accurately using simple Lambert–Beers Law relationships, but were determined from the Monte Carlo simulations. They are included in Figs. 3(A)–3(G) for reference. The other three curves on each graph were pro-

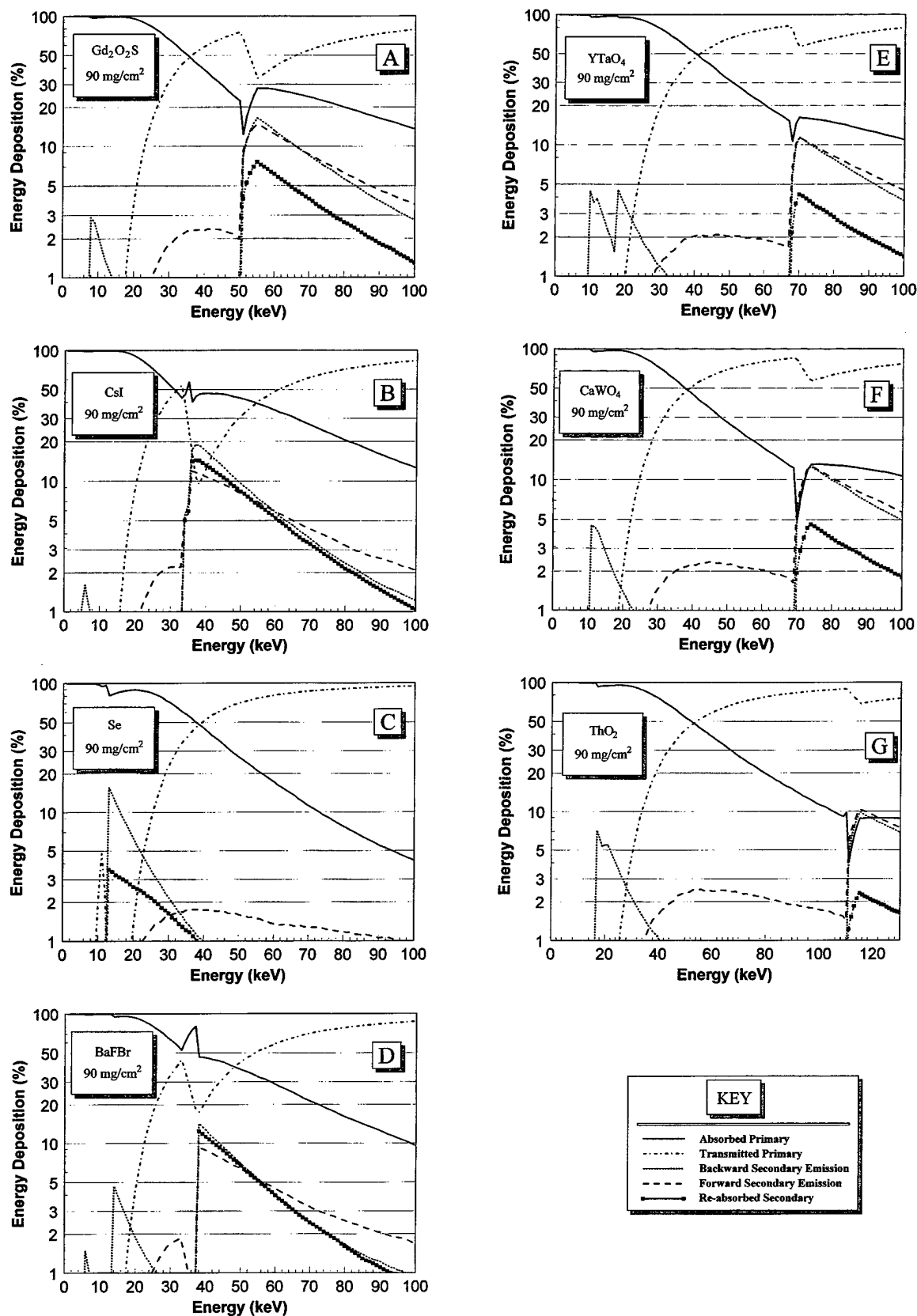


FIG. 3. The energy deposition for seven different x-ray detector materials is illustrated as a function of energy. For all seven figures (A-G), a detector thickness of  $90 \text{ mg cm}^2$  was simulated. The key indicates the deposition type of each of the five lines illustrated in each graph. The graphs correspond to (A)  $\text{Gd}_2\text{O}_2\text{S}$ , (B)  $\text{CsI}$ , (C)  $\text{Se}$ , (D)  $\text{BaFBr}$ , (E)  $\text{YTaO}_4$ , (F)  $\text{CaWO}_4$ , and (G)  $\text{ThO}_2$ . Notice that the ordinate axis is a logarithmic scale.

duced using Monte Carlo techniques. For the seven detector materials in Fig. 3 (A:Gd<sub>2</sub>O<sub>3</sub>S, B:CsI, C:Se, D:BaFBr, E:YTaO<sub>4</sub>, F:CaWO<sub>4</sub>, and G:ThO<sub>2</sub>) the graphs illustrate, more or less, the effects discussed in the last paragraph concerning Gd<sub>2</sub>O<sub>3</sub>S. At the *K*-edge of the detector materials (and to a lesser extent at the *L*-edges), there is a precipitous jump in backward, forward, and lateral (reabsorbed) secondary emissions. On all seven of the detector materials, just above the *K*-edge where x-ray fluorescence is the overwhelming majority of the secondary radiation, it can be seen that the forward scatter and the backscatter are approximately the same. For relatively thin detectors such as those represented in Fig. 3 (90 mg/cm<sup>2</sup>), since x-ray fluorescence is isotropic, there is an approximately equal chance of forward or backward emission at the photoelectric interaction site. However, because x-ray interactions occur predominantly near the front surface of the detector, x-ray fluorescent photons which are forwardly directed may be absorbed in the detector thickness. For detector materials with lower *K*-edges, such as CsI [Fig. 3(B)] and BaFBr [Fig. 3(D)], this effect is amplified because the low energy of the x-ray fluorescent photons reduce their probability of penetrating the thickness of the detector.

Figure 4 illustrates the redistributed energy curves (as shown in Fig. 3) for Gd<sub>2</sub>O<sub>3</sub>S, which is illustrative of the other detector materials. Figure 4(A) shows backward emissions from the detector, Fig. 4(B) illustrates the forward emissions, and Fig. 4(C) shows the secondary radiation reabsorbed laterally in the detector. These data are shown on a linear axis, and the curves for all five detector thicknesses are illustrated to convey the trends of secondary re-emission that are detector-thickness related. First of all, an abrupt jump occurs in all curves [Figs. 4(A), 4(B), and 4(C)] at 51 keV, just above the 50.3 keV *K*-edge of Gd. Since Rayleigh and Compton scattering cross sections do not experience dramatic changes in cross section, whereas the photoelectric interaction does, clearly most of the secondary energy redistribution is due to x-ray fluorescence and very little is due to Rayleigh or Compton scattering. For the case in which x-ray fluorescence is re-emitted back towards the x-ray source [Fig. 4(A)], there is an increase in the percentage of energy being "backscattered" as the detector thickness increases. In fact, there is no mechanism to suggest that this trend reverses, and one would therefore anticipate that with increasing detector thickness (beyond 150 mg/cm<sup>2</sup>), the curves would continue to increase in height, albeit slowly, and at some point no change would be observed with increasing thickness.

How does the re-emission of x-ray fluorescence back towards the x-ray tube affect the imaging performance in digital radiography? First, radiation that "bounces off" the front surface of the x-ray detector is headed back (through the antiscatter grid, if present) toward the patient, and much of this energy will be absorbed in the patient as radiation dose. In detector optimization scenarios where patient dose is considered,<sup>20,21</sup> the dose contribution due to x-ray fluorescence may be significant and should be considered in optimization calculations. However, it is expected from geo-

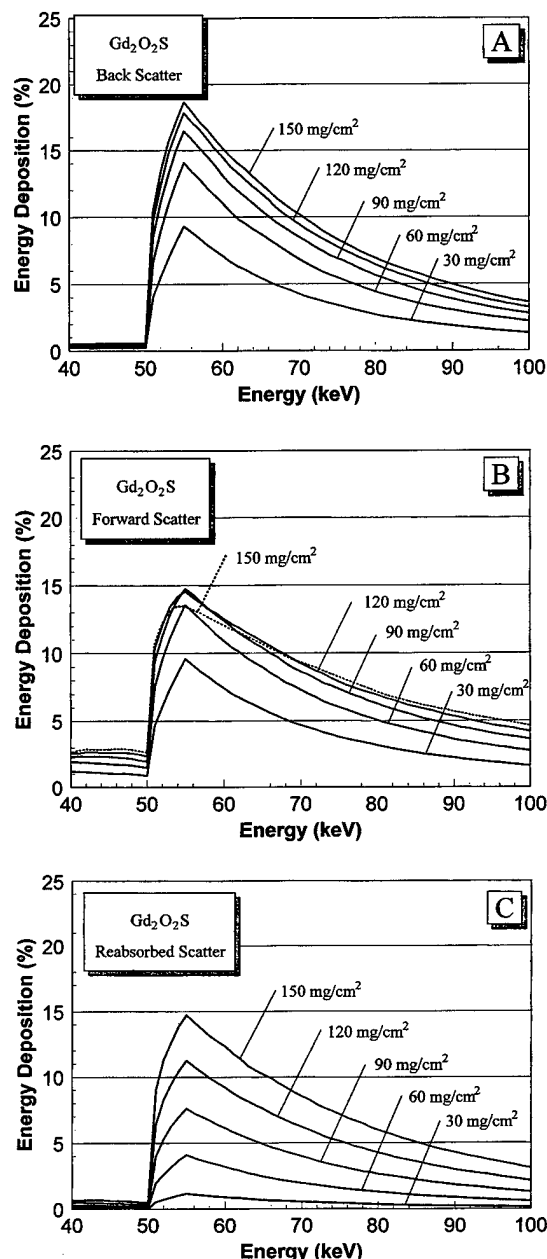


FIG. 4. The energy deposition near the *K*-edge of Gd<sub>2</sub>O<sub>3</sub>S is illustrated for the five detector thicknesses indicated. In (A), the "backscatter" is illustrated, in (B) the energy escaping the x-ray detector in the forward direction (opposite the x-ray source) is indicated, and in (C) the fraction of reabsorbed scatter is illustrated. In this figure, the term "scatter" refers to both photoelectric readmission as well as Rayleigh and Compton scatter.

metrical considerations that the presence of an antiscatter grid between patient and detector would substantially reduce patient exposure, although above 88 keV, the backwards-directed x-ray fluorescence of the lead in the grid slats would become a concern. Second, x-ray detector systems perform best when each x-ray quantum absorbed in the detector contributes the same size signal in the detector electronics. Take the example of a 70 keV incident x-ray interacting by the photoelectric effect in a Gd<sub>2</sub>O<sub>3</sub>S detector. In those interactions where the x-ray fluorescent energy is reabsorbed in the detector, the signal generated corresponds to the deposition

of 70 keV. However, when *K* escape occurs, the energy deposited in the detector is  $70 - 50 = 20$  keV, generating a signal just 29% of the previous example. Therefore, the escape or lateral reabsorption of x-ray fluorescence results in a broadening of the signal variance per incident x-ray photon, and this acts to reduce the detective quantum efficiency (DQE) of the detector system.<sup>2,22-26</sup>

In Fig. 4(B), the curve corresponding to the thickest detector ( $150 \text{ mg/cm}^2$ ) "bends over," that is, the curves (in the 50–70 keV range, at least) appear to have reached a maximum somewhere near the  $120 \text{ mg/cm}^2$  thickness, and the fractional energy allocation to forward scattering decreases with increasing thickness past this point. The mechanisms were alluded to previously, where most x-ray interactions occur at the entrant surface of the detector. Fluorescent x-ray photons emitted with a forward scatter trajectory tend to be attenuated by increasing detector thickness. Indeed, in the limit of infinite screen thickness, the amount of secondary energy passing through the screen in the forward direction would drop to zero. This investigation is focused on evaluating properties of x-ray detectors for digital radiography systems. For indirect systems such as *a*-Si TFTs, CCDs, or CMOS systems, the amount of x-ray radiation reaching the silicon electronics is a source of concern. X-rays reaching and interacting with the silicon electronics can cause the appearance of "snow" on the image, and over prolonged periods may cause radiation damage.<sup>27</sup> Standard Lambert Beers calculations will underestimate the fraction of x-ray energy reaching the photoreceptor. At the energies just above the detector *K*-edges, a significant fraction (e.g.,  $\sim 10\%$ – $15\%$  in the 50–70 keV energy region for  $\text{Gd}_2\text{O}_3\text{S}$ ) of the incident x-ray energy is seen to be re-emitted as fluorescence directed towards the photoreceptor.

Figure 4(C) demonstrates that the fraction of energy reabsorbed in the detector (laterally) increases with detector thickness. This component of x-ray energy deposition is the integrated energy deposited in all the concentric annuli except for the innermost circle [see Fig. 1(A)].

Figures 2–4 illustrate energy allocation trends as a function of monoenergetic x-ray energy, as opposed to "real world" polyenergetic x-ray sources. While x-ray fluorescent energy that escapes the detector in either direction has some subtle adverse effects as discussed above, x-ray fluorescence that is reabsorbed in the detector may cause either a reduction in the spatial resolution, an increase in noise, or both. Figure 5 illustrates the secondary radiation/primary radiation fraction (*S/P*) absorbed in the detector, as a function of polyenergetic x-ray beams ranging from 40 kVp to 130 kVp. The x-ray spectra were generated<sup>28</sup> assuming a standard tungsten anode x-ray system with 2.0 mm of added Al filtration and were calculated at 5 kVp intervals. The five detector thicknesses ranging from  $30 \text{ mg/cm}^2$  to  $150 \text{ mg/cm}^2$  are shown ( $200$ – $1000 \text{ mg/cm}^2$  for Se). The thickness labels are omitted in Figs. 5(B) and 5(D), 5(G) for clarity.

In Fig. 5(A), the *S/P* ratio increases rapidly as the kVp exceeds the 50 keV *K*-edge of the Gd-based detector. In Fig. 5(B), the curves rapidly increase from the 33 to 35 keV *K*-edges of cesium and iodine; however, the graph is limited

to 40 kV and above since x-ray spectra generated below 40 kVp are rarely used in general radiography settings. The *S/P* ratios for CsI [Fig. 5(B)] are quite high, reaching  $\sim 17\%$  for the  $90 \text{ mg/cm}^2$  detector in the 65–90 kVp region. The *S/P* ratios for selenium [Fig. 5(C)] are quite low, in part due to the low *K*-edge of selenium (12.6 keV). BaFBr demonstrates a *S/P* ratio of  $\sim 12\%$  above 70 kVp [Fig. 5(D)] for the  $90 \text{ mg/cm}^2$  detector. The detectors comprised of  $\text{YTaO}_4$  [Fig. 5(E)] and  $\text{CaWO}_4$  [Fig. 5(F)] show marked increases in the *S/P* ratio above their respective *K*-edges of 67.6 keV and 69.7 keV, respectively; however, the overall *S/P* ratio is lower with these detectors compared to  $\text{Gd}_2\text{O}_3\text{S}$  and CsI. The  $\text{ThO}_2$  detector, with *S/P* results shown in Fig. 5(G) shows very low *S/P* values ( $<1\%$ ) across the usable energy region. The secondary component (the numerator of *S/P*) is primarily x-ray fluorescence, and with a *K*-edge of 110 keV, fluorescence is not produced with most clinical x-ray spectra. There is another source of "secondary" radiation in a thorium-based detector, that from radioactive emissions in the screen itself (thorium is a 4 MeV  $\alpha^{++}$  emitter with a  $1.4 \times 10^{10}$  year half-life). This consideration is beyond the scope of this study.

### C. Lateral reabsorption of scattered and fluorescent energy

The geometry of the Monte Carlo studies [Figs. 1(A) and 1(B)] was designed to allow the assessment of the lateral (radial) distribution of energy, away from the point where the incident x-ray beam was incident upon the detector. Figure 6 illustrates the radial distribution of energy for the  $90 \text{ mg/cm}^2$   $\text{Gd}_2\text{O}_3\text{S}$  detector under various simulation conditions. This figure is provided to directly illustrate the role of x-ray fluorescence relative to Rayleigh and Compton scattering. The results of three different Monte Carlo runs are illustrated, as indicated in the figure. The Monte Carlo routine provides the option to turn on or off the tracking of characteristic x-ray emissions, and if routine was run in the "tracking OFF" mode, the energy of the characteristic x-ray was deposited at the site of the photoelectric interaction. Two curves are shown in Fig. 6 at 51 keV, just above the *K*-edge of Gd; and the 51 keV "tracking ON" curve shows a radial distribution profile with much greater amplitude than the 51 keV "tracking OFF" curve. The 51 keV "tracking OFF" curve shows the radial distribution of energy due to Rayleigh and Compton scattering only, while the 51 keV "tracking ON" curve also includes the effect of fluorescence. To further illustrate the role of fluorescence, the results from a 50 keV "tracking ON" run are shown. While x-ray fluorescence was tracked, the 50 keV simulation was just below the 50.3 keV *K*-edge of Gd, and therefore *K*-shell fluorescence was not produced. Consequently, the 50 keV "Tracking ON" curve is comparable to the 51 keV "Tracking OFF" curve, with differences being due to *L*-edge fluorescence and stochastic effects. The exponential tails of the 51 keV "Tracking ON" and "Tracking OFF" curves were computer fit ( $r \geq 0.98$ ) over the radial distances between 0.10 mm and 1.0 mm. The y-intercept ratio was calculated as

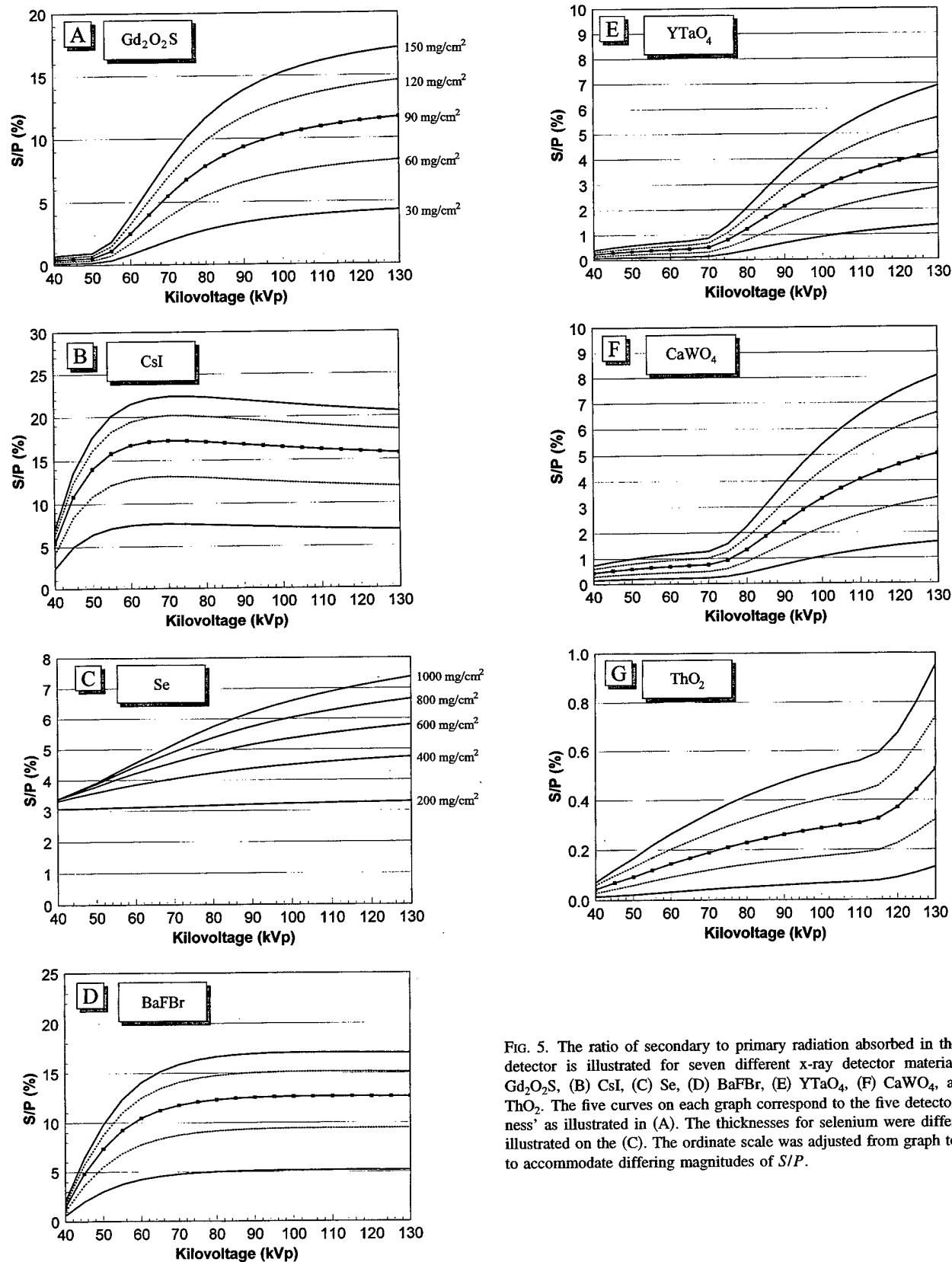


FIG. 5. The ratio of secondary to primary radiation absorbed in the x-ray detector is illustrated for seven different x-ray detector materials; (A)  $Gd_2O_2S$ , (B) CsI, (C) Se, (D) BaFBr, (E)  $YTaO_4$ , (F)  $CaWO_4$ , and (G)  $ThO_2$ . The five curves on each graph correspond to the five detector thicknesses as illustrated in (A). The thicknesses for selenium were different, as illustrated on the (C). The ordinate scale was adjusted from graph to graph to accommodate differing magnitudes of S/P.

18.2, suggesting that the difference in amplitude between fluorescence+scatter vs scatter alone is approximately a factor of 20. Clearly, x-ray fluorescence is the predominant contributor toward the lateral spread of energy in the detector.

Figure 7 shows the effect of detector thickness for the  $Gd_2O_2S$  detector at 51 keV. The curves shown in Fig. 7 illustrate the radial distribution of energy due (primarily) to x-ray fluorescence. Energy deposition was calculated by

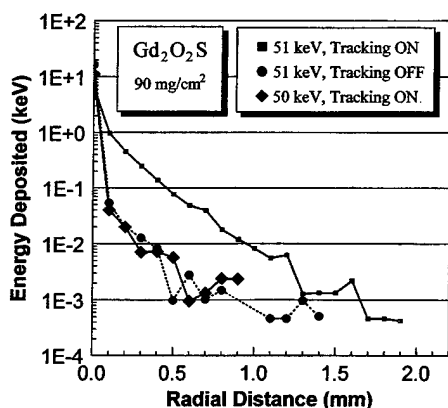


FIG. 6. The radial distribution of the energy deposition as determined in the Monte Carlo simulations is shown for various Monte Carlo runs. The results for a 90 mg/cm<sup>2</sup> thick Gd<sub>2</sub>O<sub>2</sub>S intensifying screen are shown. The two "tracking ON" curves straddled the K-edge of Gd, and the difference between the curves illustrates the influence of x-ray fluorescence. The two 51 keV curves, one which followed x-ray fluorescence and one which did not, also demonstrate that the influence of x-ray fluorescence is greater than an order of magnitude greater than the combined influence of Rayleigh and Compton scattering.

summing the energy over all radial distances. As shown in Fig. 4(C), the magnitude of energy reabsorbed in the detector increases with detector thickness. Figure 7 also shows this trend, with the thicker detectors experiencing markedly more energy deposited at a given distance than the thinner detectors. For example, at a radial distance of 0.50 mm, the ratio of energies deposited in 150 and 30 mg/cm<sup>2</sup> thick detectors is 28.

The radial distribution of fractional energy deposition is illustrated in Figs. 8(A)–8(G). Curves are shown for each detector thickness studied, with the 30 mg/cm<sup>2</sup> curve consistently being the lowest and the 150 mg/cm<sup>2</sup> being the uppermost [the Se thicknesses were different, and are indicated in Fig. 8(C)], with monotonic progression of curves between thicknesses. Each curve was produced by weighting 100 monoenergetic curves (1 keV–100 keV) by a 100 kVp x-ray spectrum, as described previously. The curves shown in Fig. 8 must be interpreted carefully. These are not "cuts"

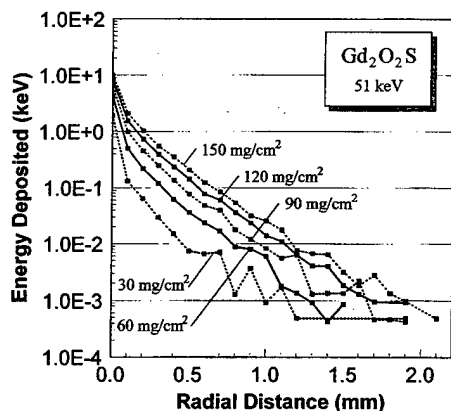


FIG. 7. This figure illustrates the influence of detector thickness on the radial distribution. Not surprisingly, the thicker detectors result in a broadened radial distribution.

through the point spread function (PSF) of the detector, because the energy at each radial distance  $\Gamma$  is integrated around the annulus of radius  $\Gamma$  [Fig. 1(E)]. Therefore, the curves illustrated in Fig. 8 must be multiplied by  $1/\Gamma$  to yield the PSF. Such a procedure would attenuate the profiles shown to even lower levels.

The curves in Fig. 8 are shown on semilogarithmic axes, and certainly the amount of x-ray energy distributed radially at some distance  $\Gamma$  (as shown on the figures) appears very small. However, to compute the total amount of energy redistributed radially, one has to integrate the individual curves. This was computed, and the results are shown in Fig. 9 for the three most practical thicknesses for radiographic applications. For example, in Fig. 9(A), the CsI curve (open circles) at a radial distance of 0.50 mm has an ordinate value of 0.80%. This means that 0.80% of the absorbed energy for the 60 mg/cm<sup>2</sup> CsI detector was deposited *outside* a circle 0.5 mm in radius, and conversely 99.20% of the absorbed energy was deposited *within* a circle 1.0 mm in diameter.

#### IV. FURTHER DISCUSSION

The redistribution of x-ray energy in an x-ray detector was the focus of this investigation. Other factors are also responsible for the redistribution of signal intensity in an image receptor. For example, the full-width at half-maximum (FWHM) of the line spread function for a Lanex screen (120 mg/cm<sup>2</sup> Gd<sub>2</sub>O<sub>2</sub>S) is approximately 1.9 mm, and the radial distribution profiles calculated here (Fig. 8) imply that the FWHM of the line spread or point spread function due to x-ray fluorescence and x-ray scattering is much narrower, on the order of 0.10 mm. Under most conditions, therefore, the spread function owing to the lateral diffusion of optical photons in an intensifying screen will completely dominate the point spread function of the system. In the case of a direct detector, however, where an electric field across the plane of the detector effectively eliminates the lateral diffusion of electronic charge liberated in the detector, x-ray fluorescence could degrade spatial resolution (i.e., broaden the point spread function).

Does x-ray fluorescence contribute to a loss of spatial resolution by broadening the PSF, or does it contribute to noise? The short answer is probably both. Take as an example an imaginary x-ray intensifying screen that experiences no lateral diffusion of the light photons emitted, and therefore has a near-perfect PSF. X-ray fluorescent photons which are emitted at a point  $P$  and then are reabsorbed in the screen a distance  $\Gamma$  away from that point, will be resolved as separate points. The signal generated by the reabsorbed fluorescent x-ray will contribute to the noise in the detector. Because the distance between the site of initial photoelectric interaction and the site of the fluorescent photons interaction is nonrandom (and has a well-defined probability density function as shown in Fig. 8), the noise due to fluorescent reabsorption will be correlated.<sup>25</sup> Continuing with the example, let the width of the optical diffusion PSF component of the intensifying screen be increased. Now when the fluorescent x-ray photon is reabsorbed a distance  $\Gamma$  away from



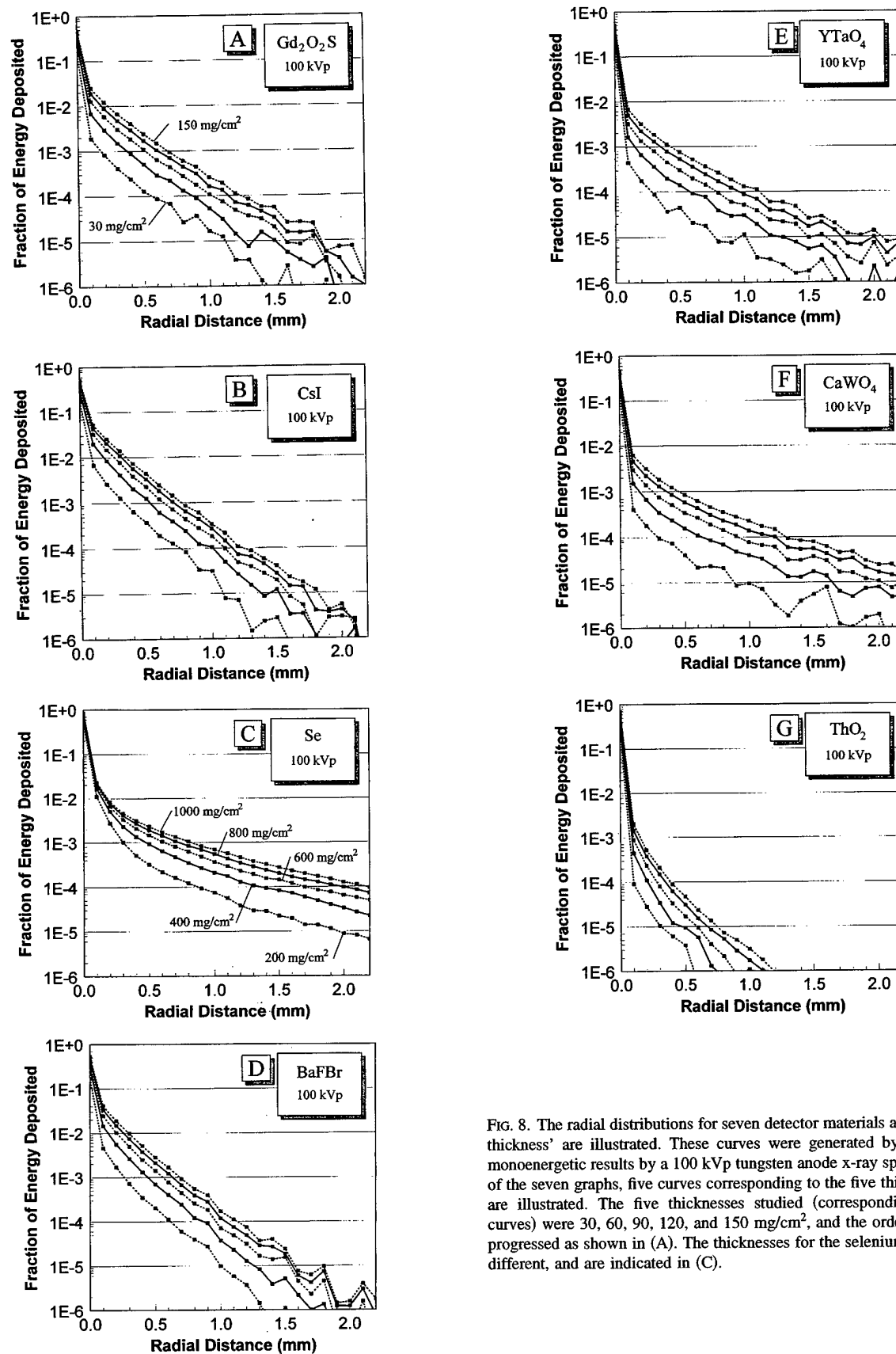


FIG. 8. The radial distributions for seven detector materials and five detector thicknesses are illustrated. These curves were generated by weighting the monoenergetic results by a 100 kVp tungsten anode x-ray spectrum. In each of the seven graphs, five curves corresponding to the five thicknesses studied are illustrated. The five thicknesses studied (corresponding to the five curves) were 30, 60, 90, 120, and 150  $\text{mg}/\text{cm}^2$ , and the order of the curves progressed as shown in (A). The thicknesses for the selenium detector were different, and are indicated in (C).

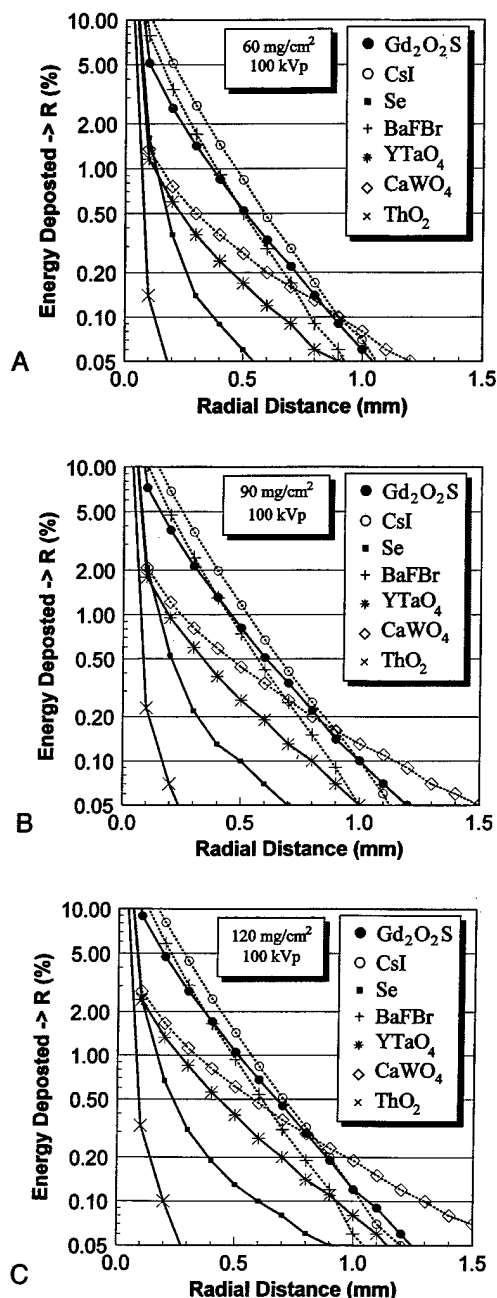


FIG. 9. The curves illustrate the fraction (in %) of absorbed x-ray energy that is deposited outside a given radial distance. The figures are for (A) 60 mg/cm<sup>2</sup> detector thicknesses, (B) for 90 mg/cm<sup>2</sup> detector thicknesses, and (C) for 120 mg/cm<sup>2</sup> detector thicknesses. For example, in (B) 0.50% of the energy absorbed in the Gd<sub>2</sub>O<sub>3</sub>S detector was reabsorbed greater than 0.60 mm away from the position of the incident primary x-ray beam.

the primary interaction point *P*, the optical signals generated in the two interactions are blurred together such that they both contribute to the signal under the point spread "cone." In this case, because the fluorescent photon is not resolved spatially, it no longer is a source of noise but rather becomes part of the signal. Furthermore, by combining the signals generated by the photoelectric interaction and the reabsorbed fluorescent x-ray under the same signal cone, the signal to noise ratio would slightly increase, although this is a rela-

tively small contribution.<sup>24,25</sup> So, while optical photon broadening of the PSF of an intensifying screen obviously reduces the spatial resolution of that detector, it also increases the SNR somewhat.

In a real x-ray intensifying screen with optical photon induced PSF widths in millimeters, it is likely given the very short range of radial redistribution (Fig. 8) for x-ray fluorescence (and scatter), that the majority of fluorescent interactions occur within the point spread cone. Some small fraction will occur outside the signal cone, and these will contribute a source of a correlated noise to the image. To give real numbers to this example, for 90 mg/cm<sup>2</sup> CsI exposed at 100 kV [Fig. 9(B)], 2% of the absorbed energy is deposited outside a circle of diameter of 0.80 mm, and 0.5% of the absorbed energy is deposited outside a circle 1.3 mm in diameter. In a pixelated digital detector system designed for general radiography, which pixel dimensions in the 100–200 μm range, some small but not negligible redistribution effects due to x-ray fluorescence will be realized.

## V. SUMMARY

The *K*-edge(s) of a detector material are traditionally thought of as an opportunity to improve the energy absorption of the detector; however the results of this study indicate that this opportunity is fraught with compromise. The emission of characteristic x-rays after photoelectric interactions in the detector results in a substantial loss in energy absorption at the interaction site, and this transiently absorbed x-ray energy is then dispersed backward, forward, and laterally in the detector. The radial distribution of x-ray fluorescence will have little consequence on the point spread function of scintillation detectors studied. In selenium direct detectors with their near-perfect point spread functions, however, reabsorbed x-ray fluorescence may be more of a concern. Finally, the properties of a little studied phosphor, ThO<sub>2</sub>, appear promising in the context of energy absorption.

## ACKNOWLEDGMENTS

This research was supported in part from grants from the United States Army Breast Cancer Research Program (DAMD 17-94-J-4424 and DAMD 17-98-1-8176), the California Breast Cancer Research Program (1RB-0192), and the National Cancer Institute (R21 CA82077-01). We are grateful to Dr. Red Cullen for providing the TART 98-2 update to the authors for its use in this study.

<sup>a)</sup>Address for correspondence: John M. Boone, Ph.D., Department of Radiology, UC Davis Medical Center, 4701 X Street, Sacramento, CA 95817. Phone: (916) 734-3158; FAX: (916) 734-0316; electronic mail: jmb Boone@ucdavis.edu

<sup>1</sup>L. E. Antonuk, Y. el-Mohri, J. H. Siewerdsen, J. Yorkston, W. Huang, V. E. Scarpine, and R. A. Street, "Empirical investigation of the signal performance of a high-resolution, indirect detection, active matrix flat-panel imager (AMFPI) for fluoroscopic and radiographic operation," *Med. Phys.* **24**, 51–70 (1997).

<sup>2</sup>J. H. Siewerdsen, L. E. Antonuk, Y. el-Mohri, J. Yorkston, W. Huang, and I. A. Cunningham, "Signal, noise power spectrum, and detective quantum efficiency of indirect-detection flat-panel imagers for diagnostic radiology," *Med. Phys.* **25**, 614–628 (1998).

- <sup>3</sup>T. T. Farman and A. G. Farman, "Clinical trial of panoramic dental radiography using a CCD receptor," *J. Digit. Imaging* **11**, 169–171 (1998).
- <sup>4</sup>S. Hejazi and D. P. Trauernicht, "System considerations in CCD-based x-ray imaging for digital chest radiography and digital mammography," *Med. Phys.* **24**, 287–297 (1997).
- <sup>5</sup>T. Yu, J. M. Sabol, J. A. Seibert, and J. M. Boone, "Scintillating fiber optic screens: A comparison of MTF light conversion efficiency, and emission angle with  $Gd_2O_2S: Tb$  screens," *Med. Phys.* **24**, 279–285 (1997).
- <sup>6</sup>H. P. Chan and K. Doi, "Energy and angular dependence of x-ray absorption and its effect on radiographic response in screen-film systems," *Phys. Med. Biol.* **28**, 565–579 (1983).
- <sup>7</sup>H. P. Chan and K. Doi, "Studies of x-ray energy absorption and quantum noise properties of x-ray screens by use of Monte Carlo simulation," *Med. Phys.* **11**, 37–46 (1984).
- <sup>8</sup>C. S. Chen, K. Doi, C. Vyborny, H. P. Chan, and G. Holje, "Monte Carlo simulation studies of detectors used in the measurement of diagnostic x-ray spectra," *Med. Phys.* **7**, 627–635 (1980).
- <sup>9</sup>Y. Kodera, K. Doi, and H. P. Chan, "Absolute speeds of screen-film systems and their absorbed-energy constants," *Radiology* **151**, 229–236 (1984).
- <sup>10</sup>D. E. Cullen, "A coupled neutron-photon 3D combinatorial geometry Monte Carlo transport code," UCRL-ID 126455, 1997.
- <sup>11</sup>The Monte Carlo code was distributed through the Oak Ridge National Laboratory Radiation Safety Information Computational Center: <http://www-rsicc.ornl.gov/codes.ccc.ccc6.ccc-638.html>.
- <sup>12</sup>Dr. Red Cullen at Lawrence Livermore National Laboratory provided the TART 98-2 update to the authors (see acknowledgments).
- <sup>13</sup>J. M. Boone and J. A. Seibert, "An accurate method for computer-generating tungsten anode x-ray spectra from 30 to 140 kV," *Med. Phys.* **24**, 1661–1670 (1997).
- <sup>14</sup>J. M. Boone, "Monte Carlo assessment of glandular breast dose for monoenergetic and high-energy polyenergetic x-ray beams," *Radiology* (in press).
- <sup>15</sup>J. M. Boone and A. E. Chavez, "Comparison of x-ray cross sections for diagnostic and therapeutic medical physics," *Med. Phys.* **23**, 1997–2005 (1996).
- <sup>16</sup>D. L. Lee, L. K. Cheung, B. G. Rodricks, and G. F. Powell, "Improved imaging performance of a  $14 \times 17$  in direct radiography system using a Se/TFT detector," *SPIE* **3336**, 14–23 (1998).
- <sup>17</sup>U. Neitzel, I. Maack, and S. Gunther-Kohfahl, "Image quality of a digital chest radiography system based on a selenium detector," *Med. Phys.* **21**, 509–516 (1994).
- <sup>18</sup>T. Moeller and M. Tecotzky, "Observations on the rare earths. Napht-hazarin complexes of certain rare earth metal ions," *J. Am. Chem. Soc.* **77**, 2649–2650 (1955).
- <sup>19</sup>J. Hubert and P. Thouvenot, "Luminescence properties of  $Eu^{3+}$  and  $Am^{3+}$  in thorium oxide," *J. Alloys Compd.* **80**, 193–200 (1992).
- <sup>20</sup>J. M. Boone and J. A. Seibert, "A comparison of mono- and polyenergetic x-ray beam performance for radiographic and fluoroscopic imaging," *Med. Phys.* **21**, 1853–1863 (1994).
- <sup>21</sup>J. M. Boone, G. S. Shaber, and M. Tecotzky, "Dual-energy mammography: A detector analysis," *Med. Phys.* **17**, 665–675 (1990).
- <sup>22</sup>J. T. Dobbins, D. L. Ergun, L. Rutz, D. A. Hinshaw, H. Blume, and D. C. Clark, "DQE( $f$ ) of four generations of computed radiography acquisition devices," *Med. Phys.* **22**, 1581–1593 (1995).
- <sup>23</sup>J. P. Bissonnette, I. A. Cunningham, D. A. Jaffray, A. Fenster, and P. Munro, "A quantum accounting and detective quantum efficiency analysis for video-based portal imaging," *Med. Phys.* **24**, 815–826 (1997).
- <sup>24</sup>I. A. Cunningham, M. S. Westmore, and A. Fenster, "A spatial-frequency dependent quantum accounting diagram and detective quantum efficiency model of signal and noise propagation in cascaded imaging systems," *Med. Phys.* **21**, 417–427 (1994).
- <sup>25</sup>I. A. Cunningham, "Linear systems modeling of parallel cascaded stochastic processes: The NPS of radiographic screens with reabsorption of characteristic x radiation," *SPIE* **3336**, 220–230 (1998).
- <sup>26</sup>J. H. Siewerdsen, L. E. Antonuk, Y. el-Mohri, J. Yorkston, W. Huang, J. M. Boudry, and I. A. Cunningham, "Empirical and theoretical investigation of the noise performance of indirect detection, active matrix flat-panel imagers (AMFPIs) for diagnostic radiology," *Med. Phys.* **24**, 71–89 (1997).
- <sup>27</sup>J. M. Boudry and L. E. Antonuk, "Radiation damage of amorphous silicon, thin-film, field-effect transistors," *Med. Phys.* **23**, 743–754 (1996).
- <sup>28</sup>J. M. Boone, T. R. Fewell, and R. J. Jennings, "Molybdenum, rhodium, and tungsten anode spectral models using interpolating polynomials with application to mammography," *Med. Phys.* **24**, 1863–1874 (1997).